Image-based and structure-integrated sensor for multiaxial measurement of structure deformations

The Department of Mechanical Engineering
at the Technical University of Darmstadt

Dissertation

by

Nassr Mohammed Mosleh Al-Baradoni

from Dhamar, Yemen

to
obtain the degree of Doctor of Engineering (Dr.-Ing.)

Primary Examiner:	Prof. Dr.-Ing. Dipl.-Wirtsch.-Ing. Peter Groche
Co-Examiner:	Prof. Dr.-Ing. Matthias Weigold
Date of submission:	06.03.2024
Date of oral examination:	15.10.2024

Darmstadt 2024
D17

Al-Baradoni, Nassr Mohammed Mosleh: Image-based and structure-integrated sensor for multiaxial measurement of structure deformations
Darmstadt, Technical University of Darmstadt,
Institute for Production Engineering and Forming Machines – PtU

Year of publication on TUprints: 2024
URN: urn:nbn:de:tuda-tuprints-286578
URI: https://tuprints.ulb.tu-darmstadt.de/id/eprint/28657
Date of the oral examination: 15.10.2024

"To my father, Mohammed Mosleh Al-Baradoni, whose strength and wisdom have inspired my curiosity and determination. This work is a tribute to you, for everything you have dedicated to me in my life.

Acknowledgments

This thesis was written during my time as a research assistant at the Institute for Production Engineering and Forming Machines at the Technical University of Darmstadt. My special thanks belong to Prof. Dr.-Ing. Dipl.-Wirtsch.-Ing. Groche for supervising this work and for giving me the opportunity to devote myself to this exciting research topic and for his constant encouragement with my questions and problems. I would also like to thank Prof. Dr.-Ing. Weigold for critically reviewing the thesis and for acting as co-supervisor.

The main content of this thesis was developed in the context of the subproject B4 in the Collaborative Research Center 805 as well as during the project “Forming position-controlled joining by plastic deformation using optical sensors,” for the funding of which I would like to thank the German Research Foundation. I would also like to thank the students who have significantly contributed to this work through student theses or by working as student assistants. I would also like to thank the staff of the PtU for their supportive cooperation, as well as the staff of the workshop, the secretariat, the accounting department, IT, and all those not yet mentioned who have supported me over the past years.

Aum Ayah deserves my sincere thanks for her professional proofreading of all my scientific works.

I would like to express my deepest gratitude to my family for their unwavering support throughout this journey. To my parents, thank you for your endless encouragement, understanding, and sacrifices that have allowed me to pursue my educational goals. I extend my deepest gratitude to my beloved wife, Amani, and our wonderful children, Sam and Elyas. Their unwavering support, patience, and understanding have been my greatest source of strength throughout this challenging journey.

Darmstadt, March 2024 Nassr Al-Baradoni

Abstract

Automated process chains in Industry 4.0 lead to increasing relevance for data acquisition to control forces and torques in many manufacturing processes. By measuring process forces and moments, it is possible to implement control approaches and, thus, more accurately obtain selected product characteristics. Moreover, the use of sensors is increasing to enable digital structural monitoring approaches and predictive maintenance. However, poor accessibility, error-prone measurement positions, or harsh environments typically prevent the use of external sensors for the accurate measurement of load conditions in load-bearing structures or process forces/moments in manufacturing machines. Structure and machine elements with integrated sensors permit the direct measurement of process forces and moments on the structural components or machine tools without affecting their mechanical functionality. According to the latest research, the integration of electromechanical transducers, such as strain gauge-based or piezoelectric transducers, into passive metallic structures by various methods, especially forming technology, has proven to be particularly promising. However, while these solutions have excellent potential, their widespread implementation is hampered by the limited performance of the sensors, such as high-resolution detection of the direction and magnitude of the applied loads, and their associated high cost.

This dissertation undertakes an investigation into the viability of employing optical image-based measurement concepts for measuring structural deformation under external loads, with the aim of realizing cost-effective and, at the same time, multiaxial sensor load-bearing structures and machine elements. A specialized measurement concept is developed, and relevant system design parameters are identified in a systematic manner. In addition, a process design is investigated for the integration of sensitive optical elements into metallic structures by rotary swaging, taking into consideration the respective requirements for positional accuracy. The dissertation concludes by highlighting the overall potential of optical image-based sensors for the comprehensive detection of multiaxial loads in structures and machine elements, thereby paving the way for the widespread integration of sensor structures and machine elements in various application domains.

Kurzfassung

Mit der Automatisierung von Prozessketten in der Industrie 4.0 gewinnt die Datenerfassung zur Regelung von Kräften und Momenten in vielen Fertigungsprozessen zunehmend an Bedeutung. Durch die Erfassung von Prozesskräften und -momenten können Regelungsansätze umgesetzt werden, um ausgewählte Produkteigenschaften genauer zu erreichen. Darüber hinaus werden zunehmend Sensoren zur digitalen Strukturüberwachung und vorausschauenden Wartung eingesetzt. Allerdings verhindern schlechte Zugänglichkeit, fehleranfällige Messpositionen oder raue Umgebungsbedingungen in der Regel den Einsatz externer Sensoren zur genauen Messung von Belastungszuständen in Tragstrukturen oder von Prozesskräften/-momenten in Fertigungsmaschinen. Durch die Integration von Sensoren in Struktur- und Maschinenelemente können Prozesskräfte und -momente direkt an Bauteilen oder Maschinenwerkzeugen gemessen werden, ohne deren mechanische Funktionalität zu beeinträchtigen. Die Integration von elektromechanischen Wandlern, wie dehnmessstreifenbasierten oder piezoelektrischen Wandlern, in passive metallische Strukturen hat sich nach neuesten Forschungserkenntnissen durch verschiedene Verfahren, insbesondere der Umformtechnik, als besonders vielversprechend erwiesen. Eine breitere Anwendung dieser Lösungsansätze wird jedoch durch die begrenzte Leistungsfähigkeit der Sensoren, wie z. B. die hochauflösende Erfassung von Richtung und Betrag der aufgebrachten Lasten, und die damit verbundenen hohen Kosten behindert.

In dieser Dissertation wird die Einsatzmöglichkeit von optischen, bildbasierten Messkonzepten zur Erfassung von Strukturverformungen unter externen Lasten untersucht, mit dem Ziel, kostengünstige und gleichzeitig mehrachsig sensorische Tragstrukturen und Maschinenelemente zu erzeugen. Zu diesem Zweck wird ein spezielles Messkonzept entwickelt und es werden systematisch die relevanten Systemauslegungsparameter identifiziert. Weiterhin wird ein Prozessdesign zur Integration empfindlicher optischer Elemente in metallische Strukturen durch Rundkneten unter Berücksichtigung der jeweiligen Anforderungen an die Positioniergenauigkeit untersucht. Die Dissertation schließt mit der Betonung des Gesamtpotenzials optischer bildbasierter Sensoren zur Erfassung multiaxialer Belastungen in Strukturen und

Maschinenelementen, wodurch der Weg für eine weitreichende Integration von Sensorsystemen und Maschinenelementen in verschiedenen Anwendungsbereichen geebnet wird.

Index

Acknowledgments .... **I**

Abstract .... **II**

Kurzfassung .... **III**

1 Introduction **1**

2 State of the Art **3**

2.1 Sensor Structures and Machine Elements 3

2.1.1 Manufacturing process for sensor integration into mechanical structures 4

2.1.2 Rotary swaging 6

2.2 Multiaxial Force/Torque Measuring 8

2.2.1 Strain gauge-based multiaxial force/torque sensors 8

2.2.2 State of the research on alternative measuring concepts 11

2.2.3 Multiaxial sensor machine elements 13

2.3 Relevant Fundamentals of Imaging Systems 14

2.3.1 Lenses and optical magnification 15

2.3.2 Photomasks 22

2.3.3 Image sensors 23

2.4 Basics of Image Processing and Machine Learning Algorithms 26

2.4.1 Digital image correlation (DIC) 26

2.4.2 Convolutional neural networks 29

2.4.3 Decision tree algorithm 30

2.4.4 Data augmentation in regression models 31

2.5 Summary 33

3 Motivation and Objective **35**

3.1 Motivation 35

3.2 Objective 36

3.3 Procedure 36

4 Image-Based Multiaxial Measuring of Structural Deformations 38

4.1 Sensor Design 38
4.2 System Behavior Under Load 43
4.3 Measuring Resolution and Measuring Range 47
  4.3.1 Measuring resolution 47
  4.3.2 Measuring range 53
4.4 Procedure for Sensor Configuration 55
4.5 Image Processing 57
  4.5.1 Image pre-processing 57
  4.5.2 Digital image correlation 58
  4.5.3 CNN-based displacement computation 60

5 Validation of the Sensory Properties 64

5.1 Multiaxial Load Determination 64
  5.1.1 Test setup and sensor assembly 64
  5.1.2 Results for uniaxial loading 66
  5.1.3 Determining the crosstalk behavior 67
  5.1.4 Results for multiaxial loads $(\boldsymbol{F}\mathbf{x}+\boldsymbol{F}\mathbf{y}+\boldsymbol{M}\mathbf{z})$ 70
  5.1.5 Results for multiaxial loads $(\boldsymbol{Fx}+\boldsymbol{Fy}+\boldsymbol{Fz}+\boldsymbol{M}\mathbf{z})$ 72
  5.1.6 Sources of measurement errors 74
5.2 Measuring the Bending Moments and Machine Learning-Based Sensor Modelling 77
  5.2.1 Sensor design, experimental test, and results 77
  5.2.2 Measuring resolution of the measuring axis 78
  5.2.3 Sensor modeling using CNN 80
  5.2.4 Sensor modeling using decision tree regression 80
  5.2.5 Results 81

6 Examples of Industrial Applications 84

6.1 Sensor Bending Roll 84
  6.1.1 Combined bending-linear flow splitting process 84

6.1.2 Sensor design and assembly 85
6.1.3 Calibration process and the impact of clamping conditions 86
6.1.4 In-situ calibration of the bending roll and experimental trials 89
6.2 Sensor Guidance Column 93
6.2.1 Blanking tool and tool misalignment problem 93
6.2.2 Sensor assembly experiment setup 94
6.2.3 Results 96
7 Sensor Integration by Rotary Swaging 98
7.1 Process and Joining Partners Design 100
7.2 Numerical Process Simulation 102
7.2.1 Preliminary simulation and basics of model parameters 102
7.2.2 Investigating the effect of rim geometry 104
7.2.3 Investigating the effect of the number of teeth 106
7.2.4 Experimental investigations 108
8 Conclusion and Future Work 113
8.1 Conclusion 113
8.2 Future Work 116
List of Figures 118
References 124
Formula symbols and abbreviations 141

1 Introduction

The transition towards digitalization in the industrial world is accelerating. Smart components are gradually replacing traditional technologies and gaining more and more recognition for their importance. They bring about the potential for increased lightweight construction, as well as monitoring and enhancing the service life and safety of mechanical and civil engineering structures, both mobile and stationary [MEL16]. Sensor machine components and load-bearing structures enable the digitalization of existing processes and structures. Their objective is to extend classical machine elements with a sensory function. The increasing prevalence of digitalization requires the implementation of smart, advanced sensor components that are able to perform self-diagnosis or calibration, communicate with users, predict maintenance, and estimate remaining useful life based on measured operating data and not only on operating time [AND12].

Recently, significant milestones have been reached in the field of sensor structures. In addition to approaches that introduce sensor structures in specific designs with limited feasibility, standardized commercial sensor machine elements, such as the piezo bolt [CON23], are becoming commercially available. However, achieving the ambitious objective of transforming traditional structures into intelligent ones comes with stringent requirements on the creation of these components. Cost-effective joining methods for adaptable, configurable sensors are a prerequisite for realizing these objectives. In addition, the sensor structures must be manufactured as standardized components, so that they can be implemented with almost no modification to the existing environment and based on the existing knowledge of design engineers [KRA20]. Due to the advancing digitalization, as well as the growing implementation of process monitoring approaches, the employment of force and/or torque sensors is becoming more and more important in many processes. A good example of these are forming processes, where deviations in force distributions due to tool wear can lead to variations in the workpiece characteristics. To monitor the force distribution during the shear cutting process, Groche et al. implemented spatially distributed uniaxial force sensors in the tool assembly [GRO19]. In a similar approach, Kim et al. implemented spatially distributed uniaxial force sensing fasteners on the guidance column of the forging die to detect a non-symmetrical distribution of the process force during the forging process [KIM18]. Fasteners are a good example of multiaxial loaded machine elements. Typically, they are subjected to bending loads in addition to the primary axial and torsional loads [IBR05].

Investigations into sensor integration into host structures through forming have highlighted several beneficial aspects, such as the ability to force and form-fit sensors joining into the structure, as discussed in reference [O1]. However, creating multi-axis sensor structures and machine elements faces process-related challenges and high costs. Krech's dissertation exposed limitations in extending measurement axes of forming integrated sensors into load-bearing structures [KRE20]. In the field of conventional external multiaxial force/torque sensors, the high cost also restricts their application. A tendency to avoid using multiaxial force sensors is reported in the field of robotics, unless their absence would have a serious impact on robotic performance [LEE16].

Many studies have investigated alternative approaches to multi-axis force/torque measurement instead of the dominant and costly strain gauge-based sensors. Optical-based sensors are becoming increasingly popular due to their low cost and simple design. Most studies in the field of multiaxial force/torque sensors that use optical methods typically measure the change in light intensity resulting from the deflection of a structure under load [TAR11], [XIE12]. Meanwhile, optical-based force/torque sensors are commercially available from OnRobot [ONR23]. Nevertheless, the resolution of force/torque sensors based on intensity measurement lags behind that of strain gauge-based or piezoelectric sensors with respect to the required structure deflection.

Adapting optical-based measuring techniques to measure the multi-axial deformation under load in load-bearing structures and machine elements poses two major challenges. First, how can the current measurement resolution be improved in a simple way? Second, how can a high-resolution optical non-contact multiaxial sensor be integrated into mechanical structures, and is sensor integration by forming technology still possible?

2 State of the Art

2.1 Sensor Structures and Machine Elements

Increasing structural safety and improving process understanding to predict machine behavior and product quality are an ongoing goal in the various fields of mechanical engineering. The growing use of sensors in the field of process control and condition monitoring has increased the demand for high quality data that provide higher informative content. Calmano demonstrated that placing sensors in close proximity to the target point of interest increases the data information content [CAL17]. However, this approach presents a big challenge regarding measurability. On the example of a forming machine, placing the sensors on the outer frame of a machine allows for relatively simple sensor integration. It suffers, however, from the poor data content. On the other hand, the information obtained from the component or tool is of high quality, but the integration of sensors in these areas is typically difficult or technically impossible [CAL17].

To enable the placement of sensors near the point of interest, a trend has emerged to extend the functionality of conventional machine elements by integrating sensitive sensor elements. Early proposals in this field includes integrating a strain gauge-based sensor element into a small hole within a bolt [OHT05]. Some works focus on integrating the sensor elements into tool systems, like force measuring in a ball screw drive system through the integration of a strain gauge-based sensor pin [MOE12]. In another area of research, sensor elements are integrated into the metallic structures of machine elements during the manufacturing process, such as the integration of piezoelectric sensors into bolts by means of rotary swaging [GRO14]. The most known approaches are discussed in more detail in the following sections.

2.1.1 Manufacturing process for sensor integration into mechanical structures

The process of integrating sensors into the metallic structures of machine elements can occur during the creation or processing of the metallic structure or through subsequent retrofitting of already manufactured machine elements. When retrofitting sensors to machine elements, the sensor elements are usually inserted into existing or newly created holes. Typical examples are the embedding of strain gauge tubes into bolts by means of epoxy adhesives [OHT05] or the press-fitting of strain gauge-based sensor elements into metallic structures [KRE21]. Alternatively, many studies have considered the embedding of sensor elements into metallic structures during their processing phase to create semi-finished processable sensor metallic structures. As described in detail in [O1], these production processes can be classified into the five main processing groups according to DIN 8580 [DIN22]. The following table summarizes these processes.

Table 1: Manufacturing Process of Semi-Finished Sensor Products Grouped According to DIN 8580

Processing Group	*Process*	*Description*
Primary shaping	Die casting	Thick-film strain gauge transducers are die-cast into aluminum parts [TIE17] [SCH13].
	Ultrasonic additive manufacturing	Optical fibers are embedded into an aluminum alloy [HEH18].
	Laser engineered net shaping	Optical fibers protected with a cladding of cushioning material are embedded onto the surface of a turbine blade [ZOU14].
Welding and brazing	Welding	Ni and Cu coated glass fibers are embedded on a surface of tin coated steel ST-52 with a tin alloy wire [GRA16]; or fiber optic sensors are embedded through layer-by-layer cladding [GRA18].
	Brazing	Brazing alloy is fused to the metallic coating of the fiber [SAN07].
Coating	Coating	Electric polymer-based piezo paints are applied directly onto the surface

		of a host structure for fatigue crack detection [ZHA06].
Forming	Pressing	Micro piezo modules are embedded into micro-structured cavities by means of pressing [SCH14a] [SCH14b].
	Rotary swaging	Piezo- and strain gauge-based transducers are integrated into metallic tubes [GRO11] and fasteners [GRO14] based on recess and infeed [GRO17a] rotary swaging.
	Rolling	A thermoplastic polymer highly enriched with piezoceramic powder is joined with thin metal sheets [KRA15].
Joining	Adhesive bonding	Metal sheets are formed by deep drawing with a piezo module integrated via an adhesive liquid [DRO18].

A comparison of these processes shows that additive manufacturing is still not a cost-effective technology for the mass production of sensor structures, despite its high degree of design flexibility [O1]. Conversely, the high temperatures required for casting, welding, or brazing impose significant limitations on the integration of sensors on thermally isolated elementary sensors, such as thick film strain gauge sensors or specially coated fiber glass sensors [CAV19]. Since machine elements are often exposed to harsh environments where they are already subject to mechanical loads, temperature, and humidity, attaching the sensor material to their surfaces, like painting or even attaching strain gauge films, is limited to special operating conditions. Furthermore, a degradation of the piezoelectric function depending on the process parameters was observed during the post-processability of piezo modules that were adhesively bound to deep drawn sheet metal [MUE16].

The investigated approaches for sensor integration into mechanical structures include joining processes that are capable of integrating ready-to-use sensors, including the necessary electronics. Some of these processes, like joining by forming or press fitting, have demonstrated high suitability in terms of cost-effectiveness and the ability to control and reproduce the sensory properties.

Joining by forming allows for target-oriented pre-stress conditions. In this way, the transducer can be integrated for monitoring and even controlling the joining process. Müller et al. developed an in-process monitoring method for preload evaluation and for fault detection during the integration of piezo modules into micro-structured aluminum sheets [MUE17]. In order to obtain defined preload – and therefore reproducible – sensory properties of the sensor structures produced by incremental forming processes, Krech et al. use the signal of the force transducer that is to be integrated to control the preload during the integration process [KRE18]. Furthermore, it could be shown that by detecting the acting forming forces during sensor integration at the integrated sensor and at a reference point at the forming machine, an in-process calibration of manufactured sensor tubes can be implemented [O2].

2.1.2 Rotary swaging

Rotary swaging is an incremental swaging process for the production of rotationally symmetric components [DIN03]. In certain process designs, the tools hammer radially on a rotating workpiece to achieve a reduction in the cross section of tubular or solid bar stock [GRO07]. Figure 1 illustrates a configuration of a rotary swaging machine. An incremental process involving the rotation of the workpiece and radial oscillation of the four dies achieves a reduction of the workpiece cross section. This motion is initiated by the rotating swaging axis, driving the base jaws, which are equipped with top surface cams. These cams interact with the cylinder rollers to push the dies inward. The swaging head has 12 cylinder rollers. Included in these components are dies, spacers, base jaws with cams, and cylinder rollers [ISH19].

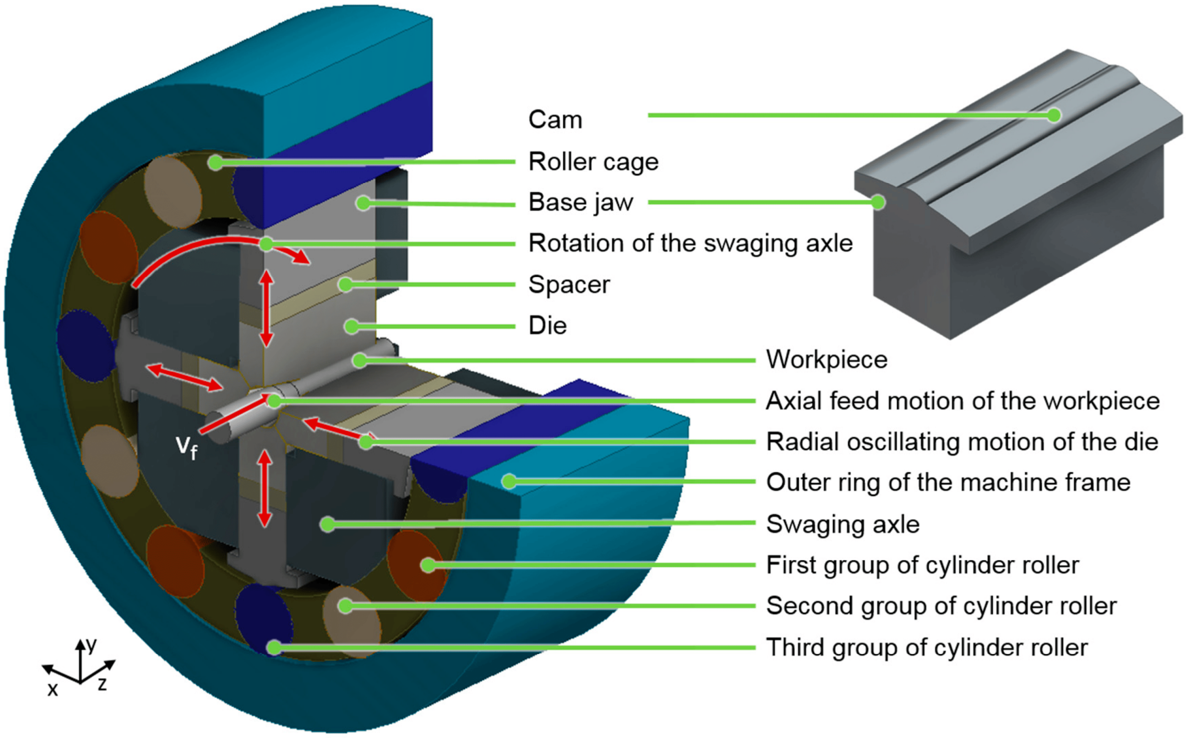

Figure 1: Illustration of the Rotary Swaging Unit [ISH19]

Two different process types of rotary swaging can be distinguished: (1) infeed rotary swaging and (2) recess rotary swaging. In infeed rotary swaging, the workpiece is fed into the dies at speed V_f, as shown in Figure 1. During recess swaging, the workpiece remains stationary in the axial direction, while the dies gradually progress in the radial direction to the final dimensions.

In addition to the radial forming forces imposed by the dies, axial forming forces also occur in rotary swaging as the workpiece moves forward into the dies. In both cases, torsional moments arise due to the workpiece rotation while the tools engage the workpiece. In his numerical studies, Rathmann showed the influence of the angle of rotation per stroke α_H on the resulting angle of twist at the workpiece [RAT07], Figure 2.

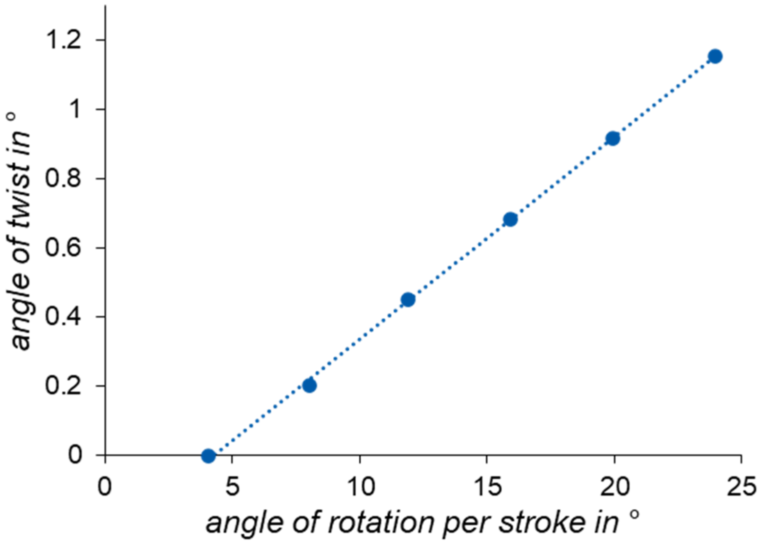

Figure 2: Influence of the rotation per stroke α_H on the resulting angle of twist according to [RAT07]

As shown in Figure 2, the resulting angle of twist increases linearly with an increasing angle of rotation per stroke. Here, the angle of rotation is defined as

$$\alpha_H = \frac{f_{rot} \cdot 360°}{f_{sw}}$$

where f_{rot} is the frequency of workpiece rotation, and f_{sw} is the swaging frequency, defined as the number of tools strokes per second.

2.2 Multiaxial Force/Torque Measuring

2.2.1 Strain gauge-based multiaxial force/torque sensors

Force and torque sensors are used in a wide range of applications, from medical to industrial to aerospace. With the continued advancement of digitalization, the spectrum of applications has significantly expanded. The review of current research on multi-axis force/torque sensors shows a clear dominance of strain gauge-based measuring techniques [TEM20]. In this type of measurement technique, strain gauge films are attached at various places on an elastic deformable structure. Important sensor properties, such as sensitivity, sensor accuracy, measurement range, and crosstalk between the measurement axes, depend significantly on the deformation behavior of the elastic element and the sensitive elements [XIO18]. The elastic element and the attachment of the strain gauges can have various designs depending on the system requirements. Figure 3 shows an overview of the basic design types of elastic elements depending on the type of load-induced stress.

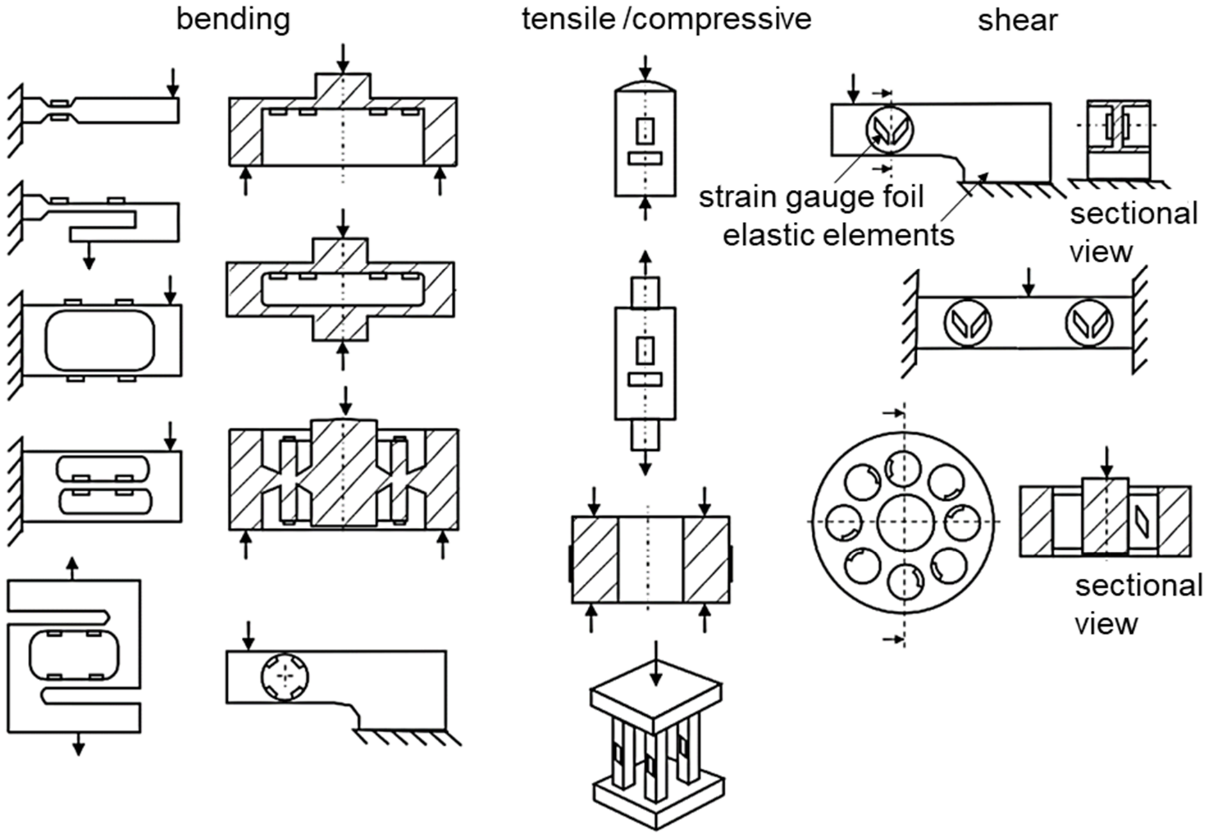

Figure 3: Basic types of elastic elements in strain gauge force/torque sensors based on the load-induced stress according to [GEV06].

As the number of measurement axes increases, the complexity of the sensor design also rises, especially since the crosstalk between the individual measurement axes cannot be completely eliminated [LIB75]. This results in a higher number of strain gauge films, a more complex design of the sensor's elastic elements and associated electronics, and more extensive calibration approaches [LIB75]. To date, many design guidelines have been developed to reduce crosstalk and enhance measurement accuracy by ensuring anisotropic or decoupled deformation behavior of the elastic element under load, as discussed in [HU18], [LIN20] and [KAN14]. This is usually achieved by optimizing the mechanical sensor design along with a certain distribution of the sensing elements. For example, Akbari et al. present a numerical shape optimization technique for improving the coupling errors of a so-called Maltese crossbeams type six-axis force/moment sensor. The proposed technique involves modifying the geometry of the sensor to reduce coupling errors while maintaining its sensitivity [AKB18]. An example of a sensor design for a six-axis force/torque sensor is shown in Figure 4. In the sensor design according to Ishkina et al., the elastic body consists of four elastic beams. The beams are connected by a square platform in the center with four elastic edges. The tool attaches to the upper flange, transmitting forces and moments to the elastic body via a square platform. The lower flange serves as both an end cap and elastic body support. For this design, a total of 32 strain gauges are installed [AHM21].

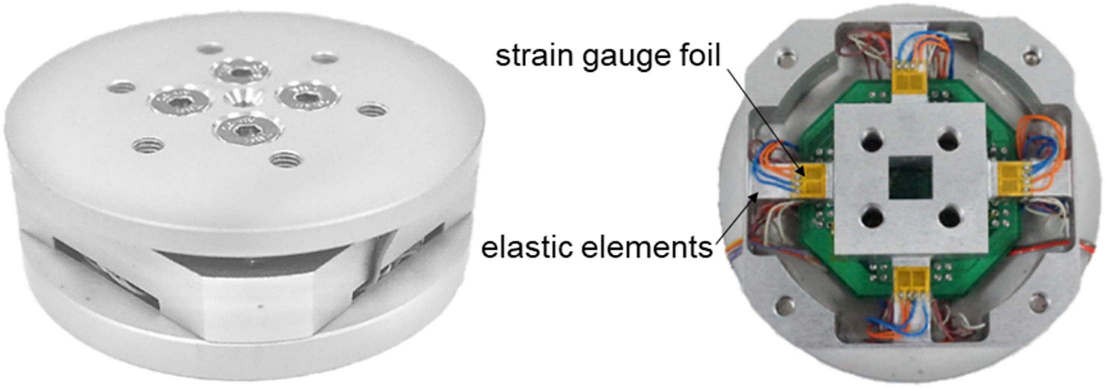

Figure 4: Design of a strain gauge-based six-axis force/torque sensor [AHM21].

In addition to the typical metal foil strain gauge elements, alternative sensing elements, like semiconductor strain gauge [HON12] and [ZHA16] or fiber grating [XIO18] and [LVS20] are sometimes used. However, the resulting overall high cost of strain gauge-based multiaxial force/torque sensors has prevented rapid implementation in many applications.

The price of six-axis force/torque sensors depends mainly on the achievable measurement accuracy, by, among other things, compensating for the crosstalk behavior between the measuring axes. In his research on the price of multi-axis force/torque sensors, Malicevic has shown that the price of sensors from ATI and Me-Systems, for example, ranges from €4,000 to €30,000, depending on the accuracy class [S1].

2.2.2 State of the research on alternative measuring concepts

Many researchers focus their efforts on reducing the design complexity and overall cost of multi-axis force/torque sensors. Some researchers aim, on the one hand, at minimizing the cost of strain gauge-based transducers through new design approaches, such as a three-axis force/torque sensor with only four strain gauges and a switchable quarter-bridge and only one voltage amplifier [BIL21]. On the other hand, many researchers have introduced new sensors based on alternative measuring concepts, such as capacitive [KIM20] or optical transducers.

A discernible trend in recent times has been the development of multi-axis force/torque sensors based on optical measurement technologies. In particular, optical-based non-contact sensors offer a low-cost, simple design and facilitate structural integration while avoiding the strict design requirements of the elastic elements in strain gauge-based sensors. These sensors detect displacements or structural deformation through intensity changes, unlike electromechanical sensors that rely on local strain measurement.

In the field of optical force/torque measurement, Tar et al. presented a 3D tactile force sensor in which light emitted by LEDs is received by reflective deformable hollow rubber hemispheres and reflected into light-emitting diodes. The magnitude and direction of the grip force is then determined by the change in intensity at the light diodes. This enables force sensing in the compliant gripper of a robot with a stable grip [TAR11]. A similar principle of operation is presented by Noh et al. in the form of a three-axis force/torque sensor for easy installation in the structure of a manipulator arm [NOH16]. Al-Mai et al. presented, firstly, a three-axis, and then later a six-axis, fiber optic force/torque sensor in which the generated and reflected light is propagated with high accuracy and low noise through a pair of optical fibers from the LED to the mirrors and then back to the photodiode [ALM17] and [ALM18]. Xie et al. adopted the optical measurement concept due to the requirement of application in a magnetic resonance imaging (MRI) environment where no metallic component could be used. Unlike the previous measurement concepts, where the change in light intensity and thus the displacement due to load was measured by evaluating the proportional voltage value of the applied photodiodes, in Xie et al.'s approach, the intensity change was pixel-based and measured with a camera [XIE12].

Díez et al. presented an optical force sensor based on a different measurement concept, where the load on the structure causes the displacement of a built-in converging lens. The light distortion caused during the lens displacement is measured by a 2x2 photo-detector matrix and interpreted as a bending proportional signal [DÍE18]. Commercial optical-based multi-axis force/torque sensors are also being promulgated, such as the OptoForce sensor from the robotic gripper company OnRobot [ONR23]. Figure 5 shows some multiaxial force sensors based on the principle of optical intensity variation.

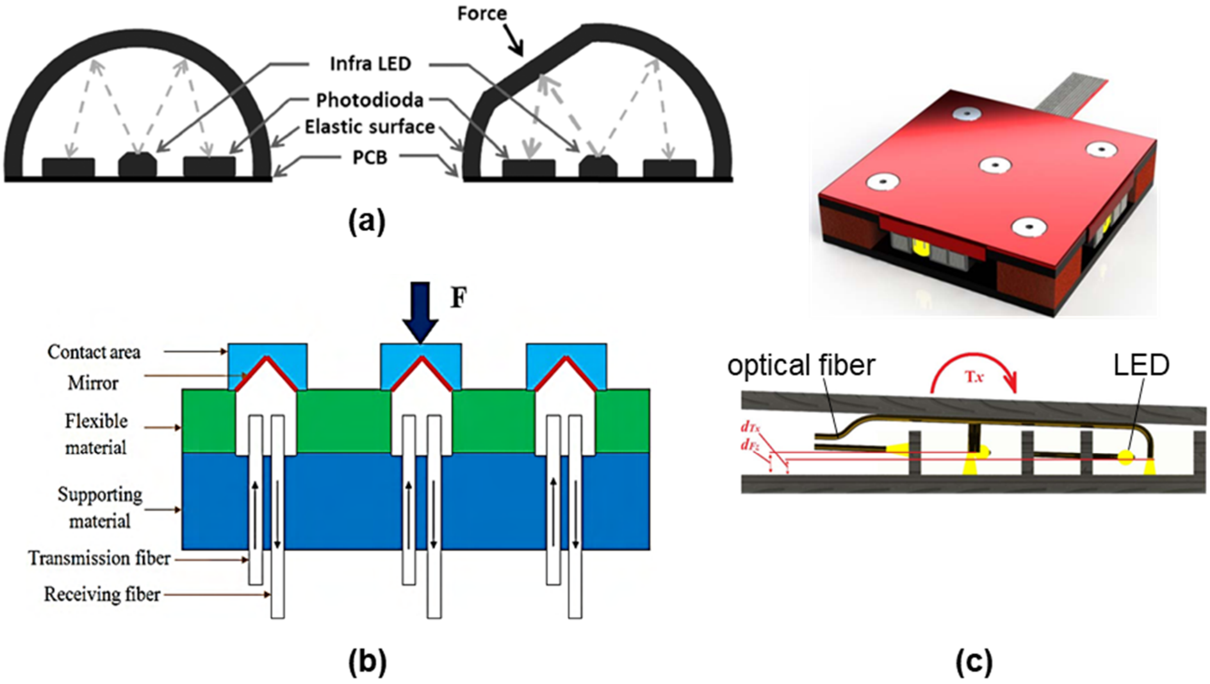

Figure 5: Optical intensity based multiaxial force sensors. (a) The deformation of the internally reflecting rubber hemisphere results in a different intensity pattern in the photodiodes [TAR11]; (b) as the distance between the mirrors and the optical fibers changes, the intensity of the reflected light changes proportionally [XIE12]; and (c) changing the distance between the fiber tip and the respective mirror results in changes in the intensity of the light detected by the photodiodes [ALM17] .

As shown in Figure 5, all these measurement concepts are based on the direct evaluation of the change in intensity as a quantity proportional to the load condition. Despite the mainly economic advantages of optical intensity sensors in terms of more flexible and lighter designs, the structures must be sufficiently compliant to produce measurable displacements. Hence, optical sensors are mainly used for force measurements on more compliant structures, such as plastic and rubber. Their measuring resolution, in terms of the required deformation, is quite far behind the achievable performance of conventional strain gauge-based or piezoelectric sensors. According to Berkovic et al., an optical sensor with higher resolution, for example, in the range of one µm, requires relatively expensive and complex measuring technologies, such as interferometry or confocal sensing [BER12]. When it comes to sensors with resolution comparable to strain gauge sensors, the most common are all fiber-based force/torque measurement methods [WOL23], which, however, similar to the strain gauges, measure the local strain instead of the resulting displacement.

2.2.3 Multiaxial sensor machine elements

In the field of mechanical engineering, for instance, many machine elements are subjected to complex loads during their use phase, which can lead to fatigue-related degradation. Fasteners are a typical example of such machine elements. They are usually subjected to bending loads, in addition to the primary axial and torsional loads [IBR05]. In turbine shafts, a combination of torsion and bending loads may lead to the development of cracks [MOM12]. As visualized in Figure 6, fasteners in the one-sided flange profile of a wind turbine tower are subjected to cyclical bending forces, resulting in the loss of preload [LI23]. For this reason, the preload of the bolts in a wind turbine is regularly inspected.

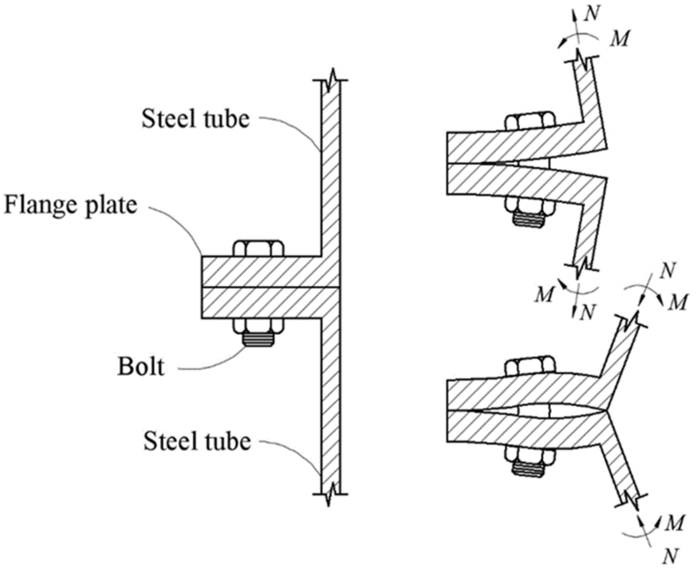

Figure 6: Multiaxial load conditions borne by fasteners in a wind turbine tower [LI23].

Current research includes approaches to the design of multi-axis sensor bolts. Some are based on strain gauge technology, such as attaching strain gauge films to a wind turbine M73 bolt [SCH21] or screwing a strain gauge-based sensor into an M20 bolt [HER22]. Alternatively, Wolf has shown how a torsion and bending sensor bolt can be achieved by using a laser beam traversing a total reflection prism rod integrated into the bolt [WOL23]. Figure 7 below depicts examples of these technologies.

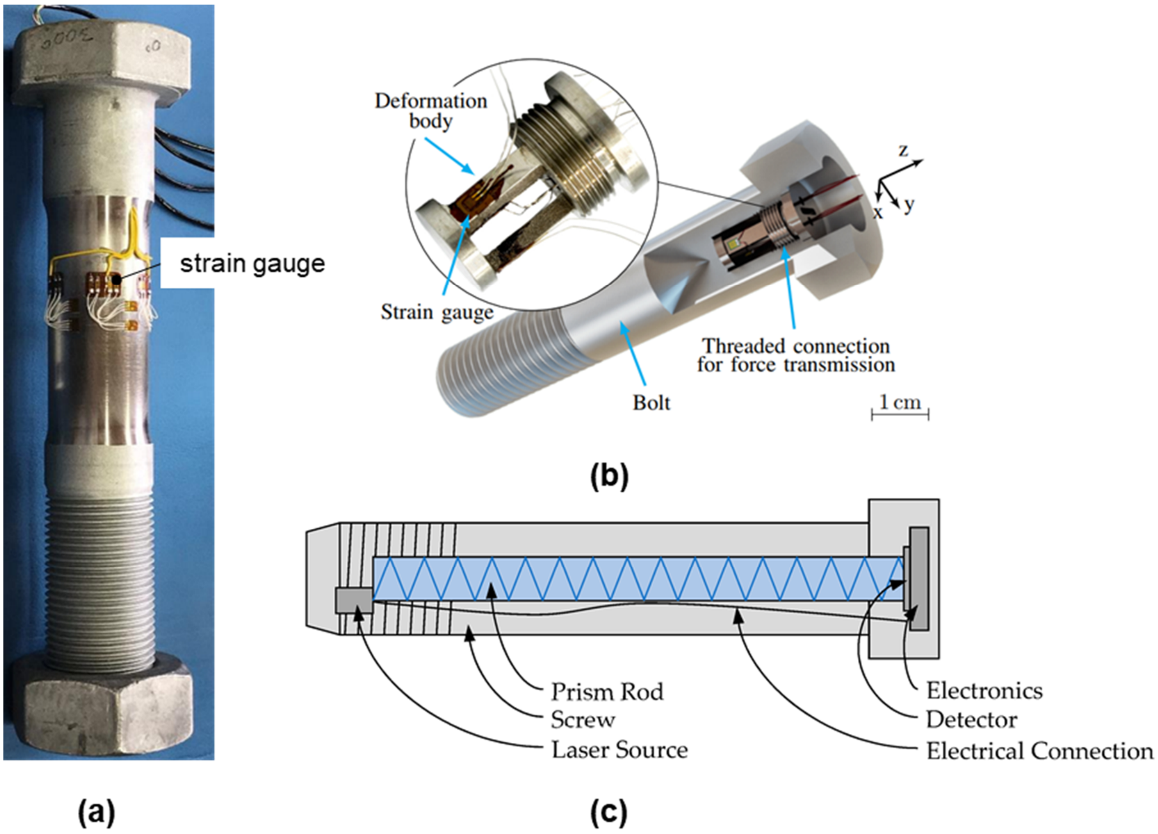

Figure 7: Multiaxial sensor bolts that function (a) by external attachment of strain gauge films on an M72 Bolt [SCH21]; (b) by screwing a strain gauge sensor inside an M20 bolt [HER22]; and c) by the integration of a laser source and a prism rod into the bolt [WOL23].

Particularly in the case of structurally integrated approaches, multiaxial load sensing at present appears to be very critical because of the associated reduction in the strength of the bolt. Herbst et al. reported a 23.5% decrease in the mechanical strength of the bolt [HER22].

2.3 Relevant Fundamentals of Imaging Systems

Camera modules are present in many consumer electronic devices, such as smartphones, computers, and tablets, and this market is expected to grow significantly over the next few years [STE12]. In terms of industrial application, camera systems for image-based quality and process monitoring are attracting more attention and becoming a growing trend in the manufacturing industry [SMI21]. The use of industrial cameras and machine vision typically includes applications for detecting objects in images and extracting quality or process features [PER13]. The simplest imaging system consists of an image sensor and a lens system that focuses and, if necessary, magnifies an object on the surface of an image sensor. Figure 8 shows a standard camera assembly.

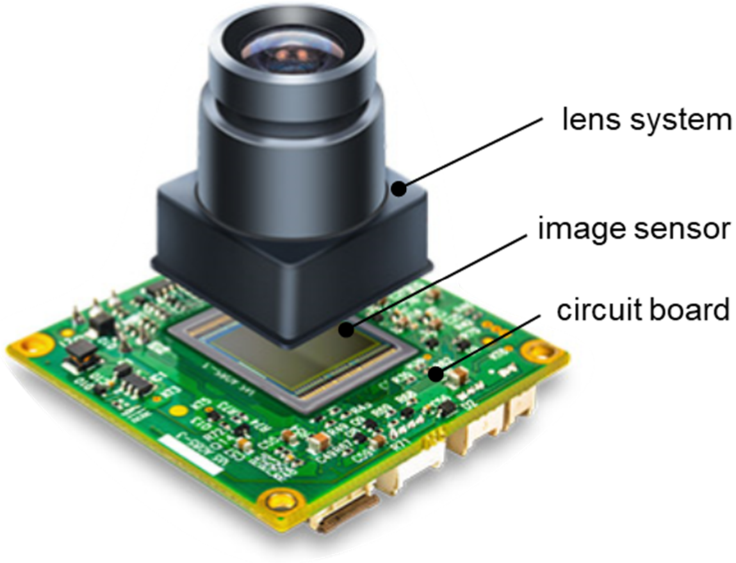

Figure 8: Visualization of the camera assembly according to [PRO23].

2.3.1 Lenses and optical magnification

Lenses are considered to be the most fundamental and widely used components of optical imaging systems [HEC18]. Their refractive indexes allow incident light to be redirected in a specific way. The refractive index of a lens and, in general, its optical properties are adjusted by both the lens material and by its geometry, such the radius of curvature [LIT05]. If a ray parallel to the axis of symmetry is incident on a curved surface with a radius of curvature R and a refractive index n_2, it will be directed forward and intersect the axis of symmetry of the lens at the focal point F [DEM09]. See Figure 9.

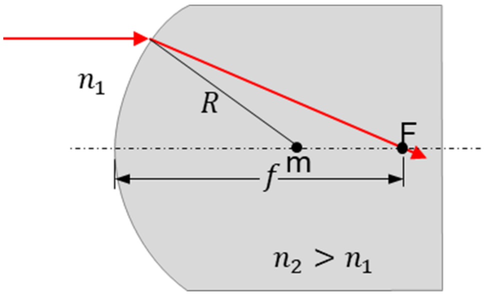

Figure 9: Definition of the focal length in a spherically curved interface according to [DEM09].

With n_1 as the refractive index of air, the focal length of a lens f is obtained by

$$f = \left(\frac{n_2}{n_2 - n_1}\right) \cdot R$$

where R is the curvature radius, and n_2 is the refractive index of the lens.

Based on their thickness, lenses can be categorized as either thick or thin [DEM09]. A thin lens is an idealized model of a real lens in which the maximum lens thickness is very small compared to its focal length. Therefore, the mid-plane of a thin lens is considered to be the principal plane when determining its focal length. In a thick lens, there are two principal planes, resulting in a front focal length and a back focal length [DEM09], as shown in Figure 10.

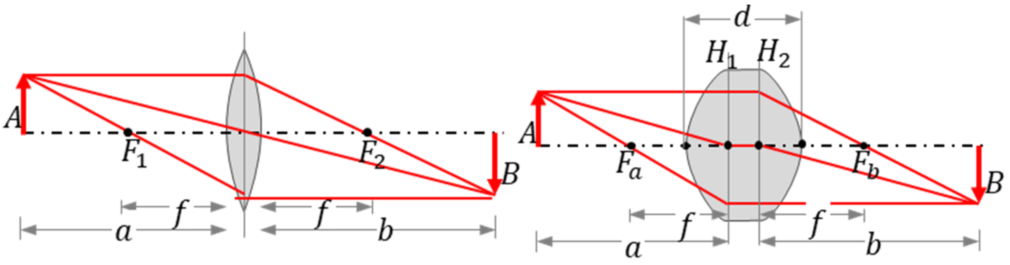

Figure 10: Determining the focal length in thin and thick lenses, according to [DEM09].

As shown in Figure 10, when designing a lens system, the distance a between the lens and the object A and the distance b between the lens and the image plane B depend on the position of the lens' principal planes. From these distances, the optical magnification M achieved by a lens is given as

$$M = \frac{-b}{a} = \frac{f}{f - a}$$

Optical multi-lens systems

Since the use of a single lens is typically limited by the presence of optical aberrations, optical systems are usually designed with lens combinations to achieve higher image quality [DEM09]. The combination of different lenses allows optical aberrations to be corrected, balanced, or minimized [SAS19]. As noted in the field of microscope objectives, lens design is usually challenging, and their design principles are limited to specialized designers in a few optical companies [ZHA19a]. However, certain lens systems, including zoom, telephoto, and telescopic lenses, have been shown to be effective in a variety of low complexity applications [MAL14]. Zoom lenses are an example of such lens systems and are commonly used in many optical applications, such as still cameras and smartphone cameras [BLA21]. These optical systems are known for their flexibility in adjusting the optical magnification and focal length at a fixed system length. In the simplest structure, the system consists of two biconvex lenses and one biconcave lens, as shown in Figure 11. The optical system can be designed through theoretical analysis of the paraxial imaging properties, as demonstrated in [CHE21]. Simply by moving the middle biconcave lens within the space between the two biconvex lenses, the system’s focal length, and the resulting optical magnification, can be adjusted within a certain range.

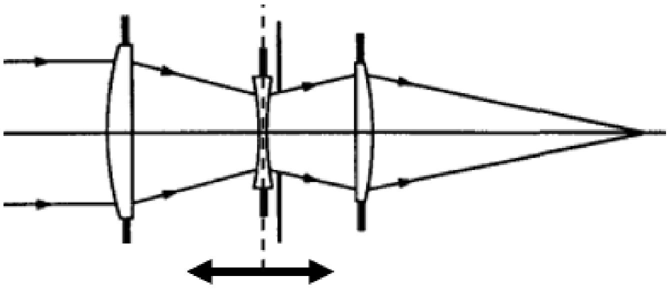

Figure 11: Three-lens zoom lens system [MOU97].

In Malicevic’s experimental studies, a bi-convex lens pair with a focal length $f = 30\,mm$ and a bi-concave lens with a focal length $f = -100\,mm$ were used to analyze the optical system. The length of the system was varied between 90 and 150 mm, while the position of the center bi-concave lens between the two lenses was adjusted. This resulted in the ability to adjust the optical magnification between $M = 1$ and $M = 4$ [S1], as shown in Figure 12.

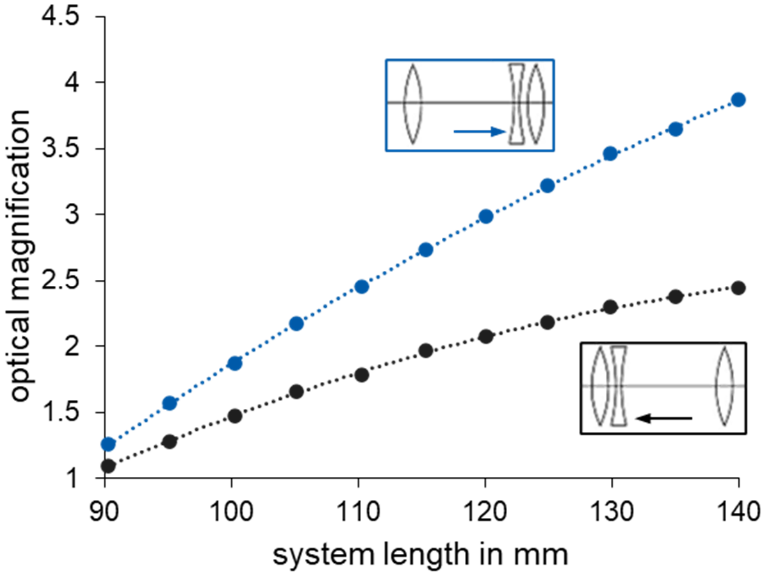

Figure 12: Adjusting the optical magnification in a three-lens zoom system, according to [S1].

As shown in Figure 12, both increasing the system length as well as moving the middle biconcave lens between the two biconvex lenses allow the system's optical magnification to be increased. Here, the upper curve is determined by where the biconcave lens attaches to the biconvex lens on the image side, and the lower curve is determined by where the biconcave lens attaches to the biconvex lens on the object side.

Optical aberrations

The performance of an optical system is usually limited by the presence of aberrations. In reality, a whole series of aberrations occur that limit the imaging quality. According to [NAK05], optical aberrations can be classified as either monochromatic or chromatic. The five types of monochromatic aberrations are as follows:

1. *Spherical aberration:* caused by the fact that the lens surface is spherical
2. *Comatic aberration*: a coma-like flare with a tail for a point light source off the optical axis
3. *Astigmatism:* causes a point light source to be projected as a line or ellipse instead of a point
4. *Curvature of field*: causes the focal plane to curve in the shape of a bowl, so that the periphery of the image is out of focus

5. *Distortion*: aberrations that distort the image

The two types of chromatic aberrations are as follows:

1. *Longitudinal chromatic aberration* refers to the fact that different colors (wavelengths of light) have different focal points.
2. *Lateral chromatic aberration* refers to the fact that different colors have different magnification rates.

Figure 13 illustrates the effects of these aberrations on the incoming rays from the object at the image plane. Further details regarding these aberrations can be found in the respective reference works.

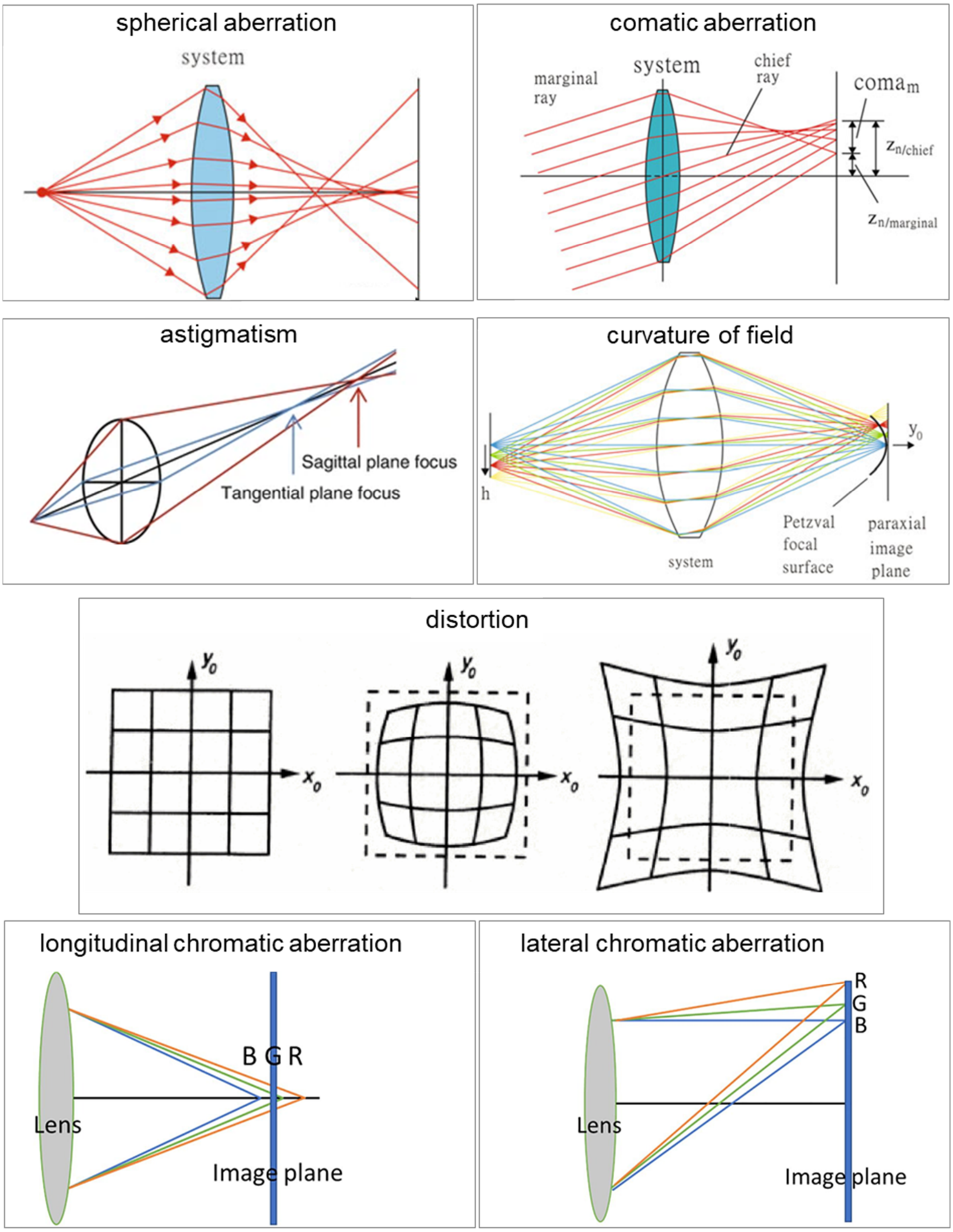

Figure 13: Effects of aberrations on the incoming rays from an object on the image plane. Spherical and comatic aberration [LIN17], astigmatism [WRI17], curvature of field [LIN17], distortion [PAR09] and longitudinal and lateral chromatic aberration [GOH21].

Optical simulation programs, such as ZMAX, OpTaliX, OpticStudio, and Oslo, play a pivotal role in lens system design and the optimization of aberrations. These software tools facilitate the simulation and validation of optical designs for specific parameters, including lens type and aperture diameter [SAS19]. Many computations within lens design software rely heavily on first-order ray tracing, encompassing tasks like determining the ideal image position and size, locating pupils, and establishing cardinal points. First-order ray tracing simplifies optical surfaces as flat but endowed with a specific optical power, allowing for the rapid calculation of basic optical parameters while minimizing computational time. In contrast, real ray tracing meticulously accounts for the actual specified surfaces with a high degree of accuracy [SAS19].

Aberrations in an optical system are, for example, evaluated by means of so-called spot diagrams. These diagrams are generated by tracing a designated number of rays through the optical system to the image plane. The points where these rays intersect with the image plane are represented by small circles or squares [GUE15]. The spot diagram effectively depicts how an optical system responds to a point object. Optical aberrations can be mitigated through various means, including modifications and improvements to the lens system as described in [SAS19] or even through digital image processing [SHA20].

Figure 14 illustrates an example of how optical simulation software can be used to visualize the aberrations that occur in a very simple optical system consisting of a single biconvex lens. Figure 14a depicts a ray tracing of two field points, one situated on the optical axis and the other off the optical axis. In Figure 14b, the corresponding spot diagram displays transverse aberrations when defocusing the distance between the object and lens horizontally by -0.5 to 0.5 mm and vertically adjusting the position on the image side between 0 and 5 mm [GRO05].

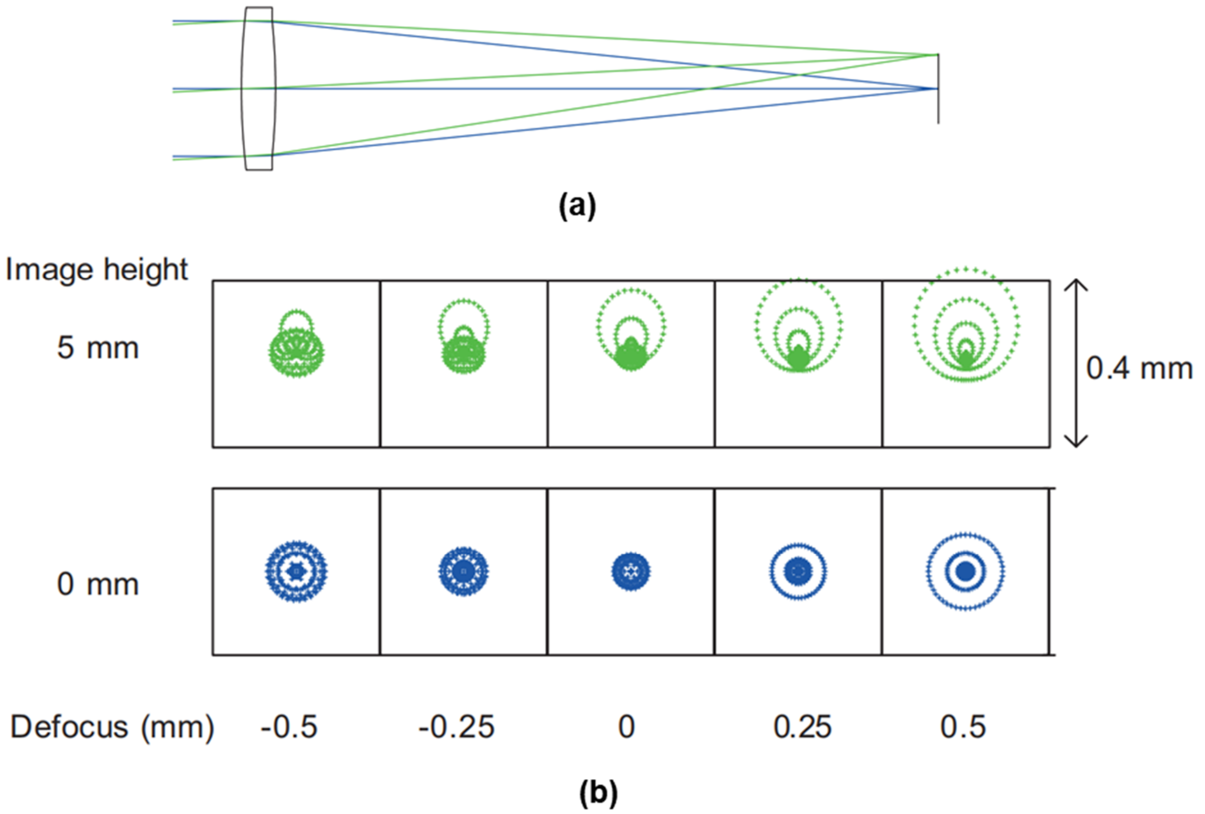

Figure 14: Simulation of optical systems: (a) ray tracing of two field points and (b) the associated spot diagram [GRO05].

2.3.2 Photomasks

Photomasks consist of a transparent substrate, typically plastic film, glass, or quartz, coated with a thin layer of a light-blocking material, such as chromium [RIZ18]. They are typically used in the semiconductor industry to transfer intricate patterns onto semiconductor wafers during the manufacture of integrated circuits (ICs) and other microelectronic devices [DON17]. This process is known as photolithography [GEI04]. Photomasks and light projection are used to transfer circuit patterns onto the wafer’s resistant film. This process collectively facilitates the creation of complex integrated circuit patterns, which serve as the foundational basis for modern electronics and technology [LEV19]. Sun and Hsiao used a backlit photomask to increase the accuracy of measuring the density of microfluidic mixtures in a technique called background-oriented schlieren. Their research demonstrates the advantages of using backlighting with small, precisely positioned and sized features to increase measurement accuracy [SUN14]. Figure 15 shows the use of the photomask for background schlieren techniques, as well as an exemplary microscopic image of a photomask.

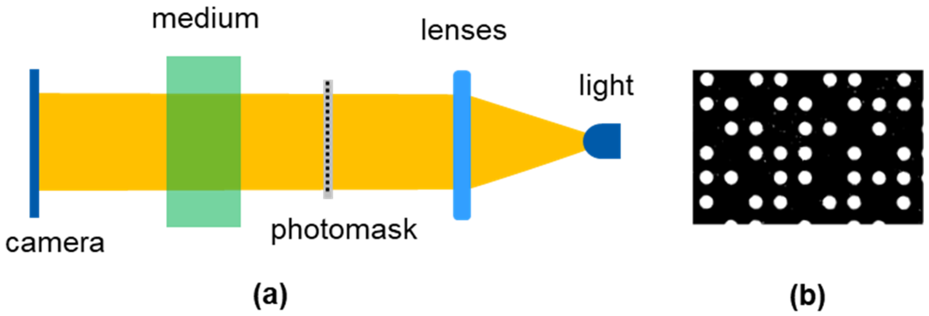

Figure 15: Use of the photomask for background schlieren techniques (a), system design according to [SUN14], and (b) a photomask consisting of pre-defined circles on a black background.

2.3.3 Image sensors

An image sensor consists of a two-dimensional area of small pixels, where each pixel consists of a photodiode made of silicon [NAK05] and acts as a single photodiode sensor. Based on the photoelectric effect, these pixels convert the incident photons into an analog electrical charge. This charge is amplified and converted to a brightness value by a built-in circuit [DAK18]. As a pixel only captures the intensity of light as monochromatic image information, color information is recorded using a color filter array applied to the surface of the image sensor, allowing only light with a predefined wavelength to pass through to the pixel. An on-chip micro-lens array (OMA) focuses the incident light onto the photodiode, and it is applied directly to the surface of the color filter layer [NAK05]. Figure 16 shows the simplified structure of a pixel in an image sensor.

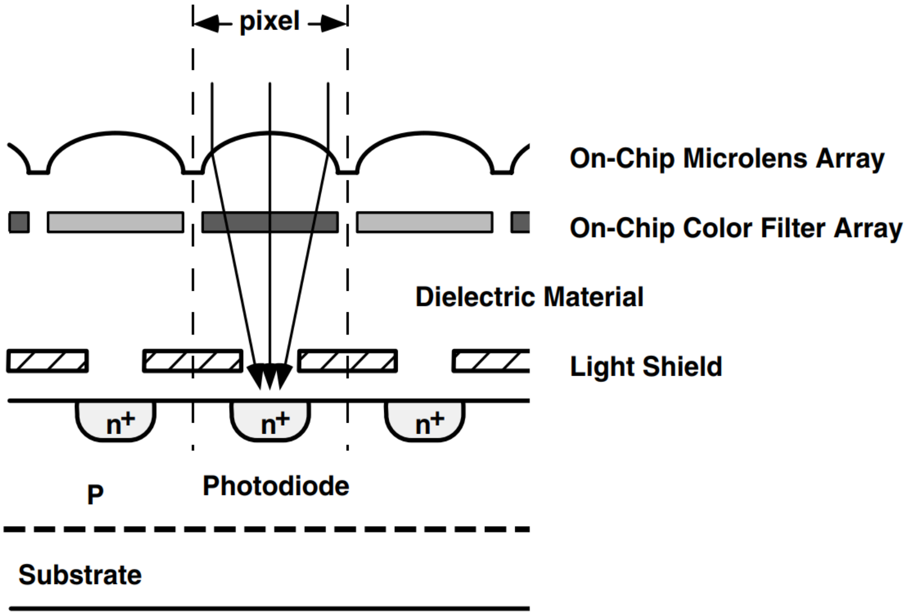

Figure 16: Cross-sectional view of an image sensor [NAK05].

Different patterns of filter arrangement, such as RGB, CFA, or Bayer, are used. They are distinguished by the distribution of the red, blue, and green color filters. After reading the image from the different pixels, the color components are interpolated to the whole image using special demosaicking methods, as shown in [GUN05]. As a result, three color matrices are generated: red, green, and blue. Figure 17 shows color patterns and the resulting color matrices.

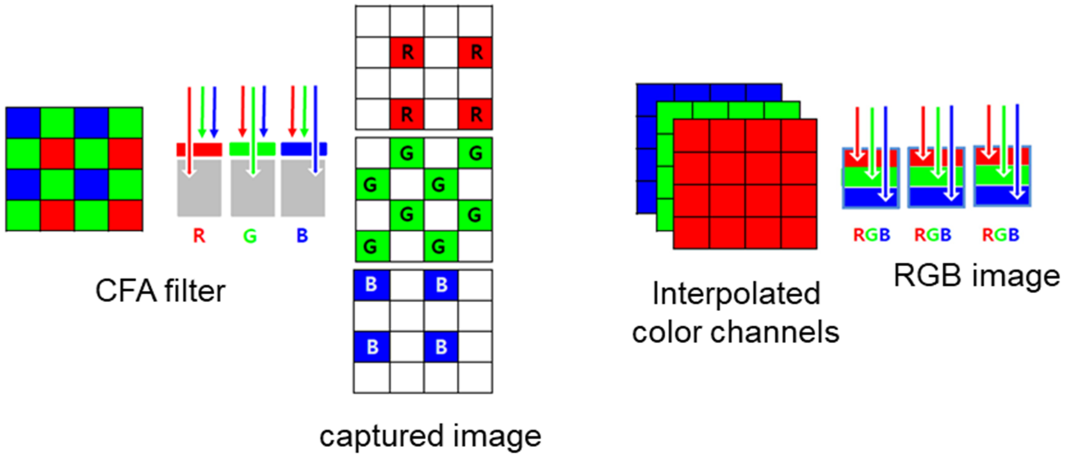

Figure 17: Capturing colored images using a color filter, according to [PAR22].

The most common image sensor technologies are charge coupled device (CCD) and complementary metal oxide semiconductor (CMOS). Historically, CCDs have been the dominant image sensor technology. Recent advances in semiconductor technologies and the increasing use of image sensors in high-volume products, such as optical mice, PC cameras, mobile phones, and high-end digital cameras, have prompted the quest for suitable alternatives to CCDs [ELG05]. The architecture of CCD and CMOS sensors differs primarily in two aspects: the method of signal transmission and the method of signal readout. The structures of CCD and CMOS image sensors are illustrated in Figure 18.

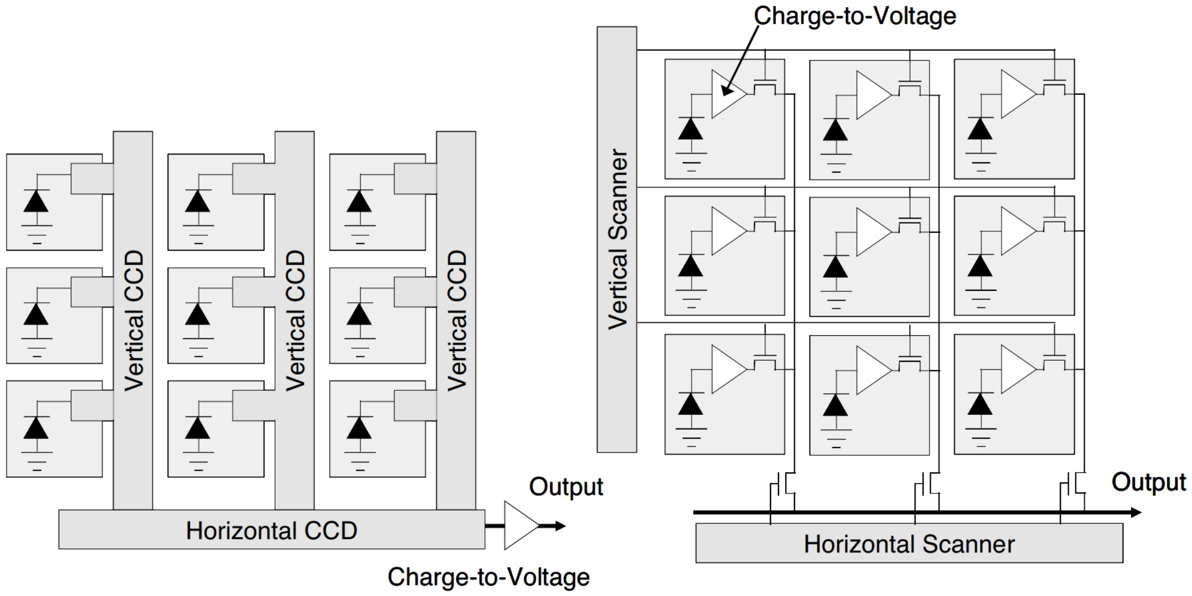

Figure 18: Structure and signal transmission in image sensors: CCD sensor (left) and CMOS sensor (right) [OHT20].

As can be seen in Figure 18, a CCD sensor transfers its pixel signal charges to the end of the output signal line and then converts them to a voltage signal using an amplifier. A CMOS image sensor, on the other hand, converts the signal charge into a voltage signal directly at each pixel before transferring them to the scanner. In terms of high-speed operation, the in-pixel amplification configuration of CMOS sensors offers superior gain bandwidth compared to the single amplifier on-chip configuration in CCDs. In CCD sensors, the signal charge is transferred simultaneously, resulting in low noise but high power consumption. In addition, this simultaneous transfer ensures that each pixel has the same accumulation time at any given time. In contrast, CMOS sensors convert the signal charge at each pixel and read the resulting signals row by row, resulting in different accumulation times for pixels in different rows at any given time. This is commonly referred to as the *rolling shutter* effect [OHT20].

For high-speed applications, rolling shutter CMOS sensors present a disadvantage, since moving objects are affected by motion blur. In recent years, CMOS sensors with global electronic shutters have been developed, especially for industrial machine vision applications [BLA21]. Generally, the manufacturing techniques of CMOS sensors facilitate increasing performance in terms of higher frames per second, increasing sensor area, decreasing the pixel size, and increasing on-chip feature integration [LU22].

2.4 Basics of Image Processing and Machine Learning Algorithms

In addition to the increasing performance of CMOS image sensors, recent developments in image processing algorithms have contributed to the widespread use of camera systems in industrial applications. Many industrial inspection and monitoring tasks, such as feature recognition or object tracking, can be accomplished with simple cameras by applying a variety of image processing techniques and computer vision algorithms. In the field of computer vision, template matching is a high-level method to determine the position of a predefined sub image, called a template, in a whole image using different matching algorithms [SWA16]. The use of template matching in computer vision is widely extended, for example, in traffic monitoring, fault detection in production lines, facial recognition, and medical pattern recognition algorithms [JIA21].

2.4.1 Digital image correlation (DIC)

In the field of stress analysis in solid mechanics, high-resolution optical techniques – such as holographic interferometry, speckle interferometry, and moiré interferometry – are used to measure strains occurring under structural loading, for example, to determine the material flow curve. However, digital image correlation (DIC) as a non-interferometric technique has gained more and more attention in recent years due to its comparatively lower cost and easier measurement setup [S2].

In the classical applications of DIC for strain measurement, the surface of an object of interest is prepared by applying a random speckle pattern. The pattern serves as an information carrier and is expected to have unique, non-periodic and stable greyscale features. For this purpose, methods like spraying, spin coating, and lithography exist [DON17]. To avoid aliasing, a maximum speckle size of 3x3 pixels is desired [REU14]. Subsequently, the coordinates of the subset with a predefined area in the reference image are selected and then sought in the target image within a predefined area there. The correlation values for the whole search field are stored in a correlation matrix, and the coordinates of the highest correlation value are assigned to the new position of the searched subset center. Small subsets increase the risk of misclassification because the uniqueness decreases. However, for small subsets, the local strain excesses can be measured with higher resolution [YAO07]. The size of the subset and the search field, in particular, have a strong impact on the computation time [PAN06]. The following figure illustrates the principle of DIC. First, the region of interest – the subset – is defined by its subset center and subset size. The resulting square, with its corresponding pixel values, is searched in the target images using a correlation algorithm that moves it over the target image pixel by pixel and stores the resulting correlation value in a correlation matrix, as shown in Figure 19. A correlation value describes the similarity of the target image to the subset at each iteration step.

After the last pixel shift in the target image, the position of the maximum correlation value is determined as the new subset position in the target image. Figure 19 illustrates the working principle of DIC for strain analysis.

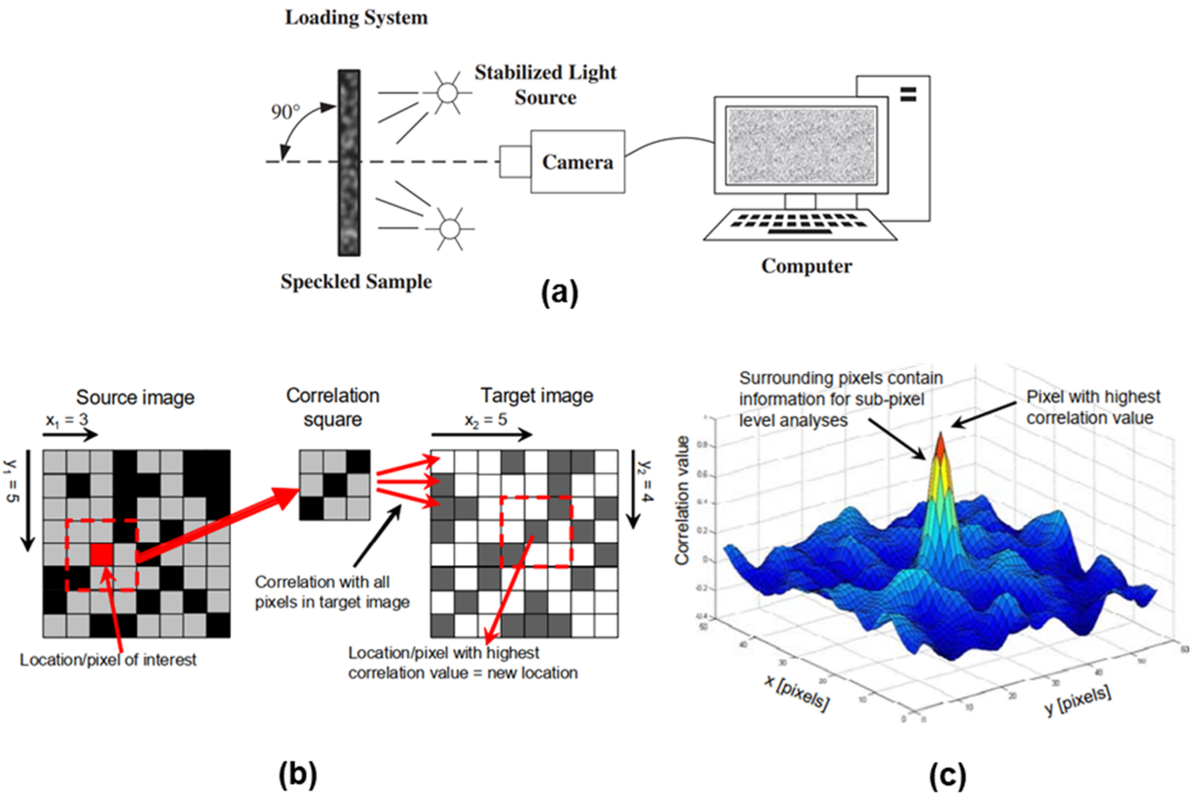

Figure 19: Visualization of the working principles of DIC: (a) set-up for strain analysis [ZHA19b], (b) correlation process for a subset of one pixel, and (c) the resulting correlation matrix [LEM08].

Expanding the field of application of the DIC has led to the development of specialized algorithms designed to achieve high resolution while minimizing systematic errors [MIC09]. As summarized in [S2], the correlation value can be calculated using many algorithms, such as cross-correlation [GIA00], sum of least squares difference [TON05], Fast Fourier Transform (FFT) [GRE10], and optical flow [SUT08]. After determining the position of the best match in the target image, the accuracy of the new position can be increased in the resolution of a few subpixels. For example, Yang et al. achieved measurement resolutions as low as 0.01 pixels to increase the measurement resolution in dynamic testing of microelectromechanical systems (MEMS) [YAN06]. In [KOK15], a shift of the micromechanical device with a measurement accuracy within the picometer range could be achieved by applying optical magnification. As can be seen in the correlation matrix in Figure 19c, the correlation values around the max value can increase the measurement accuracy to the range of subpixels. One way to achieve this is by interpolating both the subset and the target image to the required subpixel resolution and then calculating the correlation by means of the typical correlation algorithm [BOR17]. Since this is, however, computationally expensive, algorithms have been developed to optimize the search in subpixel increments. Most common algorithms for subpixel correlation are coarse to fine search algorithms [YAN06], peakfinder algorithms [HUN03], iterative spatial domain algorithms [BRU89], spatial gradient-based algorithms [ZHA03], continuum methods [CHE02], and swarm and population-based optimization [PIL04]. Application of the algorithm depends mainly on the demands and the type of application. Typical criteria include: the size of the search field, desired accuracy, subset size, and computing efficiency. However, the normalized variants of the cross-correlation and least-squares difference algorithms are typically more widely used due to their high robustness to variations in illumination [PAN09].

Despite the fact that DIC is presently one of the most widely used techniques in the field of experimental mechanics with the lowest requirements for an operating environment, its measurement accuracy as a non-interferometric method is highly dependent on the illumination conditions during the measurement. Variations in the illumination conditions, and thus in the quality of the acquired images, directly affect the measurement quality [PAN12]. Usually, very strong illumination is required to achieve high resolution.

2.4.2 Convolutional neural networks

According to [ALZ21], convolutional neural network (CNN) is the most famous and commonly employed algorithm in the field of machine learning. Similar to traditional Artificial Neural Networks (ANNs), CNN algorithms consist of neurons that improve their performance by learning [SAX22]. Each neuron receives input and performs operations, typically a scalar product followed by a nonlinear function, which is the basis of many ANNs. The only significant difference between CNNs and traditional ANNs is that CNNs are primarily used for pattern recognition within images. By encoding image-specific features into the architecture, CNNs become more adept at tackling image-based tasks, consequently minimizing the parameters necessary for setting up the model [SAX22]. A typical CNN, like other neural networks, consists of an input layer, an output layer, and many hidden layers: convolutional layer, pooling layer, and fully connected layer. Figure 20 shows the basic architecture of a CNN.

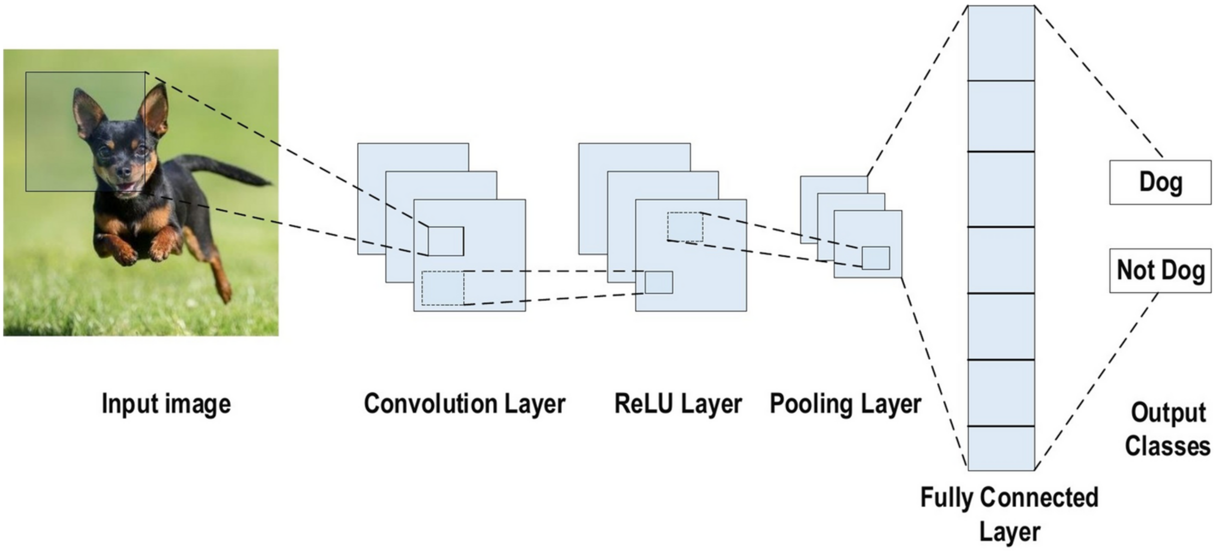

Figure 20: CNN network structure for image classification [ALZ21].

2.4.3 Decision tree algorithm

Derived from machine learning theory, decision trees are an effective tool for solving classification and regression problems [XU05]. A decision tree is a successive splitting method that sequentially partitions samples into subsets. Beginning with the entire dataset, the decision tree first identifies an attribute and a breakpoint before splitting the samples into subsets to improve the homogeneity of the class label vector within the subsets [YAN15].

In comparison to other machine learning algorithms like neural networks, decision tree algorithms are interpretable and provide valuable insights into the functioning of the underlying system [YAN15]. Decision trees can be utilized for classifying discrete output variables or predicting continuous output variables in regression. As supervised learning models, decision trees require a training dataset, consisting of input variables as well as known output labels. Once trained, decision trees can be used to generate predictions for input data with unknown output values [ABS21]. Figure 21 illustrates the structure of the decision tree algorithm, which comprises three node types: root, decision, and leaf nodes. The root node serves as the starting point, while the decision nodes facilitate decision-making by transitioning from one node to another. The leaf nodes serve as outputs from decision nodes. The tree is comprised of multiple sub-trees, with each sub-tree consisting of decision and leaf nodes [HAF21].

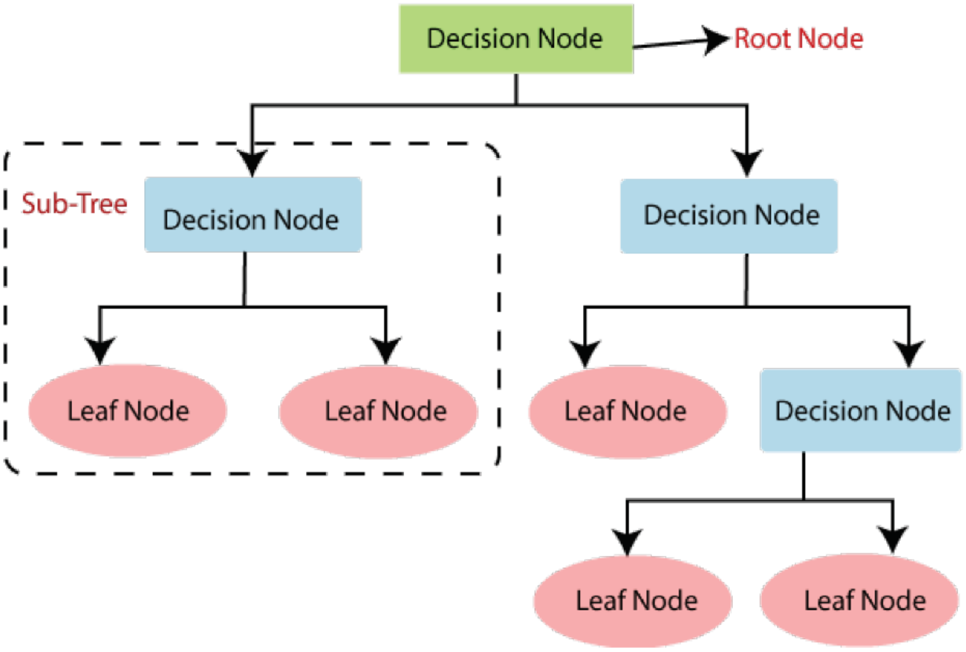

Figure 21: Structure of a decision tree algorithm [HAF21].

2.4.4 Data augmentation in regression models

As with all deep learning algorithms, the performance of the CNN algorithm is determined by the amount of labeled training data [DUB19]. However, in various processes, the collection of images can be a costly and difficult undertaking. To overcome this problem, image augmentation has proved to be an effective method to improve the generalization capabilities of neural networks. Beyond basic augmentations like image rotation, translation, and flipping, generative adversarial networks (GANs) can be utilized for producing artificial – but convincingly realistic looking – *fake* images to augment limited training datasets [COR21]. Dubost et al. introduce a data augmentation strategy called *Hydranet* in which a significant increase in the size of training datasets is achieved by recombining existing training samples [DUB19]. Figure 22 illustrates this strategy.

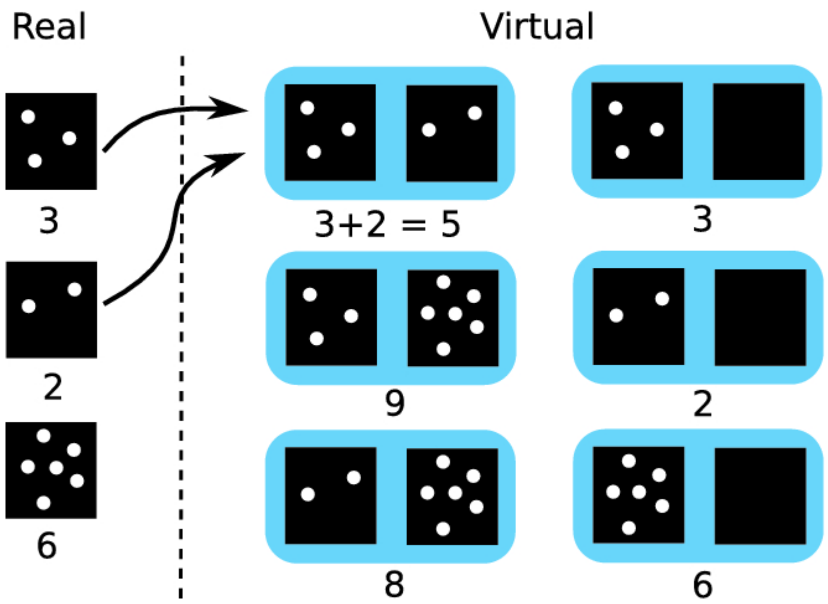

Figure 22: Create virtual training images by recombining real training images. The real samples are shown on the left, and the new virtual samples are shown on the right, along with the original samples resized to fit the new image dimensions [DUB19].

As can be seen in Figure 22, by combining the first and second images, a new virtual image was created from the sum of both images' labels.

2.5 Summary

Integrating sensors into mechanical structures, such as machine elements, offers several advantages, such as enhanced sensor accessibility to otherwise inaccessible processing points, protection of sensitive sensor elements, and enhanced signal quality, without compromising mechanical functionality or requiring changes to the interfaces of the overall system. While numerous methods have been examined in integrating sensors, it is evident that integration ready-to-use electromechanical sensors in a form-fit and force-fit manner, for example, through rotary swaging, significantly facilitates the joining process and ultimately allows the sensory properties of the manufactured structures to be adjusted. Despite progress in sensor integration techniques, much attention has been devoted to combining established measuring methods, primarily electromechanical transducers, with the mechanical host structures. This often results in trade-offs between the requirements of the mechanical structure and the desired sensory properties.

Current approaches to creating multiaxial sensor bolts demonstrate this conflict of interest. While externally applying strain gauge sensors does not compromise mechanical bolt strength, it necessitates encasing sensitive sensor films, altering external bolt geometry. Conversely, integrating strain gauge-based sensors within the bolt does not alter its outer dimensions but significantly reduces strength, especially when measuring bending forces in thick-walled structures.

To illustrate the effect of hole diameter on structural stiffness, assume that an internal hole is drilled in a round machine element to insert a strain gauge-based sensor. The resolution of the bending force measuring will increase as the diameter of the hole increases. However, this will result in a decrease in both bending and tensile stiffness depending on the diameter of the hole. A one-side clamped round bar with an outer diameter of 50 mm and a length of 100 mm is used to illustrate this effect. In this case, applying a bending force of 100 N would result in a measurable strain of more than 1 µm/m only at an inner hole diameter of 15 mm. Figure 23 depicts the resulting increase in the bending strain and decrease in the tensile and bending stiffness.

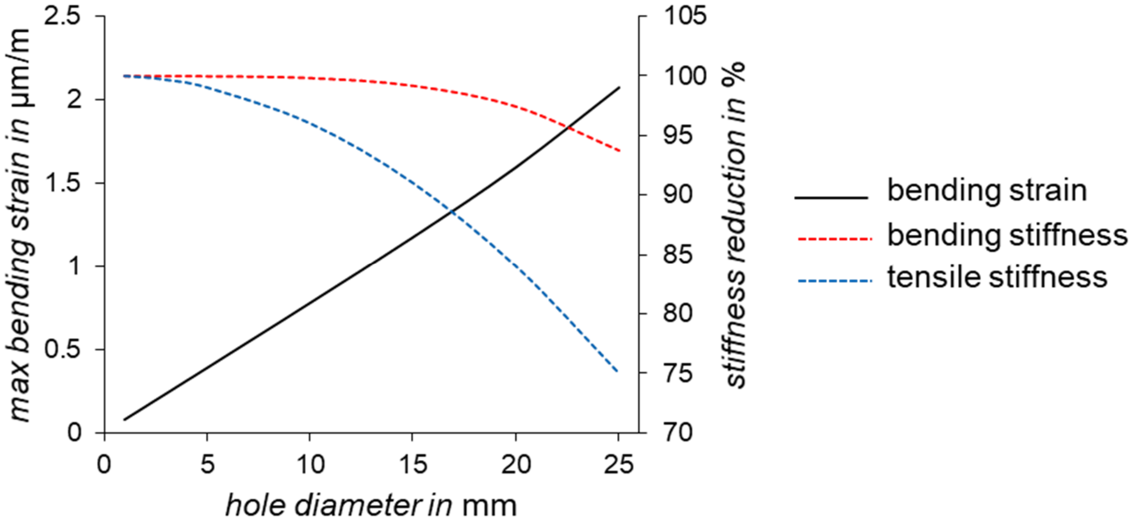

Figure 23: Visualization of the influence of the inner hole diameter on the structure stiffness.

Regarding sensor integration by rotary swaging, increasing the number of measurement axes leads to increased complexity in the sensor design, as Krech demonstrated in his dissertation [KRE20]. Furthermore, the cost and space requirements for the entire measurement chain increase linearly with the number of measurement axes.

A review of the state of the art demonstrates that there is a growing interest in optical-based force/torque sensors that rely primarily on intensity changes. However, while these sensors offer design flexibility and cost-effectiveness, multiaxial sensors of this kind suffer from limited measuring resolution. In contrast, image-based measurement technologies, such as Digital Image Correlation (DIC), offer the required resolution at a lower cost and with a simpler setup. Developments in the semiconductor industry, particularly in the field of image sensors, indicate a shift towards higher performance devices at lower costs. Likewise, the growing utilization of camera-based feature detection in industrial applications and advances in image processing algorithms, such as Convolutional Neural Networks (CNN), are improving the accuracy of object detection in captured images. Furthermore, augmented data can boost model accuracy even further.

3 Motivation and Objective

3.1 Motivation

In the age of digitalization and Industry 4.0, special attention is paid to the generation of data in the production environment and in mechanical structures in general. Sensor-integrated machine elements have proven to provide measurement capabilities to the point of interest in the manufacturing process or to accurately represent the load conditions in their structures.

An analysis of the state-of-the-art reveals that there is a considerable need for multiaxial force/torque sensors with low cost and space requirements that can be integrated within a host structure. These requirements cannot be met with current well-known electromechanical force/torque transducers due to their complex sensor design, associated effort for the joining process, and the competing requirements of both high measuring resolution and high mechanical strength.

Optical based multiaxial sensor concepts have been introduced as alternatives to conventional electromechanical sensors and have attracted special interest due to their low cost and design simplicity. However, their low achievable measuring resolution poses a challenge for their adaptation to machine elements and load bearing structures. In load bearing structures and machine elements, the resulting deformations are usually very small compared to the presented applications. Obtaining a comparable measurement resolution from strain gauge sensors would consequently require the deployment of highly complex optical measuring techniques, like interferometry or confocal measuring method. Conversely, optical measuring techniques for full field strain analysis, such as digital image correlation, provide high measurement resolution at (usually) high illumination and a large, complex, external setup.

3.2 Objective

In order to enable the widespread use of sensor machine elements and load-bearing structures, this thesis aims to contribute to the manufacture of such structures at low cost and with increased sensory performance with respect to the measuring axis and the measuring resolution. In pursuit of this objective, a proposed optical and image-based measurement concept facilitates multi-axial load measurement. It is designed to be embedded into machine elements with comparatively low space requirements. In addition, the possible integration of sensitive optical and non-contact sensor components into metallic structures will be investigated. The research aim can be divided into the following scientific sub-questions:

1. How can an optical non-contact measurement concept be designed to measure multiaxial loads within load-bearing structures and machine elements, while offering comparable measuring resolution to strain gauge-based sensors, and with a simple system design compared to high-resolution optical techniques such as interferometry?
2. What are the resulting design parameters, and can the sensor properties be configurated?
3. What are the requirements for integrating optical non-contact sensors into mechanical structures, and how can a process design for joining by rotary swaging meet these requirements?

3.3 Procedure

To answer these sub-questions, Chapter 4 presents an optical image-based measuring concept for multiaxial and high-resolution measurement of the resulting structural deformation under load. An analytical description of the sensor behavior under multiaxial loads is provided, outlining the correlations between the various load components and the resulting displacements between two measuring planes within the structure. Furthermore, design parameters for establishing the desired measurement resolution and a comprehensive strategy for sensor configuration are presented and an overview of the possible approaches to processing captured images and determining the occurring structural displacements is provided. Chapter 5 provides extensive validation of the findings from chapter 4 on various prototypes. Firstly, the capability of multiaxial load detection from single image acquisition is demonstrated. After that, different AI-based strategies for characterizing the sensor system's behavior are investigated and compared. In chapter 6, the sensor validation is performed in two stiff machine elements, as examples of possible industrial applications, by integrating the sensors into the bending roll of a roll forming machine and into the guidance column of a blanking tool.

In chapter 7, the sensor's integration into tubular structures by rotary swaging is discussed. A novel process design for the damage-free integration of optical elements with high positioning accuracy is presented, and the experimental results that have been obtained are discussed. Chapter 8 concludes with a summary and a discussion of future works.

4 Image-Based Multiaxial Measuring of Structural Deformations

4.1 Sensor Design

Taking image-based measurements to measure the load-induced elastic deformation of a metallic structure can be achieved by measuring the resulting displacement between two planes within the structure at a specific measuring distance l_m to each other. This can be achieved by placing an object in one plane and an image sensor in the other plane. During the elastic structure deformation under load, relative displacements between these two planes occur according to the load direction and can be captured by the built-in image sensor. Subsequent processing of the image determines the magnitude and direction of load-induced displacements in the captured images. Figure 24 shows the basic principle of optical image-based detection of plane displacement within a host structure.

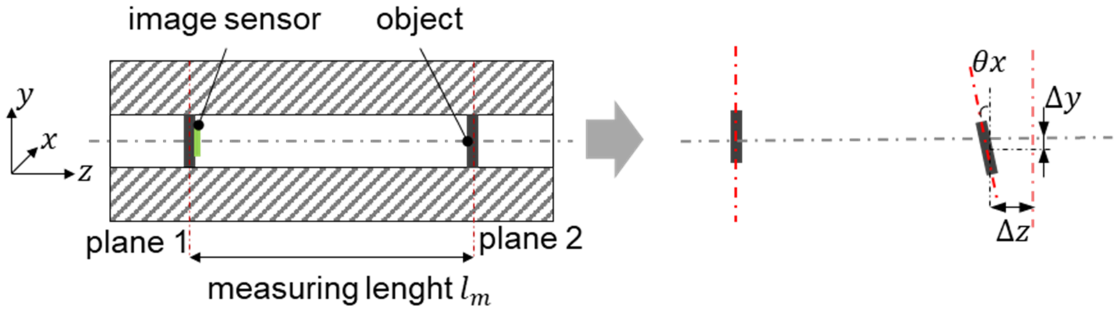

Figure 24: Schematic of optical image-based multiaxial load detection within a hollow structure (left) and visualized plane displacements in ($\Delta z, \Delta y$, and θx).

As shown in Figure 24, it is possible to measure the relative displacements between two measurement planes caused by the applied load component in the different axes of motion. The relationship between the applied load components and the resulting displacements can be expressed as follows:

$$\begin{pmatrix} F_x \\ F_y \\ F_z \\ M_x \\ M_y \\ M_z \end{pmatrix} = \vec{k}^T \begin{pmatrix} \Delta x \\ \Delta y \\ \Delta z \\ \theta x \\ \theta y \\ \theta z \end{pmatrix} \tag{1}$$

where k represents the calibrating coefficients. It is assumed in a simplified manner that a linear relationship exists between bending moments and bending forces. Thus equation (1) becomes

$$\begin{pmatrix} F_x \\ F_y \\ F_z \\ M_x \\ M_y \\ M_z \end{pmatrix} = \vec{k}^T \begin{pmatrix} \Delta x \\ \Delta y \\ \Delta z \\ l_m \cdot \Delta x \\ l_m \cdot \Delta y \\ \theta z \end{pmatrix} \tag{2}$$

where l_m is the axial distance between the two measuring planes.

Object pattern design

The dimensions and contrast of the features within the captured images have a significant impact on the ability to obtain higher resolution measurements of displacements based on Digital Image Correlation (DIC). When the feature generation of three state-of-the-art methods – airbrush, spin coating, and photomask – are compared, it is clear that the photomask variants offer a distinct advantage. See Figure 25.

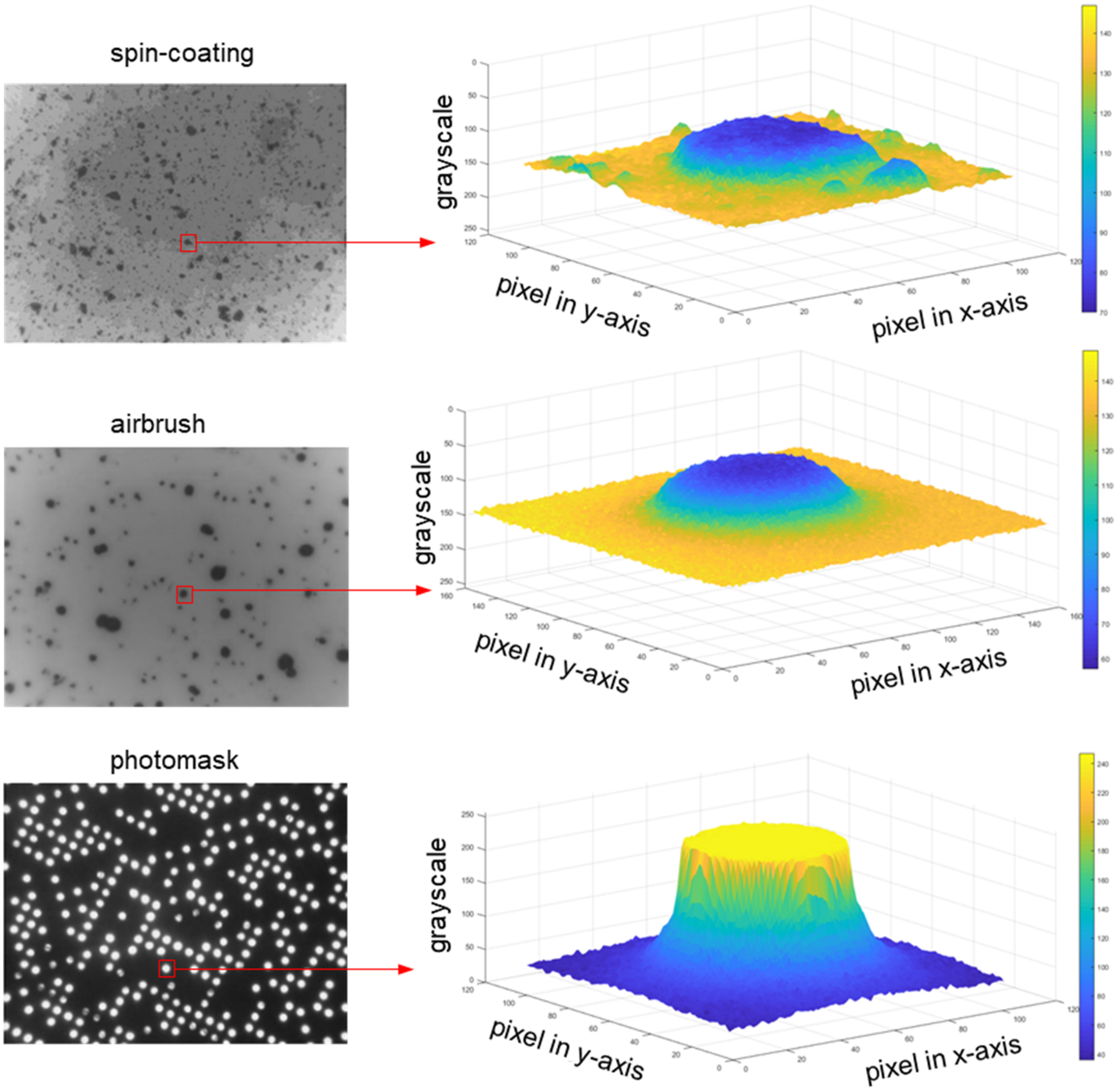

Figure 25: Comparison of the feature contrast achieved by the methods of spin coating, airbrush, and back-illuminated photomask patterning [S3].

In Figure 25 (left), sections of patterned areas created by spin-coating, airbrushing, and a back-illuminated photomask are displayed. In Figure 25 (right), grayscale representations of specific regions are visualized with a size of approximately 60 x 60 µm for each pattern. The patterns created by airbrushing and spin coating exhibit random feature distributions that can only be imprecisely influenced. Ultimately, these methods yield random patterns that are particularly suitable for full-field investigations. Lithography, on the other hand, allows the creation of several patterns on a photomask with specific geometry and spacing. Due to these advantages, the photomask is used to create specifically sketched and high-contrast patterns.

In-plane and out-of-plane displacements

The load induced relative displacements between the measuring planes can be divided into *in-plane* and *out-of-plane* displacements. In-plane displacements $\Delta x, \Delta y,$ and θz (see Figure 24) are caused by bending or torsional loads and can be easily detected by aligning the image sensor and the object in parallel. However, to detect out-of-plane displacement component Δz, caused by axial load, an extended optical system is necessary. As shown in [O3], employing a specialized configuration involving two mirrors, similar to a periscope design, enables out-of-plane displacements to be converted into in-plane displacements. As a result, the placement of two mirrors at an angle of 45 degrees to each other will change the lateral position of the reflected image in response to changes in the distance between the two measurement planes under an axial load.

Figure 26 illustrates the overall design of such an optical image-based sensor utilizing a back-illuminated photomask and two mirrors.

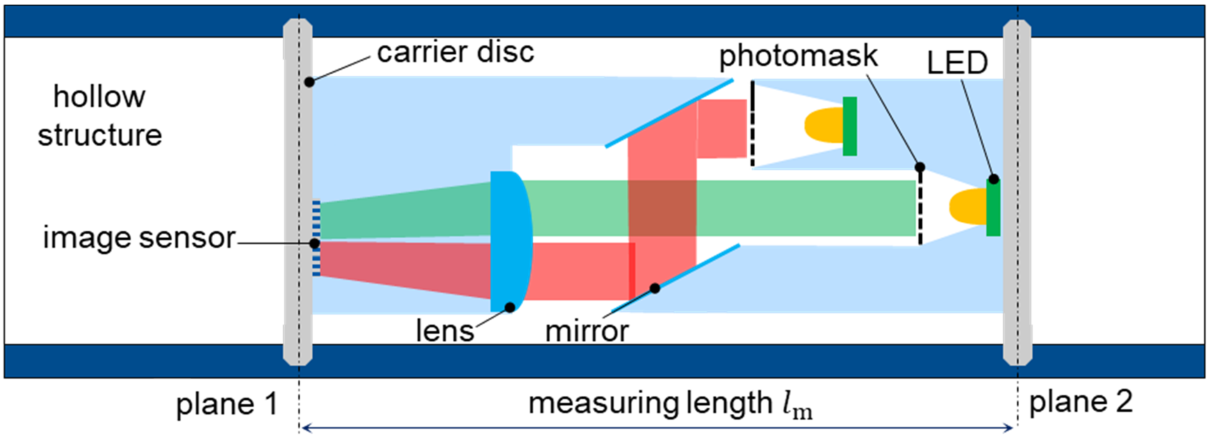

Figure 26: Schematic illustration of the optical image-based multiaxial structure-integrated load measurement [O3].

As can be seen in Figure 26, two carrier discs are inserted and fixed inside the hollow structure at a specific distance to each other, standing for the measurement planes. On the right disc, two stage back-illuminated photomasks are attached, projecting their pattern in two light beams. While the first beam directly enters the lens of the built-in image sensor, the second beam is reflected twice by the built-in mirrors. The area of the image sensor is thus divided into two parts. One part captures the pattern in the direct beam with the information about in-plane displacements, and the second part captures the mirrored beam with information about out-of-plane displacements. To ensure the same focus for both image parts, the photomask of the mirrored pattern is placed closer to the image sensor, compensating for the extended path length of the reflection. To uniquely distinguish between the translational displacements $\Delta x, \Delta y$, and Δz and between the rotational displacement θz, the pattern on both photomasks needs to have at least two evaluation points. In the captured images, the displacements are calculated at four evaluation points P_{1-4} with a specific area and in a specific area of possible displacement. Figure 27 demonstrates the projection of two-point patterns onto the image sensor surface for each of the two photomasks.

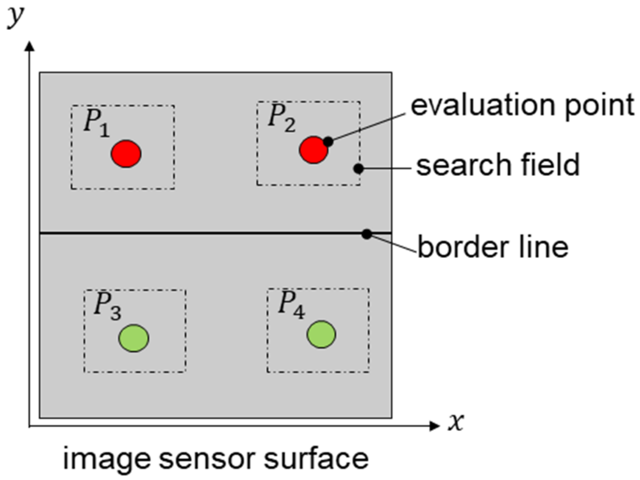

Figure 27: Visualization of the photomasks' pattern projection onto the image sensor where the pattern has only two points.

As shown in Figure 27, the evaluation points P_{1-4} can be considered as circular transparent areas within the non-transparent black foil. During image processing, the relative displacements between the two measuring planes will be determined by detecting the position change of evaluation points within an expected range of displacement (the search field). The intersection line of the two light beams is shown as a border line.

4.2 System Behavior Under Load

When the host structure is loaded with only bending forces F_{xy}, the amplitude and direction of the resulting deflection $\vec{\delta}_{\mathrm{xy}}$ can be determined by the displacements ΔP_1 and ΔP_2, which are equal in magnitude and direction. For a torsional load M_{t}, the angle of twist $\varphi{\sim}M_{\mathrm{t}}$ is calculated from the unequal displacement as the angle between the two vectors, connecting P_1 and P_2, before and after the displacement. The two vectors connecting the points P_1 and P_2 before and after the rotational displacements are calculated as follows:

$$\vec{v}_1 = \begin{pmatrix} P_{1\_x} - P_{2\_x} \\ P_{1\_y} - P_{2\_y} \end{pmatrix} \tag{3}$$

$$\vec{v}_2 = \begin{pmatrix} (P_{1\_x} + \Delta P_{1\_x}) - (P_{2\_x} + \Delta P_{2\_x}) \\ (P_{1\_y} + \Delta P_{1\_y}) - (P_{2\_y} + \Delta P_{2\_y}) \end{pmatrix}$$

where P_{i_x} and P_{i_y} are the x- and y-components of the initial positions of P_1 and P_2, and ΔP_{i_x} and ΔP_{i_y} are the x- and y-components of each displacement, respectively.

The angle of twist $\varphi{\sim}M_{\mathrm{t}}$ is then given by the dot and cross product of two vectors as follows:

$$\varphi = \arccos\left(\frac{\vec{v}_1 \cdot \vec{v}_2}{|\vec{v}_1| \times |\vec{v}_2|}\right) \tag{4}$$

With a known angle of twist φ and center of rotation coordinate $\vec{c}_{\mathrm{CR\_d}}$, the translational component of the displacement $\vec{\delta}_{xy}$ can be calculated in case of combined bending and torsional load (see Figure 29) using the following equation:

$$\vec{\delta}_{\mathrm{xy,i}} = \vec{c}_{\mathrm{i}} + \Delta\vec{P}_{\mathrm{i}} - \vec{c}_{\mathrm{CR\_d}} - \begin{pmatrix} cos(\varphi) & -sin(\varphi) \\ sin(\varphi) & cos(\varphi) \end{pmatrix} \left(\vec{c}_{\mathrm{i}} - \vec{c}_{\mathrm{CR\_d}}\right), \mathrm{i} = 1{,}2 \tag{5}$$

Where $\vec{c}_{\mathrm{i}}$ is the corresponding initial position and $\Delta\vec{P}_{\mathrm{i}}$ is the detected relative displacement of the evaluation point P_{i}. The deflections $\vec{\delta}_{xy,1}$ and $\vec{\delta}_{xy,2}$ are subsequently averaged to $\vec{\delta}_{xy}$ and then separated into δ_x and δ_y.

Alternatively, the translational displacement of the center of rotation can be calculated by applying the barycentric coordinates [SZC19]. For this purpose, three evaluation points are required to create a triangle enclosing the center of rotation. Furthermore, a mere compression or elongation of the structure due to an axial load F_z results in a change of the measuring span $l_m \mp \Delta l_m$, which is translated into the equally radial displacements ΔP_3 and ΔP_4. However, crosstalk occurs on the mirrored light beam both during bending and torsional loads. Figure 28 illustrates the system behavior under these loads.

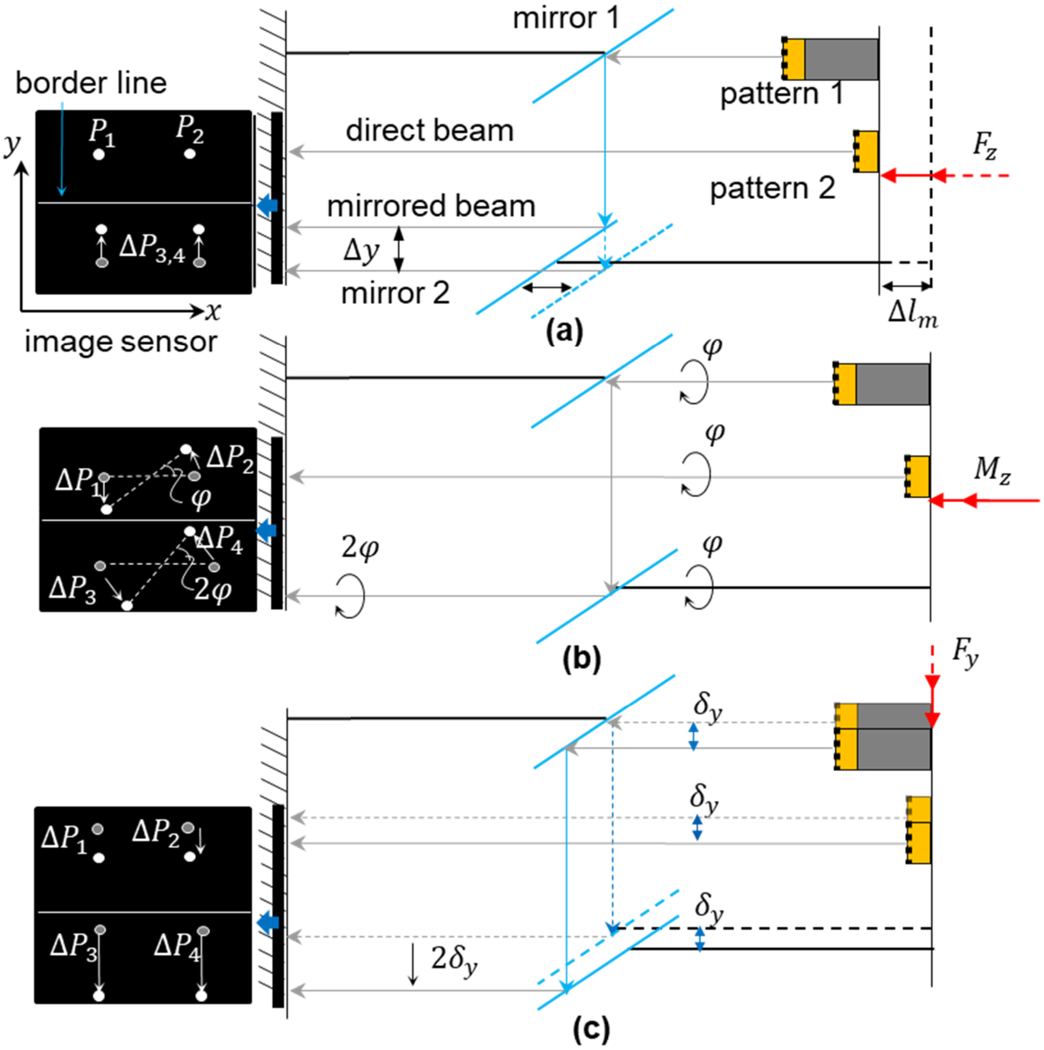

Figure 28: Visualization of the crosstalk behavior of in-plane displacements φ and $\vec{\delta}_{xy}$ on the out-of-plane displacements $\Delta P_{3,4}$ [O3].

While a mere compression or elongation of the structure due to an axial load F_z does not result in crosstalk on the evaluation points $P_{1,2}$ (Figure 28a), the angle of twist φ appears doubled in the mirrored image because of the rotation between pattern 1 and mirror 1 and between mirror 1 and mirror 2 (Figure 28b). These two displacement types (between pattern 1 and mirror 1 and between the two mirrors) cause, in the case of structure deflection under bending force F_{xy}, double displacements on the mirrored image segment ($\Delta P_{3,4} = 2\Delta P_{1,2}$) if the induced deflection is perpendicular to the border line (Figure 28c).

The illustrated displacement at the mirrored image segment $2\delta_{\mathrm{y}}$ caused by F_{y} in Figure 28c is considered an ideal scenario, as the border line, whose orientation on the image sensor's surface is defined by the rotation of the mirrors around the z-axis, is perfectly parallel to the system x-axis. However, this cannot be ensured due to the deviations expected during sensor assembly. For this reason, it will be further considered that the border line is rotated at an angle Ø to the x-axis of the image sensor. Figure 29 illustrates the influence of an inclined border line between the two beams on the determination of the crosstalk behavior.

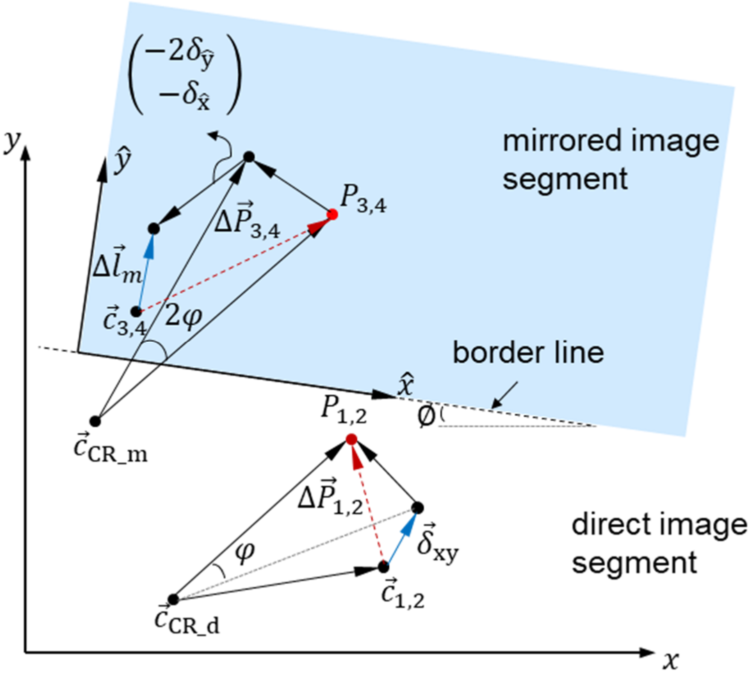

Figure 29: Influence of an inclined border line between the two beams on the determination of the crosstalk behavior [O3].

The displacement at the points $P_{1,2}$ in the direct image segment results from a translation component $\vec{\delta}_{xy}$ and a rotational component determined by the angle of twist φ. The translation component $\vec{\delta}_{xy}$ of the displacement can be easily determined in this case by applying equations (3)−(5). However, determining the displacement component $\Delta\vec{l}_m$ requires, besides known in-plane-displacements $\vec{\delta}_{xy}$ and φ, a known orientation of the border line or the angle by which it is twisted from the ideal parallel alignment to the x-coordinate of the image sensor (see Figure 29). Therefore, the border line coordinate system $\hat{x} - \hat{y}$ is used, which is rotated at an angle $\emptyset$ to the coordinate system $x - y$. The coordinate transformation matrix $R(\emptyset)$ is calculated as follows:

$$R(\emptyset) = \begin{pmatrix} \cos(\emptyset) & sin(\emptyset) \\ -\sin(\emptyset) & cos(\emptyset) \end{pmatrix} \tag{6}$$

After calculating both in-plane translational and rotatory displacements, the displacement of the structure caused by axial load $\Delta\overrightarrow{l_m}$ can be determined by known center of rotation of the mirrored image segment $\vec{c}_{\mathrm{CR\_m}}$ as a function of the angle $\emptyset$ as follows:

$$\Delta\overrightarrow{l_m} = R(\emptyset) \cdot \left(\vec{c}_{3,4} + \Delta\vec{P}_{3,4} - \vec{c}_{\mathrm{CR\_m}} - \begin{pmatrix} \cos(2\varphi) & -sin(2\varphi) \\ sin(2\varphi) & \cos(2\varphi) \end{pmatrix} \cdot \left(\vec{c}_{3,4} - \vec{c}_{\mathrm{CR\_m}} \right) \right) - \begin{pmatrix} 1 & 2 \end{pmatrix} \cdot R(\emptyset) \cdot \vec{\delta}_{xy} \tag{7}$$

where $\Delta\vec{P}_{3,4}$ is the displacement detected at the points P_3 and P_4, and $\vec{c}_{3,4}$ are their initial positions.

Here, the effect of crosstalk in the angle of twist φ is first eliminated from the displacement $\Delta\vec{P}_{3,4}$ by coordinate transformation with 2φ. Then a second coordinate transformation is performed on the border line coordinate system with the angle $\emptyset$ of the intermediate result together with the translational in-plane displacements $\vec{\delta}_{xy}$, doubling the $\hat{y}$-component.

The angle $\emptyset$ can be determined by means of a strictly uniaxial bending load (F_x or F_y), which leads to a one-dimensional displacement on the direct image segment ($\Delta P_1$and ΔP_2) and a two-dimensional displacement on the mirrored image segment ($\Delta P_{3,4}$). The angle $\emptyset$ can then be calculated as

$$\emptyset = \arctan\left(\frac{\Delta P_{3,4\_}y}{\Delta P_{3,4\_}x} \right) \tag{8}$$

After calculating the displacement components, the relationship between acting loads and plane displacements, generally defined in equation (1), is as follows:

$$\begin{pmatrix} F_x \\ F_y \\ F_z \\ M_x \\ M_y \\ M_z \end{pmatrix} = \vec{k}^T \begin{pmatrix} \delta_x \\ \delta_y \\ \Delta l_m \\ l_m \cdot \delta_x \\ l_m \cdot \delta_y \\ \varphi \end{pmatrix} \tag{9}$$

4.3 Measuring Resolution and Measuring Range

One of the main goals of the developed sensor concept is to achieve an acceptable measuring resolution, defined as the smallest measurable plane displacement resulting from the applied loads on the host structure. The four main parameters to increase the measuring resolution in an optical image-based sensor are:

1. *Measuring length* l_m: Higher measuring length allows for higher deflection δ_{xy} under bending load F_{xy}, a higher angle of twist φ under torsional load M_z, as well as a larger strain Δl_m between the two measuring planes under axial load F_z. The measuring resolution of all these displacements depends directly on the measuring length l_m.
2. *Optical magnification* M: Higher optical magnification M allows the size of a captured object to be enlarged and resolved onto a larger area of pixels on the image sensor, so that small displacements are magnified by the power M.
3. *Pixel size*: Smaller pixel size allows small pattern displacement to be captured. However, this is a product feature of the image sensor used.
4. *Degree of subpixel registration* s_p: Higher super-pixel registration when determining displacements using digital image correlation algorithms allows for the detection of subpixel displacements.

The influence of these parameters will be discussed in the following sections.

4.3.1 Measuring resolution

In order to assess the correlation between measurement length and measurement resolution, a reference is made to the well-established measurement resolution of strain gauge-based sensors, which is approximately 1 µm/m [KEI17]. This correlation will be demonstrated using a host structure where the load-induced local strains and resulting plane displacement are calculated.

The host structure is assumed to be a one-sided clamped hollow tube of length l, outer diameter D, and inner diameter d. It will be assumed that the occurring local strains are measured by strain gauge films within the structure at the diameter d. The occurring displacements are evaluated at two measuring planes placed at the two ends of the structure. See Figure 30.

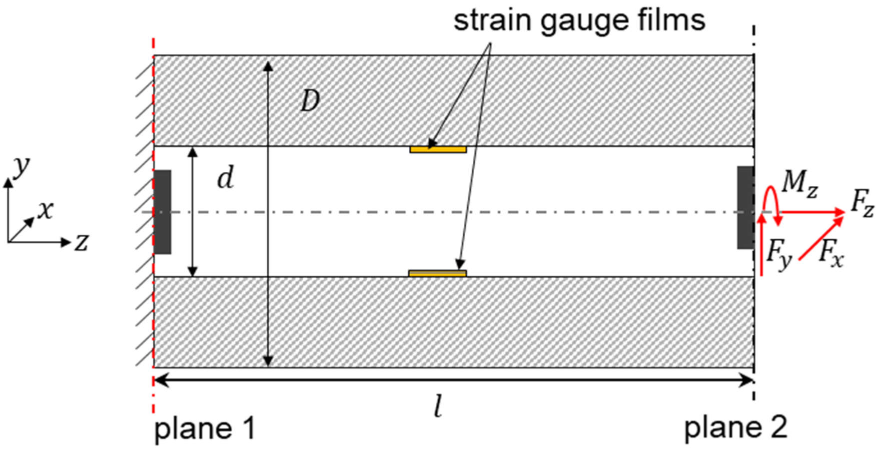

Figure 30: A one-sided clamped hollow tube for detection of local strains and relative plane displacements under different load components

Loading the tube with bending forces F_{xy}, axial force F_z, and torque M_z results in the bending strain ε_b, the normal strain ε_N, and the torsional shear strain ε_τ respectively.

With the normal strain components ε_N as a function of the resulting axial load F_z

$$\varepsilon_N = \frac{\sigma}{E} = \frac{F_z}{E\ A} \tag{10}$$

where σ is the normal stress under axial load F_z, E is the Young's modulus of the material, and A is the cross-sectional area of the hollow tube. The resulting length changing Δl under this axial load can be given as a function of the normal strain as follows:

$$\Delta l = \frac{F_z l}{E\ A} \tag{11}$$

In the case of bending load F_{xy}, the maximum bending strain at the clamping on the outer surface is given as

$$\varepsilon_b = \frac{\sigma_b}{E} = \frac{F_{xy} \cdot l}{W_b \cdot E} \tag{12}$$

with $\varepsilon_{b,d}$ as the resulting bending strain at the inner diameter d as follows:

$$\varepsilon_{b,d} = \varepsilon_b \frac{d}{D} = \frac{F_{xy} \cdot l}{W_b \cdot E} \frac{d}{D} \tag{13}$$

And the bending section modulus

$$W_b = \frac{\pi(D^4 - d^4)}{32D} \tag{14}$$

The resulting deflection of the tube at the free end under this bending load is given as

$$\delta_{xy} = \frac{F_{xy} l^3}{3EI_{xy}} \tag{15}$$

The product moment of area I_{xy} is given as

$$I_{xy} = \frac{\pi(D^4 - d^4)}{64} \tag{16}$$

When measuring torsional strain with strain gauge sensors that are usually rotated 45°, the measured strain $\varepsilon_{\tau,d}$ is equal to half the shear [MES23]:

$$\varepsilon_{\tau,d} = \frac{\gamma}{2} \cdot \frac{d}{D} = \frac{M_z}{W_p \cdot G} \cdot \frac{d}{D} \tag{17}$$

where G is the shear modulus and W_p is the torsional section modulus as follows:

$$W_p = \frac{\pi(D^4 - d^4)}{16D} \tag{18}$$

The resulting arc length arc of the angle of twist φ at the inner diameter d is given as

$$arc = \varphi \cdot \frac{d}{2} = \frac{M_z \cdot l}{G \cdot I_t} \cdot \frac{d}{2} \tag{19}$$

where the torsion constant for the section I_t is

$$I_t = \frac{\pi(D^4 - d^4)}{32}$$

Solving the equations to determine the resulting displacements between the two measuring planes as a function of the strain components yields the following:

$$\Delta l = l\varepsilon_N \tag{20}$$

$$\delta_{xy} = \frac{1}{3} \varepsilon_{b,d} l^2 \frac{W_b}{I_{xy}} = \frac{2}{3} \frac{l^2}{d} \varepsilon_{b,d} \tag{21}$$

$$arc = 2\ l\varepsilon_{\tau,d} \tag{22}$$

The equations (20), (21), and (22) show that, for normal and torsional strain, the resulting displacement increases linearly with the measuring length. In this case, the resulting deflection under the bending load increases quadratically to the measuring length and decreases linearly as the inner diameter of the tube increases.

Assuming an optical system with an optical magnification M and a subpixel registration s_p in the image-based displacement measurement, the measuring resolution s is determined as follows:

$$s = \frac{s_p}{M} \cdot pixel\ size \tag{23}$$

where s_p is the subpixel registration achieved by the coarse-fine algorithm and is defined as follows:

$$s_p = \frac{1}{2^n}, n = 1, 2, \ldots \tag{24}$$

where $s_p = 0.01$ pixels is the lowest achievable subpixel registration yet reported [YAN06].

Figure 31 demonstrates how the measuring resolution of an image-based deflection sensor can be increased by optical magnification and subpixel registration.

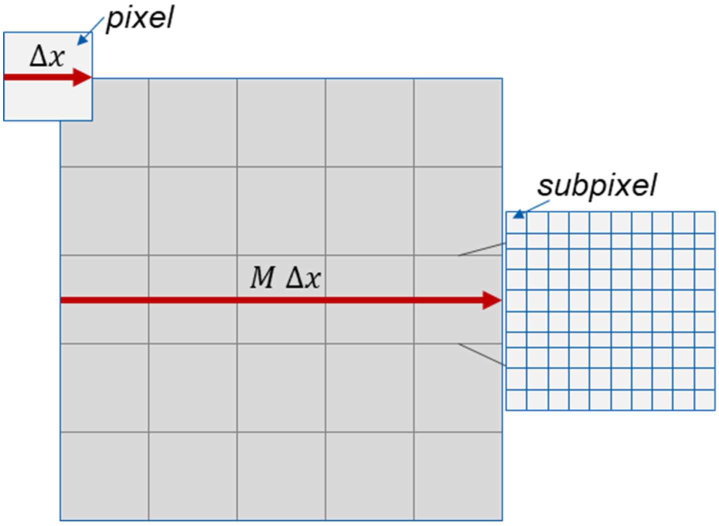

Figure 31: Visualization of the measuring resolution in image-based displacement measuring.

As can be seen in Figure 31, a displacement that is one pixel long will increase to be 5 pixels long by optical magnification. Subpixel registration, on the other side, plays a significant role in further increasing the desired measurement resolution, in addition to the influence of the measuring length.

Assuming a measuring resolution for the strain gauge sensors of $\varepsilon = 1\,\frac{\mathrm{\mu m}}{\mathrm{m}}$, a common pixel size of $1.3\ \mathrm{\mu m}$, a subpixel registration of $s_p = 0.125$ and an optical magnification of $M = 4$, the smallest detectable change using an image-based displacement sensor is $s = 0.040625\ \mathrm{\mu m}$.

Using these values for optical magnification and subpixel registration, the required measurement length of the image-based sensor system to match the measurement resolution of the reference strain gage sensor, $\varepsilon = 1\,\frac{\mathrm{\mu m}}{\mathrm{m}}$, can be determined. Next, the displacement components (Δl and arc) in equations (20) and (22) are assigned to $s = 0.040625$ µm and the equations are then solved to determine l.

$$l = \frac{\Delta l}{\varepsilon_N} \cong 40\ \mathrm{mm}$$

$$l = \frac{arc}{2 \cdot\ \varepsilon_{\tau,d}} \cong 20\ \mathrm{mm}$$

As shown above, the required measurement length for the image-based sensor to match the measurement resolution of a strain-gauge sensor is 40 mm for axial load and 20 mm for torsional load cases. The measuring resolution can be significantly increased through optical magnification, and the achievable subpixel registration can likewise be improved by the processing algorithm. However, higher optical magnification usually leads to changing the whole system, including the resulting measuring length. As can be seen in Figure 12, increasing the optical magnification from $M = 2$ to $M = 3$ requires increasing the distance between the lenses from 100 mm to 120 mm. Moreover, in basic lens systems like the three-lens zoom system, a higher optical gain results in higher aberration. This subsequently causes a decrease in feature contrast, which limits the attainable subpixel registration, as discussed in [ZHA19b] and [SCU21]. Figure 32 shows how the feature contrast decreases when the optical magnification is increased from $M = 1$ to $M = 3$ in three steps. Here, the pattern contrast is visually evaluated by the 3D grayscale curve. It can be seen, that optimal contrast and, consequently, pattern sharpness is most pronounced at an optical gain of $M = 1$. As optical magnification increases, contrast and feature sharpness diminish.

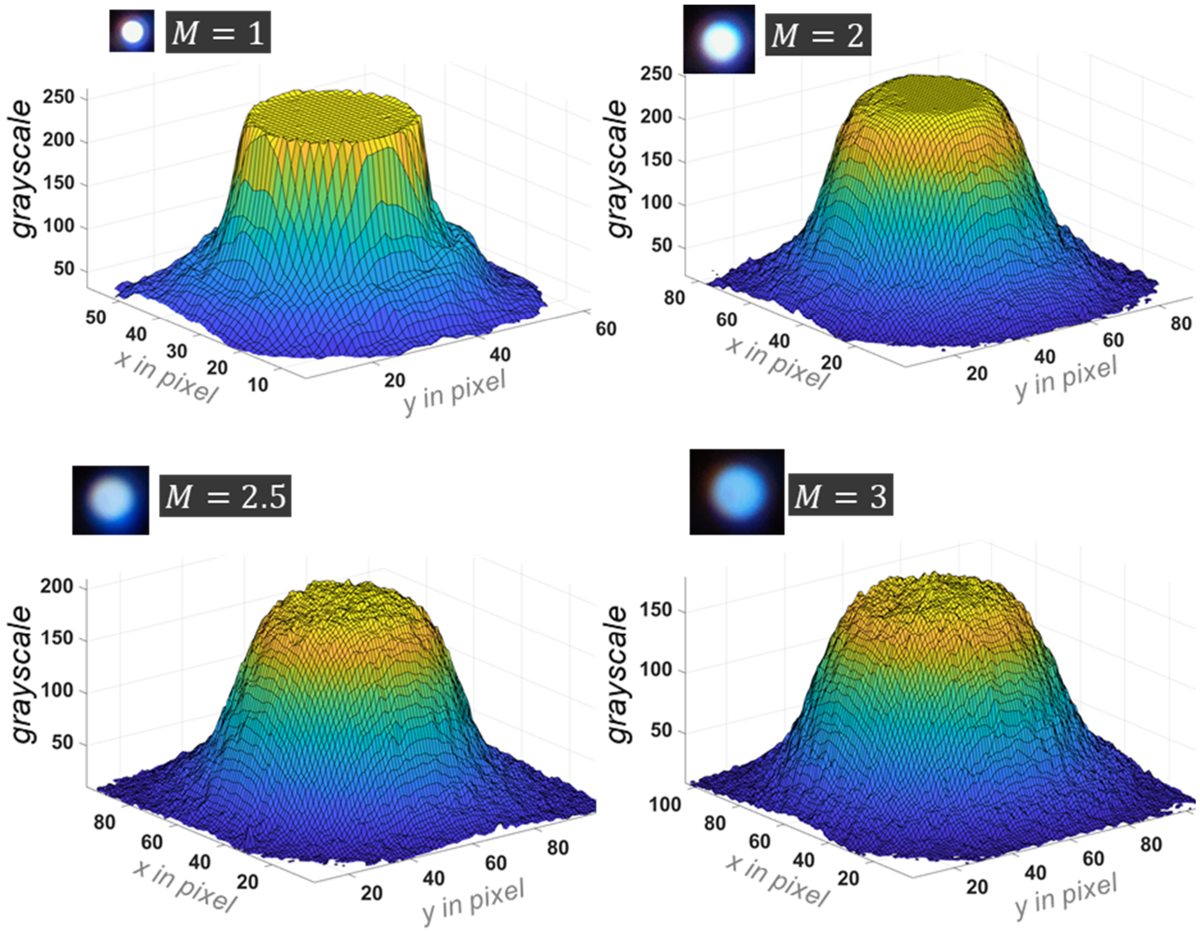

Figure 32: Deterioration of pattern imaging sharpness caused by increasing the optical magnification

4.3.2 Measuring range

In the image-based deflection sensor, the measuring range is determined by the maximum detectable displacements, which depend on several factors, including the measuring length l_m, optical magnification M, and the imaging area of the image sensor. Force/torque sensors often present a trade-off between achieving high measurement resolution and setting a larger measurement range. However, the high sensitivity of the axial force measurement to bending loads and measuring length is particular characteristic of the presented sensor design. As can be seen in equations (20), (21), and (22), the structural deflection δ_{xy} under a bending load increases quadratically with the measuring length, while torsion and axial load exhibit a linear increase. Due to bending crosstalk on a measured axial load, shown in Figure 28 and equation (7), a significant challenge arises from the potential for a bending load to cause the mirrored beam to shift outside of the sensor surface. Assuming a square shaped image sensor area A_s with a length and width of $\sqrt{A_s}$, an optical magnification M, and a photomask pattern located at the center of each point segment in the unloaded case, Figure 33 demonstrates the correlation between sensor area, optical magnification, maximum deflection under bending load $\delta_{xy,max}$, and maximum elongation under axial load $\Delta l_{m,max}$.

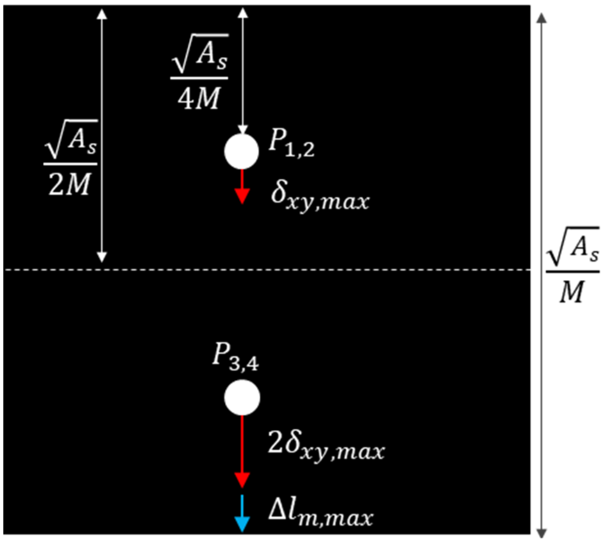

Figure 33: Displacement measuring range as a function of sensor area, optical gain, and maximum structure elongation and deflection under load.

As can be seen in Figure 33, the image sensor area A is reduced by the optical magnification to $\frac{\sqrt{A_s}}{M}$. Considering that the sensor area is divided into two equal parts (one for the direct beam and the other for the reflected beam), with the photomask pattern positioned in the center of each part, a $\frac{\sqrt{A_s}}{4M}$ displacement range is achieved in both directions. In addition, it can be seen that an in-plane displacement of $\delta_{xy,max}$ of the feature points $P_{1,2}$, perpendicular to the border line, results in a $2\delta_{xy,max}$ shift of the points $P_{3,4}$ in the reflected image segment, which significantly limits the axial force measurement range. For a given image sensor area A_s, the maximum achievable optical magnification is determined as follows:

$$M = \frac{\sqrt{A_s}}{8(\delta_{xy,max}+\Delta l_{m,max})} \tag{25}$$

4.4 Procedure for Sensor Configuration

Multiaxial measuring of the relative displacements of two measurement planes in a host structure by means of the presented sensor design, as shown in Figure 26, poses a challenge both in terms of the configuration of the sensory properties and the resulting requirement for positionally accurate alignment of the two sensor parts to each other.

Two primary challenges emerge when configuring the sensors:

1. Setting an appropriate measurement length: Increasing the measurement length allows for higher resolution of the displacement measurements but reduces the measurement range for axial force.

2. Setting an appropriate optical magnification: Optical magnification is a crucial design parameter for enhancing measurement resolution. However, it also results in reducing the measurement range and increasing imaging aberrations, thereby reducing the achievable degree of subpixel registration by decreasing feature sharpness. Furthermore, adjusting the optical magnification usually requires changing the system length, as shown in the three-lens zoom system in Figure 12.

The sensor design process must, therefore, iteratively adjust the measuring length and the optical magnification while simultaneously evaluating the resulting pattern sharpness. Figure 34 shows an iterative design procedure for the sensor system, simplified to focus on two key design parameters: measurement length and optical magnification.

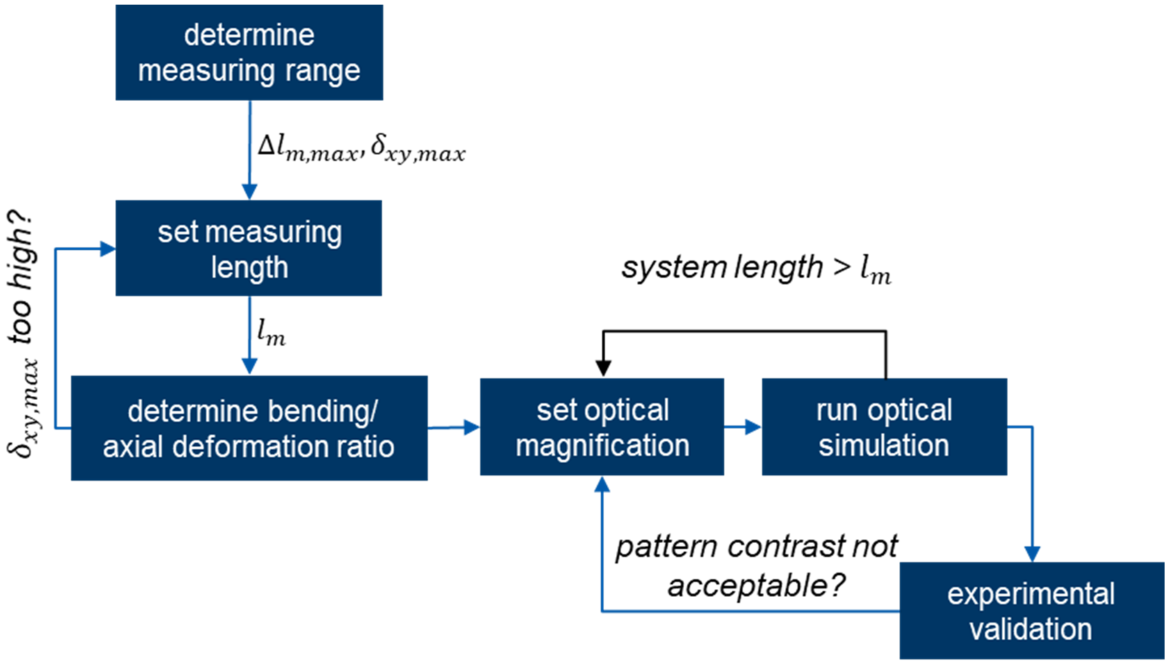

Figure 34: Iterative setting of the optical magnification and measuring length in the sensor design.

In the exemplary iterative design procedure presented in Figure 34, a specified measuring range based on the maximum displacements $\delta_{xy,max}$ and $\Delta l_{m,max}$ is initially assumed, and the measuring length is set. If the resulting deflection $\delta_{xy,max}$ is too high to achieve the desired measuring range for the axial force, the measuring length is reduced. The optical magnification is then given an initial setting, and optical simulation is performed to determine the required lenses and their arrangement. If the overall system exceeds the set measurement length, the optical magnification is decreased. Once the optimal system is established, the resulting pattern sharpness is evaluated as a measure of the achievable subpixel registration.

4.5 Image Processing

An important feature of the image-based sensor is image processing. There are three primary goals for the sensor's image processing:

1. Increasing the achievable measurement resolution by filtering out or compensating for optical aberrations

2. Accurately assigning the detected displacement to the applied load components

3. Reducing processing time and required computing power

The first requirement is driven by the previously discussed conflict of interest between increasing optical magnification and the resulting reduction in pattern sharpness. The second requirement focuses mainly on the case of multiaxial loads and the accuracy of an exact assignment of the detected displacements to the load components causing them. For this task, the analytical methods detailed in section 4.2 will be employed, and deviations in the system's behavior must be compensated by the processing algorithm. The third requirement stems from the fact that force/torque sensor technology produces a time-series signal and, consequently, does not present any real-time monitoring problems. However, an image-based measurement sensor must process a vast matrix of pixel data before converting them into time-series signals. Therefore, the emphasis is on the required processing time and computational power.

4.5.1 Image pre-processing

As shown in Figure 32, the desired increase in optical magnification leads to a significant decrease in pattern sharpness and thus a decrease in the achievable measuring resolution. However, since the captured images comprise three color channels, while only grayscale values are used to determine the resulting displacement, the color channel, which is less affected by chromatic aberration, shows a clear enhancement compared to converted to black and white images. Figure 35 shows the feature sharpness for the optical magnification $M = 2$ in Figure 32 evaluated visually by the 3D grayscale curve.

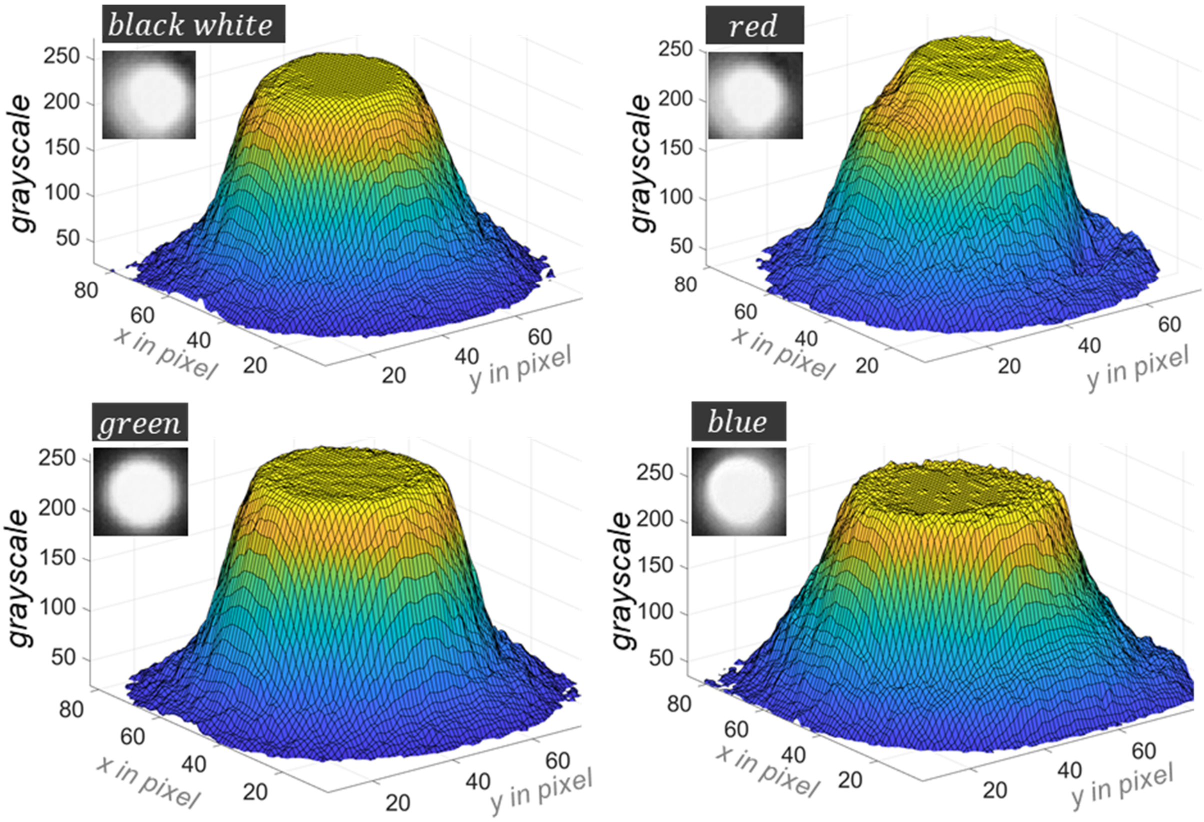

Figure 35: Resulting feature sharpness in the color channels.

As shown in Figure 35, the 3D grayscale curves show certain differences compared to the three color channels. Here, the green color channel shows the best feature sharpness while the red color channel shows a non-circular feature shape due to lateral chromatic aberration. When the RGB image is converted into a gray image, the color dependent aberration affects the image quality. For the exemplary case in Figure 35, the green image color will be rather used for determining the feature displacement.

4.5.2 Digital image correlation

As shown in subsection 2.4.1 digital image correlation can be achieved using various correlation algorithms. For high-resolution position detection of a non-deformable and non-rotating pattern on an image with nearly constant illumination, the main influencing parameters are defined as subset size, search field, and degree of subpixel registration (see Figure 36a). Investigations by Winter have shown that the Normalized Cross Correlation (NCC) and the Normalized Sum Square Difference (NSSD) with full pixel shift are particularly suitable with respect to the achievable accuracy and the required computation time. However, both algorithms depend highly on the subset size and the search field. Figure 36b shows the required computation time as a function of the subset size, and Figure 36c shows the case of a constant subset size of 40 pixels as a function of the search field size. Once the full pixel displacement has been determined, coarse-to-fine correlation algorithms have proven to be the most appropriate to improve the correlation results in the fine subpixel accuracy [S2]. However, the computational time of this algorithm depends largely on the subset size and the degree of subpixel registration. Figure 36d shows a logarithmic plot of the computation time as a function of the degree of subpixel registration for two subset sizes of 8 and 40 pixels.

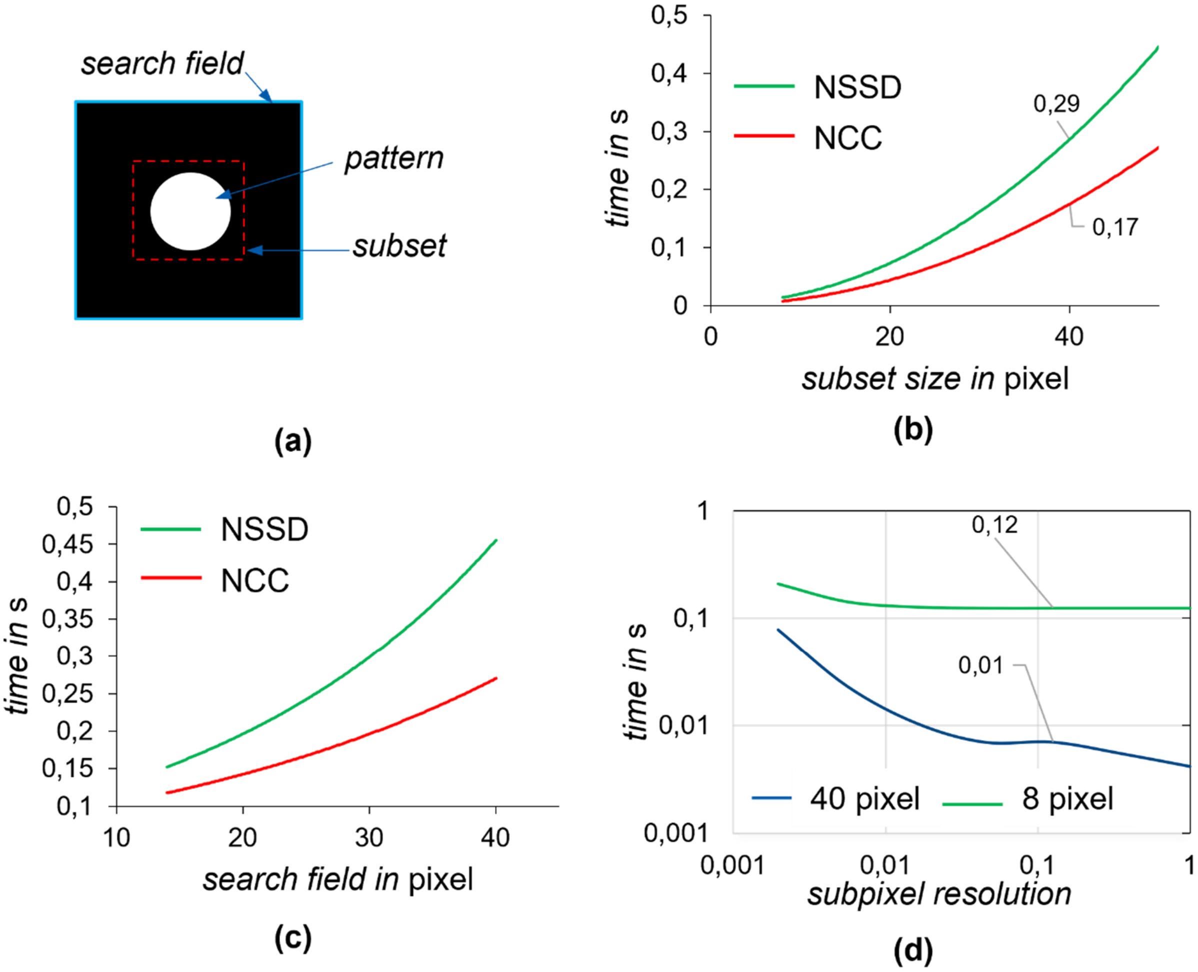

(a) (b)

(c) (d)

Figure 36: Key parameters for DIC and required processing time. (a) Visualization of the parameters and processing time for the two DIC algorithms NCC and NSSD; (b) as a function of the subset size; and (c) as a function of the search field size; (d) a

logarithmic curve of the processing time as a function of the subpixel size according to [S2].

As shown in Figure 36b and c, the increase in required processing time is almost square with increases in the subset size and exponentially with increases in the size of the search field. In both cases, the normalized sum-square-difference algorithm (NSSD) increases more significantly than the normalized cross-correlation (NCC). The logarithmic graph of the required processing time as a function of subpixel resolution in Figure 36d shows that the processing time increases significantly with the higher subpixel resolution and less so with the subset size.

For a search field of 70 pixels, the NCC algorithm requires a computation time of 0.7 seconds for a 40-pixel subset. If a subpixel registration of 0.1 pixels is adjusted, an additional computational time of 0.1 seconds will be required for the coarse-to-fine algorithm. The used notebook has a 2.4 GHz Intel Core 2 Duo processor and 4 GB 1067 MHz DDR3 RAM [S2].

4.5.3 CNN-based displacement computation

As can be seen above, the pixel-wise subset matching and comparison of the correlation values for each iteration allows the analytically operating algorithms of DIC to achieve high accuracy. Furthermore, the resolution of the displacement measurement can be significantly increased by subpixel registration. However, its main drawback is the computational time required. An approach to reduce the computational time for displacement calculations while maintaining the accuracy of DIC is to use convolutional neutral networks (CNN). In this approach, a CNN algorithm is trained on the displacements computed by the DIC and used to predict displacements in the same manner as the DIC. For the use case of multiaxial sensor load-bearing structures and machine elements, creating a large amount of training data is quite a challenge. In the term of investigation by Zhang et al. [S4], a CNN network is designed to be trained with only 72 images acquired under different load conditions with different degrees of displacement. The resulting displacements in the training data are evaluated using the DIC algorithm to a subpixel registration of 0.1 pixels. Since CNNs have good performance in classification tasks, the considered problem is reduced to a classification problem of numbers between 0 and 10.

To reduce the complexity of the model, the CNN is divided into three sub-models or displacement determination levels, each with 10 classes, based on the approach of Ma et al. [MA21]. The first level, F-CNN, determines the displacements in the tens scale. The second level, S-CNN, determines displacements in the single digits, and the third level, T-CNN, determines displacements in the decimal digits. The output of the three sub-models is then calculated to the determined displacement. See Figure 37.

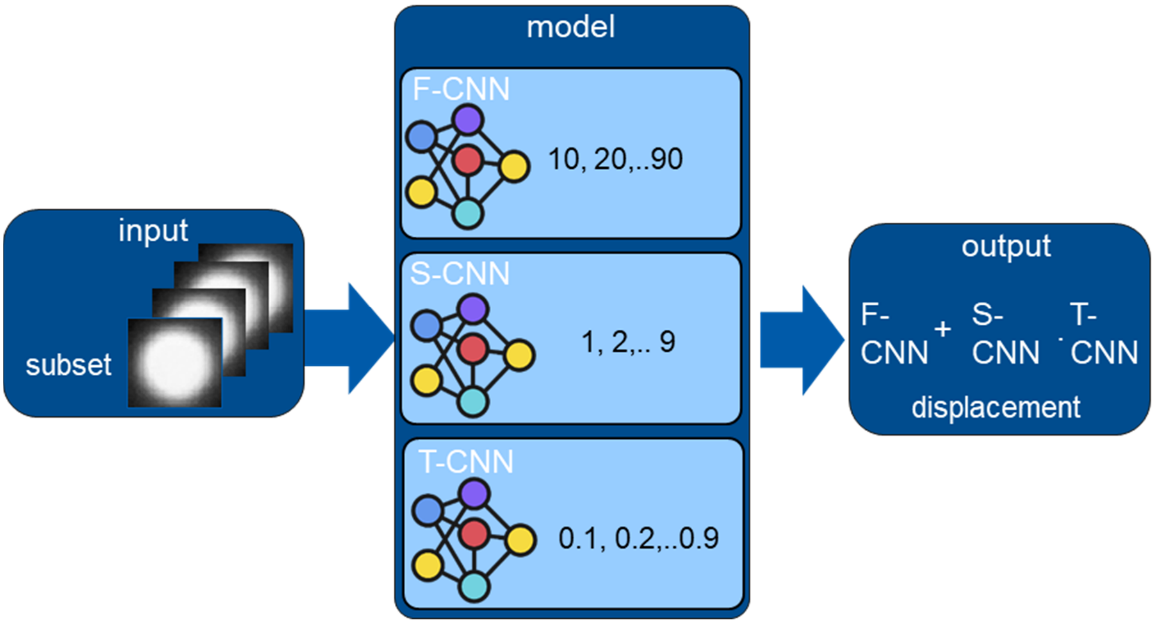

Figure 37: CNN network structure for determining displacements by number positions in the decimal number system according to [MA21] and [S4].

As can be seen in Figure 37, the input to the network is an image subset that contains the pattern and a search field for the possible displacement area. Furthermore, considering the relatively low amount of training data, the algorithm is designed to determine displacements in only one direction. This allows the creation of a network that provides high accuracy with a small amount of training data and with low model complexity. To determine displacements in all four directions, each image is rotated by 0°, 90°, 180°, and 270°, and the displacement is calculated each time and assigned to the axis depending on the angle of rotation. Figure 38 visualizes this procedure.

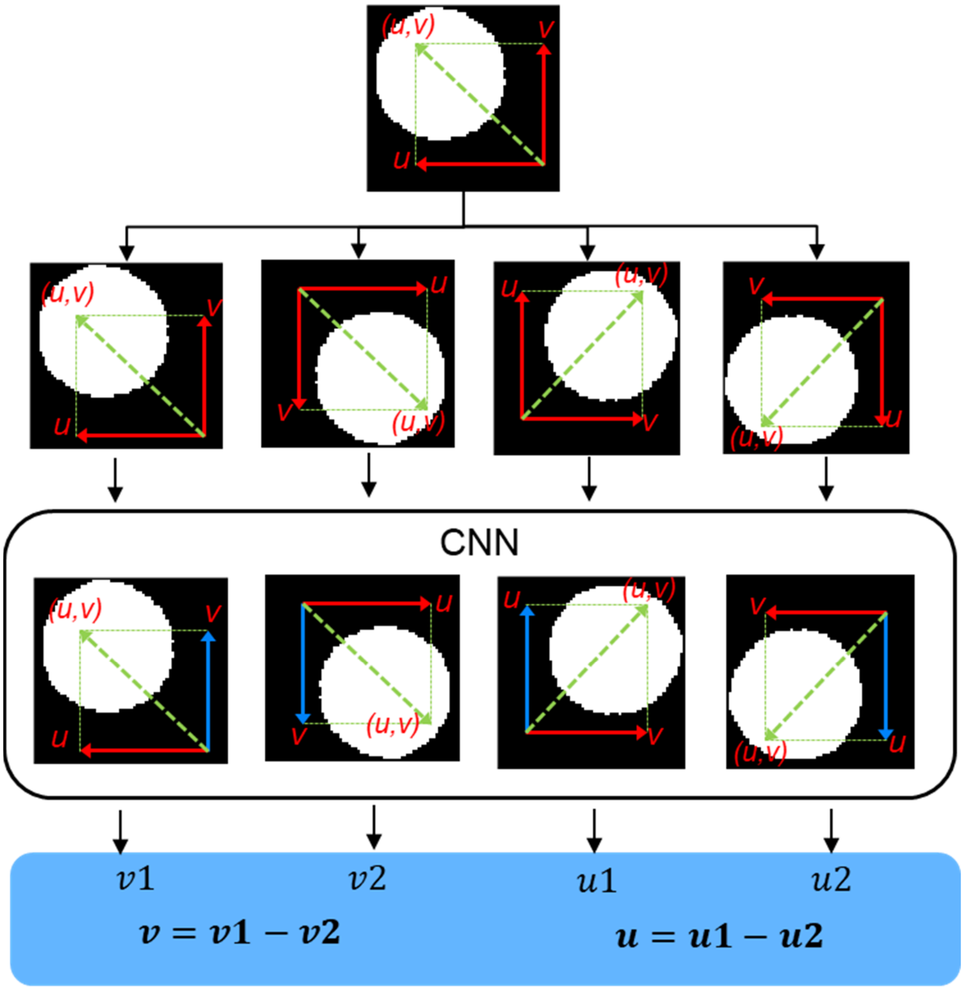

Figure 38: Displacement determination process according to [MA21].

Since the number of convolutional and fully connected layers determines the complexity of the network and, thus, the required training data and prediction time, the focus was on keeping these layers as small as possible while maintaining the required accuracy. The created CNN model consists of three basic units and three fully connected layers. Each basic unit consists of two convolutional layers, each with a 5x5 pixel kernel size. The first basic unit uses 16 kernels, the second uses 32 kernels, and the third uses 64 kernels [S4]. Figure 39 shows the achieved prediction accuracy of the three sub-models and the required prediction time cost as functions of the number of fully connected layers.

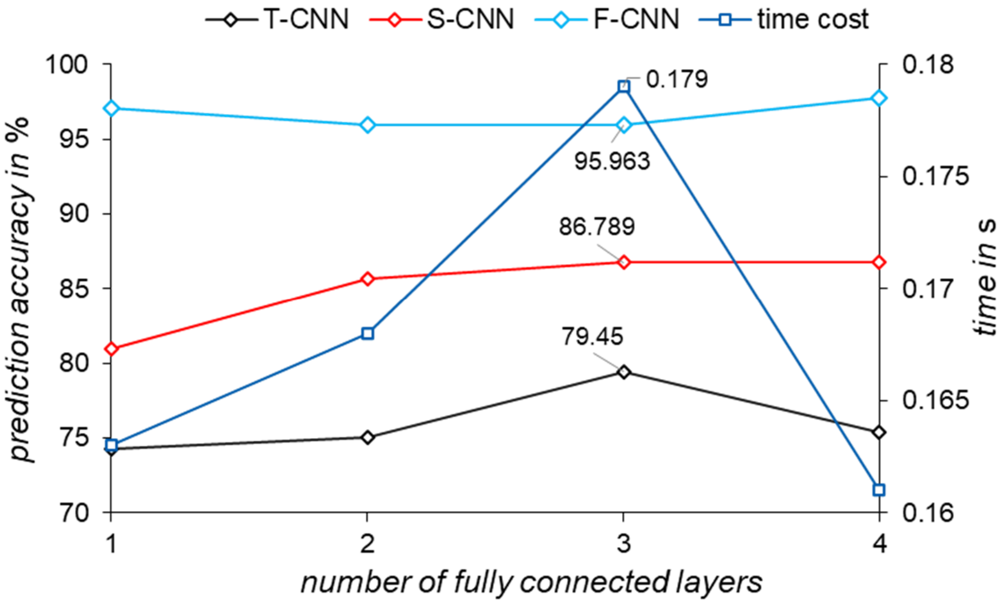

Figure 39: Prediction accuracy and time cost as functions of the number of fully connected layers according to [S4].

As shown in Figure 39, the sub-models have different degrees of prediction accuracy with respect to the number of layers. In the case of three fully connected layers, the F-CNN shows the best prediction accuracy of about 96%, followed by the S-CNN with 86.8% and the T-CNN with 79.45% accuracy.

A significant advantage in computational time can be observed compared to the DIC algorithm. The computational time of DIC algorithms is dependent on the subset size, which does not affect the CNN model. However, a subset size of 40 pixels and a search field of 70 pixels, along with a subpixel registration of 0.1 pixels, will require a computational time of 0.8 seconds for the DIC algorithm. In contrast, the CNN model only requires less than 0.2 seconds of computational time.

5 Validation of the Sensory Properties

After presenting the sensor, analytically deriving its behavior, and discussing the set parameters for the measurement resolution, as well as the algorithms for determining displacements from the acquired images, this chapter deals with the experimental validation of the sensory properties.

5.1 Multiaxial Load Determination

As a proof of concept for multiaxial load measuring, a sensor prototype is designed to measure the displacement caused by multiaxial loads applied to a hollow tube in between two parallel measuring planes.

5.1.1 Test setup and sensor assembly

The two parts of the sensor are bolted to two rigid flanges to ensure no deformation or relative displacement between the sensor parts and their carrying flanges. In a designed test bench, the host structure with the built-in sensor is mounted on a multiaxial strain gauge-based sensor from HBM (HBM: K-MCS10-025) on one side. On the other side, axial force, bending force, and torque are applied, causing elastic deformation of the host structure and, thus, relative motion between the two sensor planes, which is than captured by the built-in image sensor. The sensor components are combined using 3D-printed parts and inserted into tubes with external threads. These tubes are then screwed into the flanges, see Figure 40.

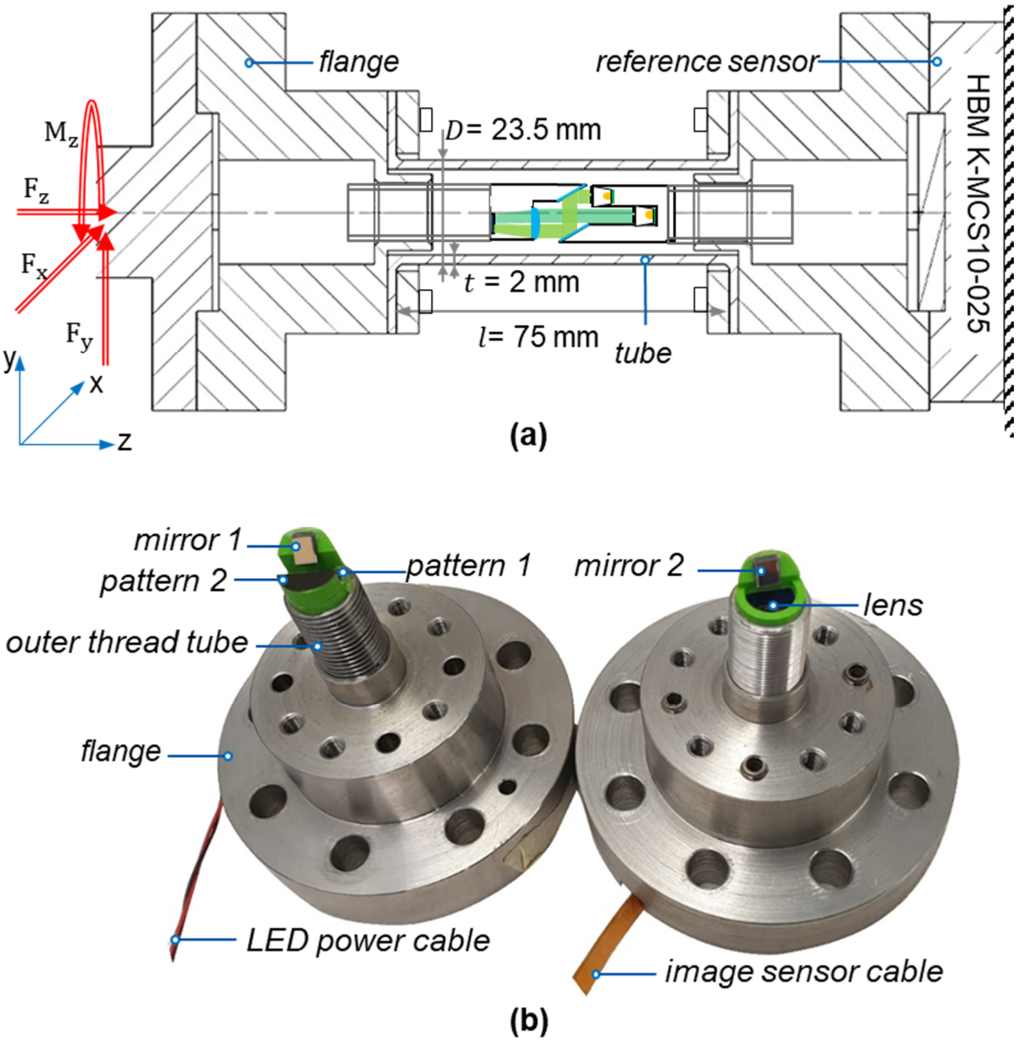

Figure 40: Evaluating the multiaxial load detection: (a) test bench design and (b) sensor prototype [O3].

To minimize optical aberrations and to sufficiently focus the pattern points P_{1-4} at the maximum expected strain or compression of the structure of $\Delta l = \mp 0.0258\ \mathrm{mm}$ at $F_z = \pm 10\ \mathrm{kN}$, a symmetric lens system is designed to provide an optical magnification of $M = -1$ and a best focus range of [-0.248 mm, 0.252 mm]. The photomask patterns are, therefore, imaged 1:1 on an image sensor (Omnivision OV5647) of 3673.6 µm x 2738.4 µm with a pixel size of 1.4 µm x 1.4 µm. Image acquisition is performed using a Raspberry Pi device. The photomask used is from JD PHOTO DATA and has a point diameter of 5 µm. Given that the feature has a diameter of only 5 µm ~ 7 pixels, a subset size of 10 pixels is established around the center of each pattern. Further, based on a maximum expected deflection of 0.16 mm under the maximum bending force $F_{xy} = 2kN$, the search field is set to be 100 pixels, as illustrated in Figure 41.

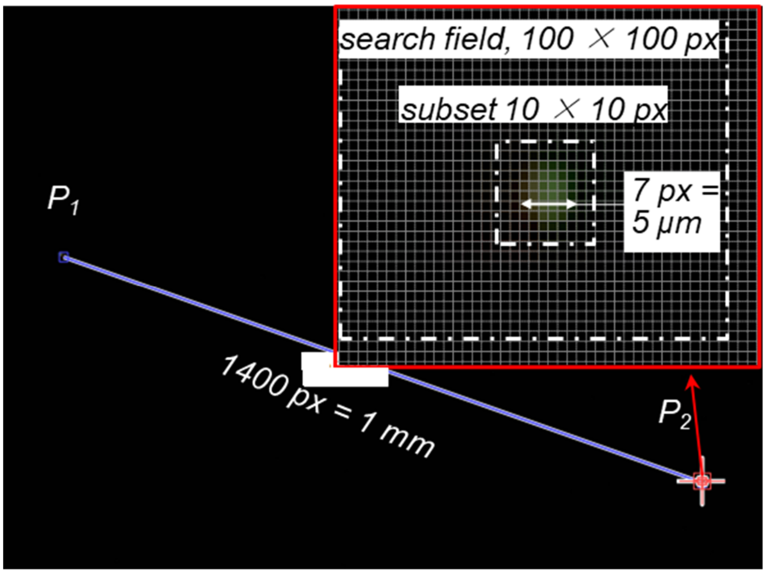

Figure 41: Photomask design [O3]

As presented in section 4.2, the initial step in characterizing the displacement involves the determination of the rotation centers for both the direct image segment $\vec{c}_{\mathrm{CR\_d}}$ and the mirrored image segment $\vec{c}_{\mathrm{CR\_m}}$. These centers of rotation are determined by calculating the intersection points of two linear functions, defined by the positions of each pattern before and after a rotation induced by torsional loading. Subsequently, the uniaxial loads (F_{x}, $F_{\mathrm{y}}, F_{\mathrm{z}}$, M_{z}) and then multiaxial loads ($F_{\mathrm{x}} + F_{\mathrm{y}} + F_{\mathrm{z}} + M_{\mathrm{z}}$) are manually applied within the defined loading limits of the structure F_{x} and F_{y} between ±250 N, M_{z} between ± 65 Nm, and F_{z} between ±3 kN. The loads are therefore incrementally increased and decreased. The measured displacement components (φ, δ_x, δ_y, and Δl_m) are calculated according to equations (3)−(5). In this case, no crosstalk behavior occurs, and the displacement on the mirrored image segment is simply determined. The displacement components are then compared with the analytically expected reference values, which are calculated from the tube geometry and the reference loads measured by the strain gauge sensor.

5.1.2 Results for uniaxial loading

Figure 42 presents the achieved results for uniaxial loads (F_x, F_y, F_z, M_z).

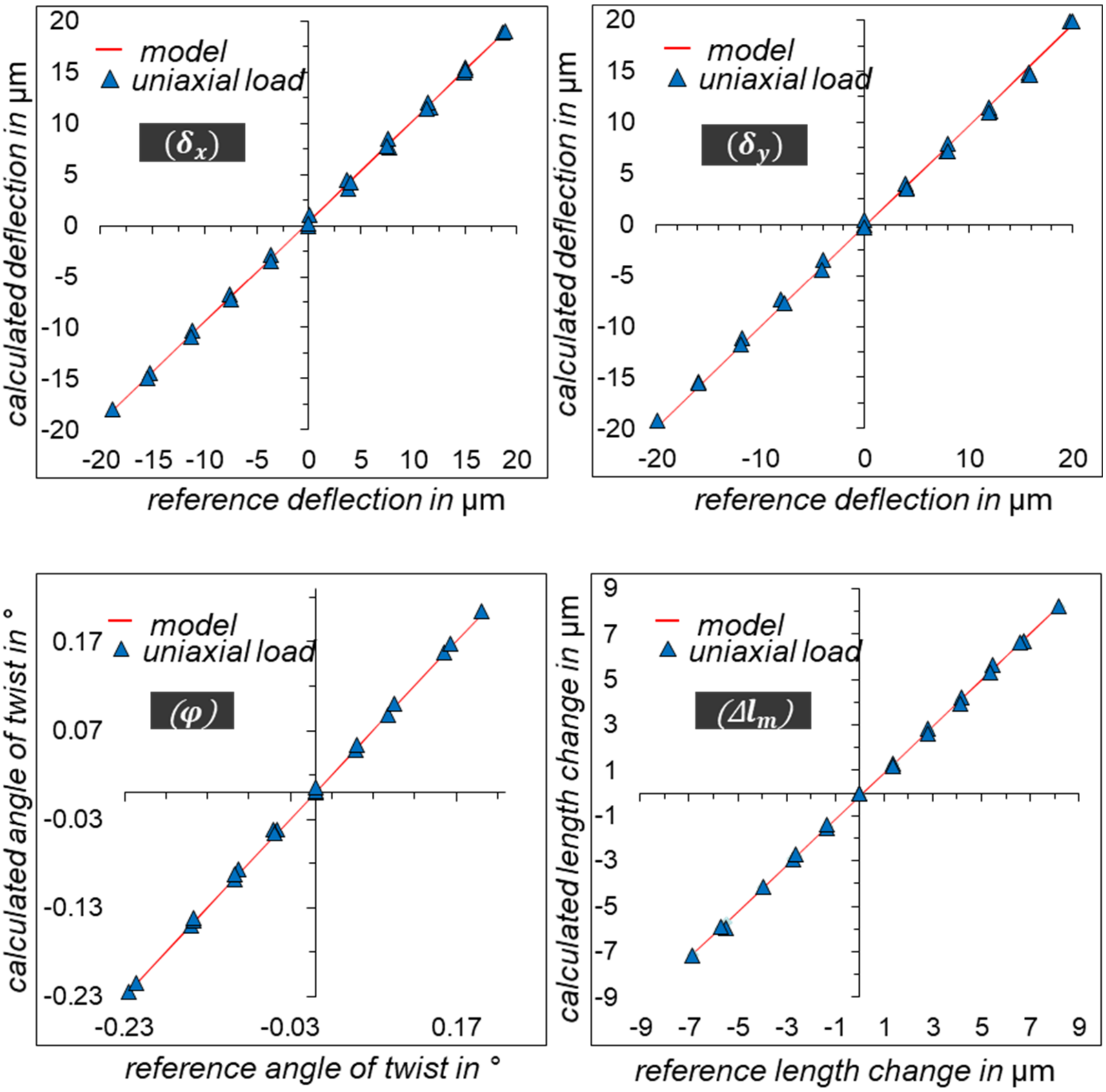

Figure 42: Results of uniaxial loading test [O3]

As shown in Figure 42, the deflections δ_x,and δ_y, the twist angle φ, and the length change Δl_m determined by the image-based sensor show a very good and linear correlation with the reference values.

5.1.3 Determining the crosstalk behavior

Before applying and recording multiaxial loads, the crosstalk behavior of in-plane displacements δ_{xy} and φ to out-of-plane displacement Δl_m must be determined according to equations (6) and (7), as explained in 4.2. First the angle ∅, by which the mirrored beam is twisted with respect to the image sensor coordinate system, is determined by uniaxial loading of the structure with F_x and

F_y, respectively, as depicted in Figure 43a. Based on the displacement caused both in the direct and mirrored image beams, the angle of rotation between both coordinate systems is determined. Afterwards, biaxial bending loads F_{xy} are applied, and the resulting displacement of $\Delta P_{3,4}$ at the mirrored image segment is transformed into the border line coordinate system ($\hat{x} - \hat{y}$) based on the determined angle $\emptyset$. Then, the correlations between the resulting in-plane displacement components (δ_x and δ_y) and the displacement components $\Delta P_{3,4\_}\hat{x}$ and $\Delta P_{3,4\_}\hat{y}$ at the mirrored image segment are determined after transformation to the coordinate system with $\emptyset$, as shown in Figure 43b and 43c. For the torsional load, the crosstalk between the direct and the mirrored image segments is investigated by determining the resulting angles of twist of both image segments. Figure 43d shows the resulting correlation between the twist angle φ and the corresponding rotation of the mirrored image segment.

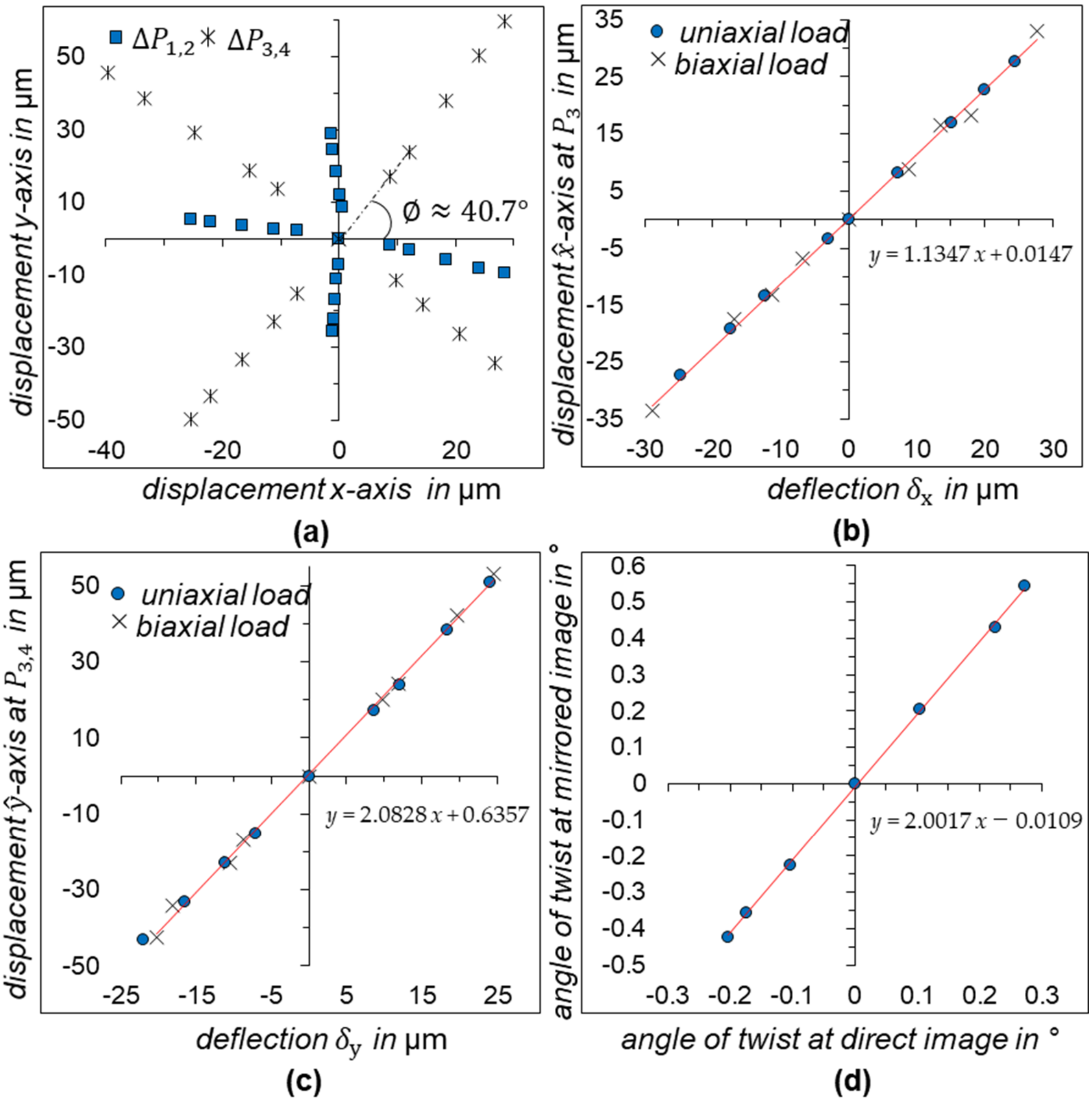

Figure 43: Characterization of the crosstalk behavior: a) determined angle ∅ of the border line; b) determined crosstalk between δ_x and $P_{3,4\_}\hat{x}$ for uniaxial (F_x) and biaxial (F_{xy}) loading; c) determined crosstalk between δ_y and $P_{3,4\_}\hat{y}$ for uniaxial (F_y) and biaxial (F_{xy}) loading; d) crosstalk of the twist angle φ on the mirrored image segment [O3].

As can be seen in Figure 43a, the border line between the mirrored and direct image segments is rotated by $\emptyset = 40.7°$ towards the x −axis of the image sensor. The calculated angle of rotation seems to be very accurate, as can be seen in the good correlation between the displacement $\Delta P_{3,4}$ along the $\hat{x}$- and $\hat{y}$-axes and the deflections δ_x and δ_y, respectively, for both uniaxial und biaxial loading. The slopes of the determined regression models in Figure 43b, 43c, and 43d are, however, slightly different from the theoretically expected values calculated in section 4.2. This is attributed to slight tilting of the mirror under bending load, which causes the mirrored light beam to be more displaced at the image sensor surface than caused by the actual displacement. The derived equation (6) is therefore modified with the determined slopes values to

$$\Delta\overrightarrow{l_m} = R(\emptyset)\cdot\left(\vec{c}_3 + \Delta\vec{P}_3 - \vec{c}_{\mathrm{CR\_m}} - \begin{pmatrix}\cos(\boldsymbol{2\varphi}) & -sin(\boldsymbol{2\varphi})\\ sin(\boldsymbol{2\varphi}) & \cos(\boldsymbol{2\varphi})\end{pmatrix}\cdot\left(\vec{c}_3 - \vec{c}_{\mathrm{CR\_m}}\right)\right) - (\mathbf{1.135} \quad \mathbf{2.081})\cdot R(\emptyset)\cdot\vec{\delta}_{xy} \tag{26}$$

with the modified crosstalk vector $(\mathbf{1.135} \quad \mathbf{2.081})$ instead of $(\mathbf{1} \quad \mathbf{2})$. $\vec{c}_{\mathrm{CR\_d}}$ and $\vec{c}_{\mathrm{CR\_m}}$ are determined by calculating the intersection points of two linear functions, which are described by the two points of each pattern point before and after a rotation caused by a mere torsional load; see Figure 44.

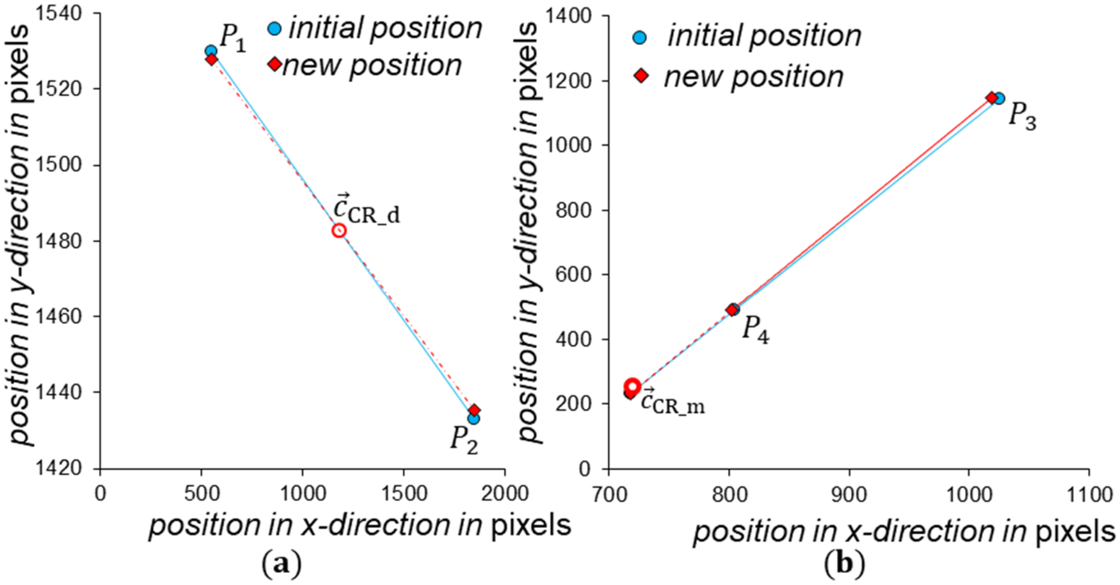

Figure 44: Determination of the centers of rotation for the direct and mirrored image segments by mere torsional load (a) for the direct image segment and (b) for the mirrored image segment [O3].

Figure 44 shows how the centers of rotation $\vec{c}_{\mathrm{CR\_d}}$ and $\vec{c}_{\mathrm{CR\_m}}$ are determined by applying mere torsional load. Together with the center of rotations for both image segments, the resulting strain $\Delta\overrightarrow{l_m}$ can be accurately determined according to equation (26).

5.1.4 Results for multiaxial loads (F_{x}+F_{y}+M_{z})

Similar to the uniaxial load tests, multiaxial load tests are also performed. The combined load is gradually increased and decreased. With the known center of rotation for the direct image segment $\vec{c}_{\mathrm{CR\_d}}$, in-plane displacement causing the load combination $F_x + F_y + M_z$ are applied. The measured displacements $\Delta\mathrm{P}_1$ and $\Delta\mathrm{P}_2$ are then calculated to δ_x, δ_y, and φ according to equations (3)−(5). Figure 45 shows the displacements occurring during this test.

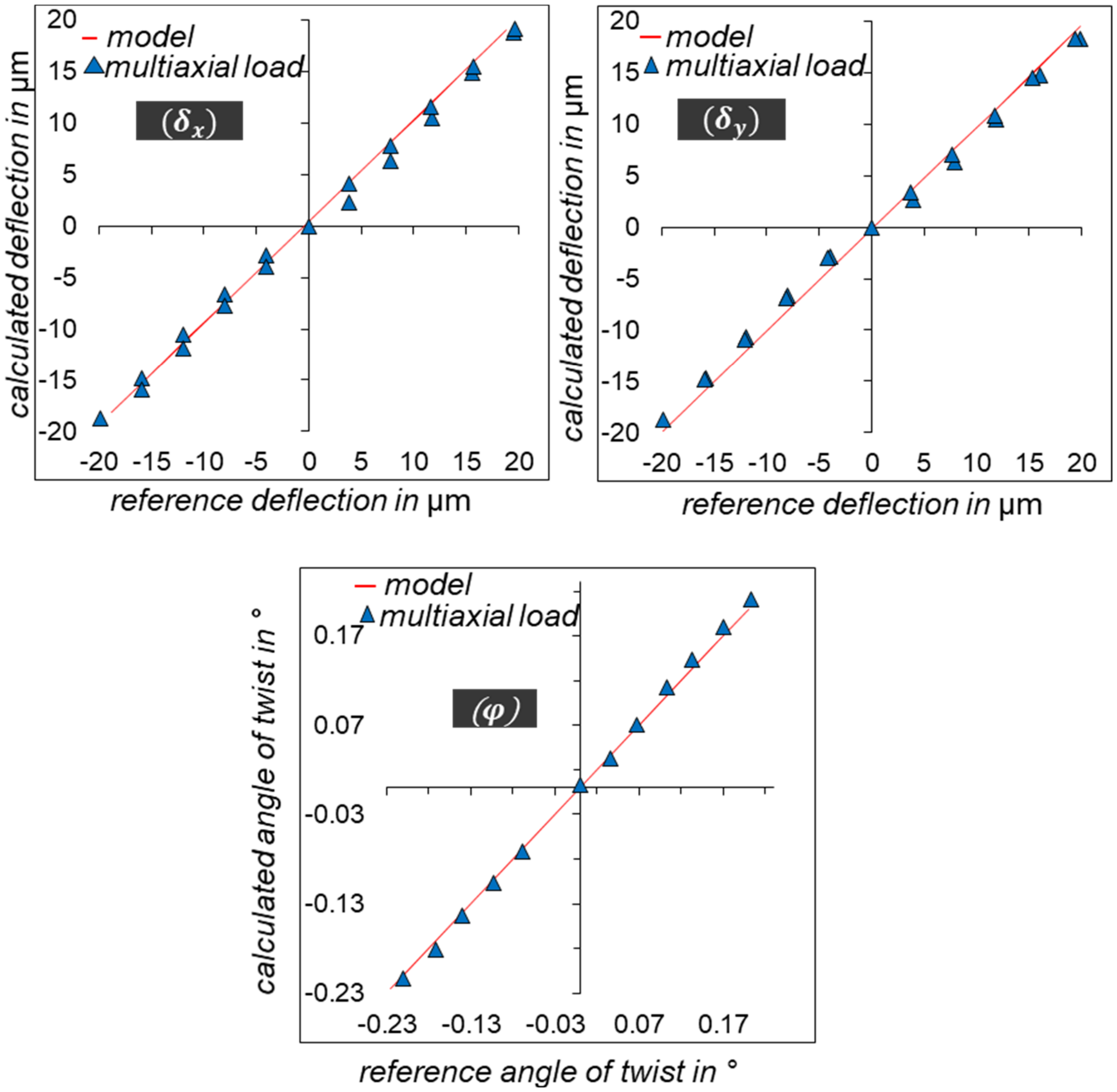

Figure 45: Calculated displacement components (δ_x, δ_y, φ) when the structure is under multiaxial loading with ($F_x + F_y + M_z$) [O3].

The calculated deflections δ_x and δ_y and the twist angle φ in Figure 45 also show good and linear agreement with the reference values. Compared to the uniaxial loads in Figure 42, a small deviation for deflection from the reference model can be observed. One possible reason for this deterioration is the screw joint used in the prototype (Figure 40), which is suspected of exhibiting settling behavior under multiaxial loading of the structure.

5.1.5 Results for multiaxial loads ($\boldsymbol{F_x + F_y + F_z + M_z}$)

Following the investigation of the sensor's behavior under multiaxial loads causing in-plane displacement ($F_x + F_y + M_z$), multiaxial loads, including the axial force F_z, are applied. In order to avoid any settling behavior in the bolts, the load ranges were reduced in comparison to previous tests as follows: F_x and F_y from ± 250 N to ± 100 N, F_z from ± 3 kN to ± 1 kN, and M_z from ± 65 Nm to ± 50 Nm. After applying the whole load combination ($F_x + F_y + F_z + M_z$), the measured displacements $\Delta\mathrm{P}_{1-4}$ are calculated to (δ_x, δ_y, φ, and Δl_m). Figure 46 shows the results for this load case.

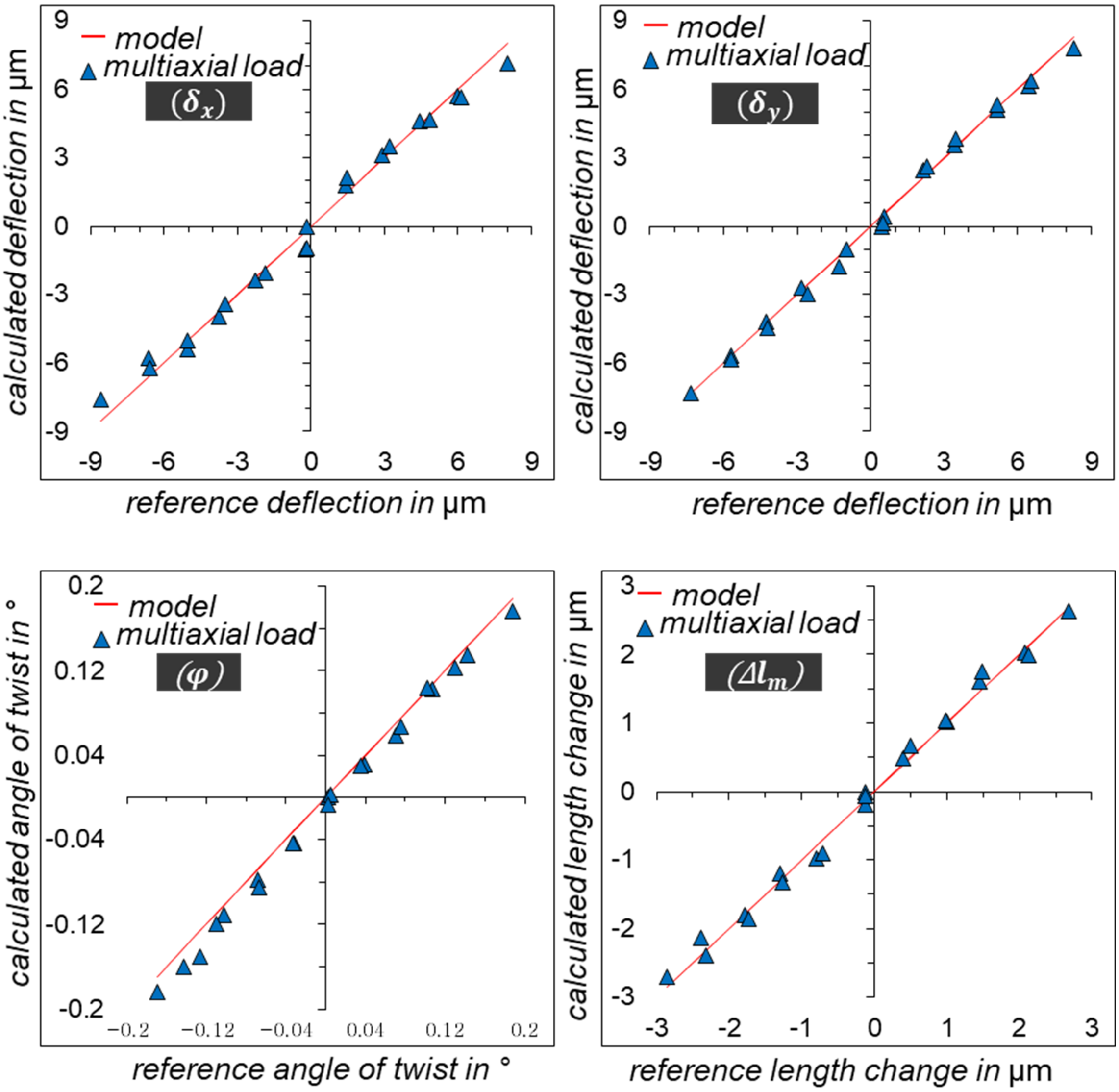

Figure 46: Determined displacement components (δ_x, δ_y, φ, Δl_m) when the structure is multiaxially loaded with ($F_x + F_y + F_z + M_z$) [O3].

The calculated deflections δ_x and δ_y and length change Δl_m in Figure 46 show good accuracy and linearity to the reference values, despite a reduction of the loading range and, thus, of the measuring range. However, the twist angle φ seems to have a higher deviation compared to the previous uniaxial M_z and multiaxial ($F_x + F_y + M_z$) load. The results show higher deviation comparing to the uniaxial load case with ($F_x + F_y$+M_z) in Figure 45. The accuracies achieved in the three loading cases with respect to the used regression models are shown in Table 2. The deviations are specified as the maximum relative error related to the maximum measured value for each displacement component (δ_x, δ_y, φ, Δl_m).

Table 2: Models used and the achieved accuracy of the results [O3].

Displacement component	Model	Max. measured value in µm	Load type	Max. deviation/ max. measured value in %
δ_x	$y = 1.014\,x$	20.65	F_x	2.58
			$F_x + F_y + M_z$	9.75
			$F_x + F_y + F_z + M_z$	2.50
δ_y	$y = 1.011\,x$	20.33	F_y	4.22
			$F_x + F_y + M_z$	9.77
			$F_x + F_y + F_z + M_z$	4.71
φ	$y = 0.996\,x$	0.242	M_z	2.45
			$F_x + F_y + M_z$	5.53
			$F_x + F_y + F_z + M_z$	10.43
Δl_m	$y = 1.0215\,x$	8.22	F_z	2.66
			$F_x + F_y + F_z + M_z$	3.18

As can be seen in Table 2, the models obtained deviate slightly from the theoretical value *1* under uniaxial loads, indicating a good robustness of the system, in spite of simple manual assembly of the prototype. However, the calculated deviation varies between 2.5% and 10.43%. The displacements (δ_x,δ_y Δl_m) under uniaxial and whole multiaxial loads show the best accuracy and almost the same deviation. The twist angle, on the other hand, shows a higher deviation with multiaxial loading.

5.1.6 Sources of measurement errors

The results shown in Figure 46 were only obtained by tightening the screws and simultaneously reducing the load range. Nevertheless, a deterioration in accuracy, especially compared to the results of the uniaxial loading case in Figure 42, remains visible. There was no critical observation regarding the image quality, for example, the disappearance of features under tensile load.

Due to the uniqueness of the features in their surroundings, no miscorrelation was suspected by the DIC algorithm. In this particular experiment, the structure length, respectively, the distance between the camera and the object, changed by only ± 9 µm, which is within the depth of field for the imaging system used. However, significant doubt relates to eccentric axial loading of the structure. Such loading will lead to non-uniform circumferential deformation of the structure and, hence, tilting of the carrier flanges, which can result in a falsification of the pattern displacement. In this case, the angle of twist would be strongly affected, since the pattern displacements under torque loading of the structure are relatively small compared to the displacements under bending or tensile loading. A look at the bending force and bending moment curves at loading cases $(F_x + F_y + M_z)$ and $(F_x + F_y + F_z + M_z)$ makes clear that, in the case of a multiaxial load combined with an axial load, no linear relationship can be found between the bending forces and the bending moments (see Figure 47). This means that the system behaves differently at each load step. Although the clear linearity in the load case $(F_x + F_y + M_z)$ indicates a homogeneous deformation of the structure during the whole test, this does not seem to be the case in the load case $(F_x + F_y + F_z + M_z)$, and a non-uniform deformation of the structure over the circumference due to eccentricity is assumed.

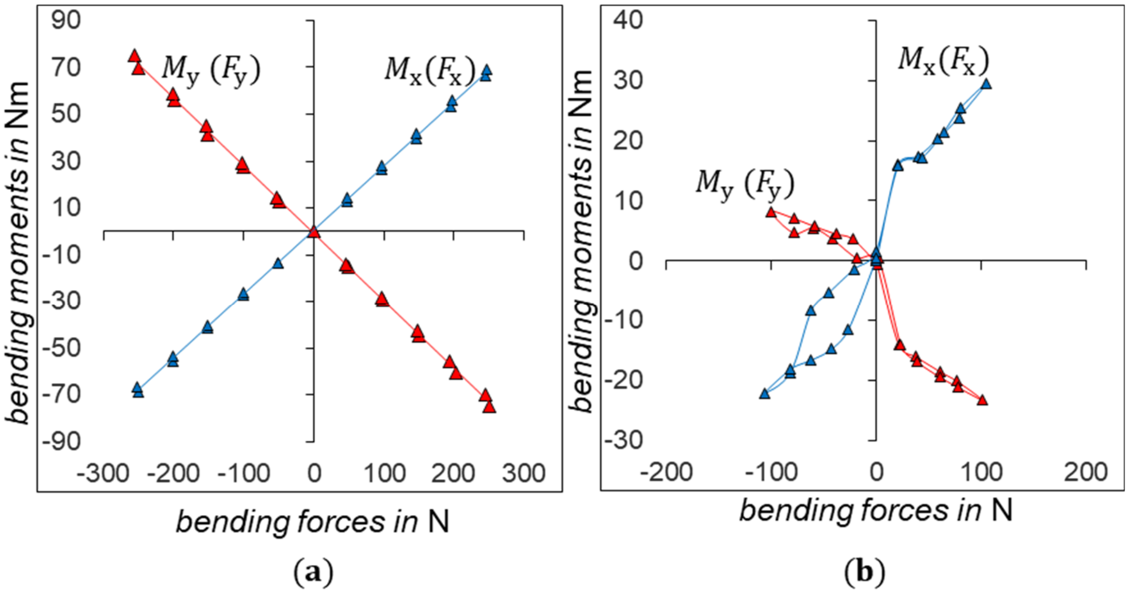

Figure 47: Correlation of bending moments to bending forces in both load cases (a) for $F_x + F_y + M_z$ and (b) for $F_x + F_y + F_z + M_z$.

As can be seen in Figure 47, the relationship between bending forces and bending is linear when the axial force F_z is not applied (a), and it is nonlinear, when F_z is applied (b). This behavior can be explained by the resulting eccentric axial load when applying an axial and bending load at the same time, leading to tilting of the measuring plane.

5.2 Measuring the Bending Moments and Machine Learning-Based Sensor Modelling

This sensitivity to tilting of the measurement planes under eccentric axial loads raises the question of whether it is possible to detect the nonlinear dependence between bending forces and bending moments to compensate for the resulting measurement inaccuracy. To address this problem, the system robustness is firstly increasing by press-fit integration of the sensor-carrying flanges into the tube, preventing any relative displacement between the sensor-carrying flanges and the host structure under load. After that, the applicability of deploying a machine learning algorithm for distinguishing between the resulting image changing under bending force and bending moments is investigated and compared to the use of a decision tree algorithm.

5.2.1 Sensor design, experimental test, and results

To achieve a high tolerance through press-fitting, the measuring concept is modified to use only one mirror, as shown in Figure 48a. Compared to the initial sensor design, tilting the upper beam path at an angle α allows for a reduction in the number of mirrors needed to only one, tilted at an angle of $\alpha/2$. As a result, the displacement of the mirrored beam dx while a length change Δl caused by an axial force F_z is reduced by the term $\tan(\alpha)$ as follows:

$$dx = \Delta l \cdot \tan\,(\alpha) \tag{27}$$

In contrast to the analytical approach for describing the crosstalk behavior in section 4.2, the crosstalk behavior of the modified sensor design will be described by means of a machine learning model that can predict the load components from the captured images. The model will be trained by captured images and their reference load values. Figure 48 depicts the sensor’s design and its installation in the test bench.

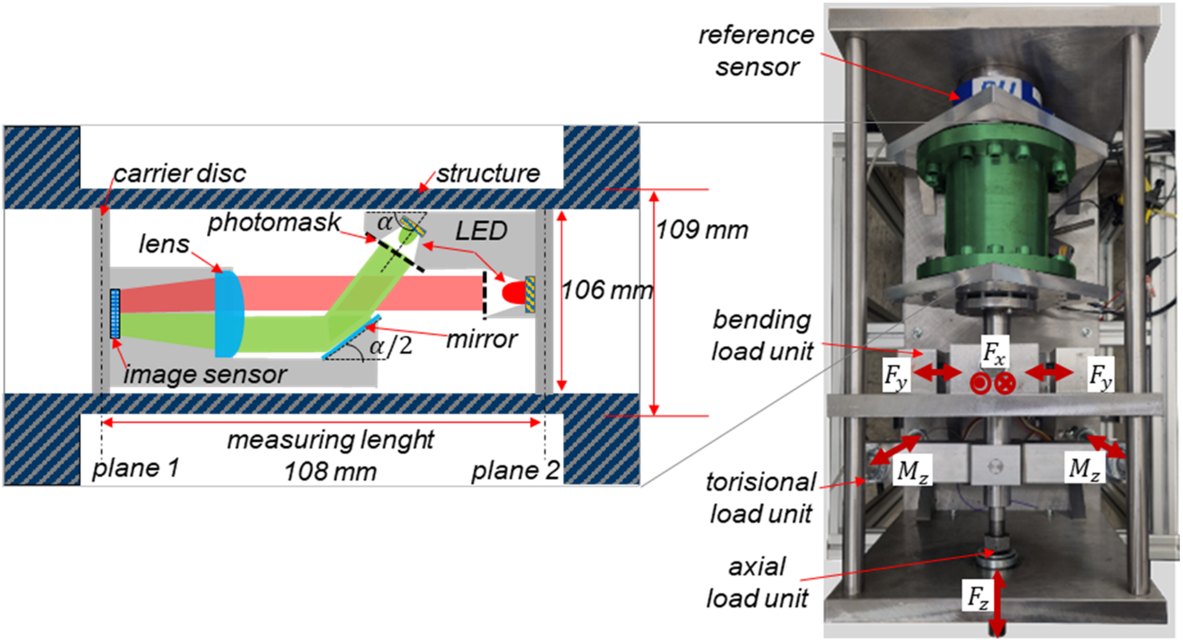

(a) (b)

Figure 48: (a) modified sensor design and (b) test bench for multiaxial loading of the sensor [O4].

As can be seen in Figure 48a, the sensor components are fixed in two thick discs that are press fitted into a flange-shaped metallic structure, as shown in [S1]. The sensor integrated flange is then fixed to the strain gauge based multiaxial sensor (HBM, K-MCS10-025) in a multiaxial loading test bench, and the loads are applied on the other side. To increase the measurement resolution, the lens system is designed to have a magnification factor of $M = 3.4$.

5.2.2 Measuring resolution of the measuring axis

Prior to determining the sensor behavior by means of a machine learning approach, the achievable measuring resolutions for each measuring axis (F_x, F_y, F_z and M_z) are determined through digital image correlation.

The loads were uniaxially applied in the range between F_{xy} ± 1 kN, M_z ± 250 Nm, and F_z ± 15 kN stepwise in 20 steps in both measuring directions. Because of the structure's high stiffness and the reference sensor's low maximum torque, an additional torsion test is performed on a torque calibration machine with a torque sensor (HBM TB2 1 kNm) loaded in the range of M_z ± 1 kNm.

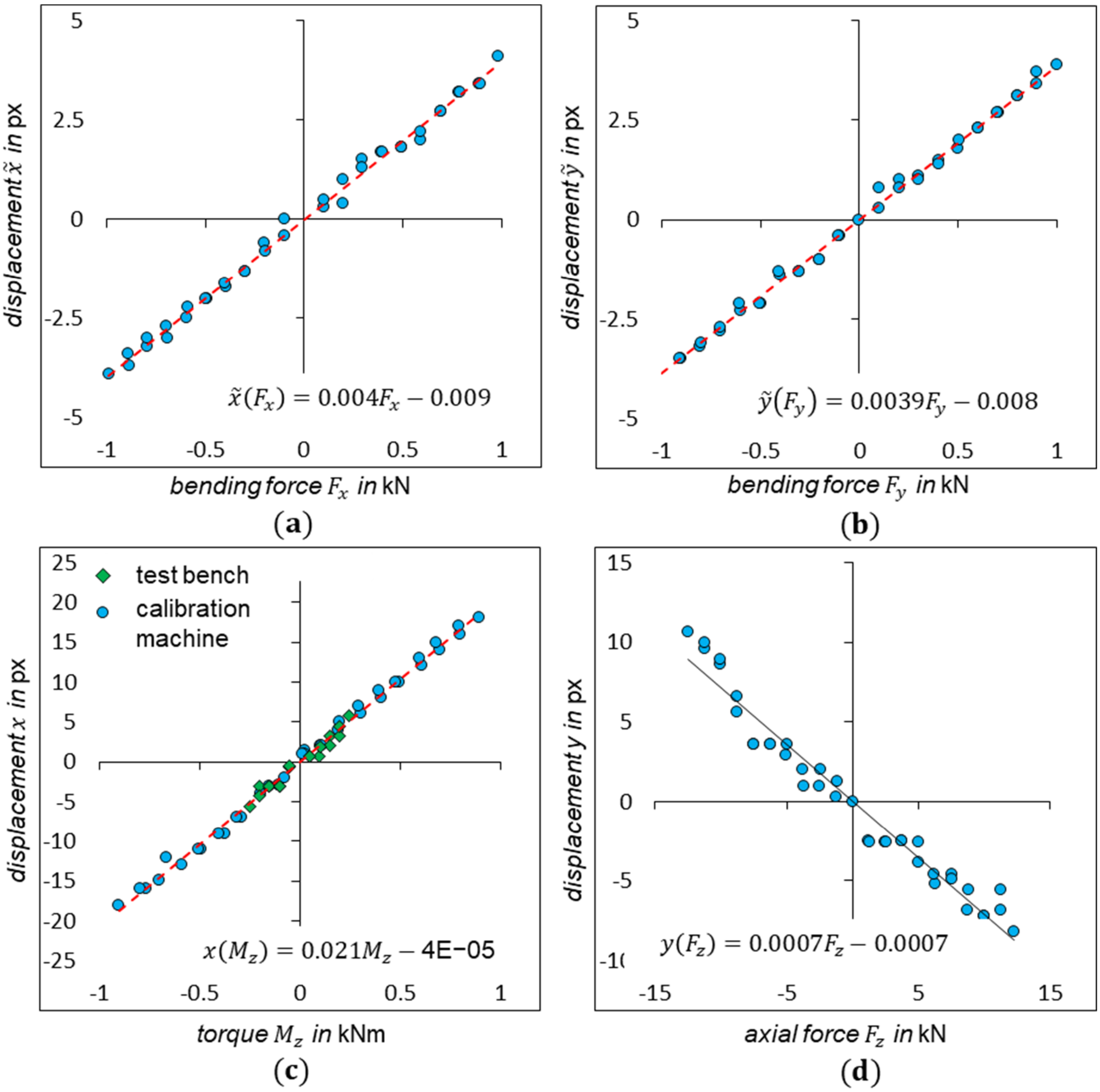

Figure 49: Results of uniaxial loads [O4].

As can be seen in Figure 49a and 49b, a linear behavior can be observed between the displacements and the bending forces. A maximum deviation of 104 N is determined for F_x and 100 N for F_y. In Figure 49c, the green boxes depict the load curve obtained from the developed test bench using the reference sensor at a torsional load ranging between ± 250 Nm. The blue circles depict the loads in the torque calibration system with a torsional load ranging from ±1 kNm. The calculated displacements show a maximum deviation of 95 Nm. However, for the axial force F_z in Figure 49d, a linear and more scattered curve can be observed. Here, a maximum deviation of 3.7 kN is found.

5.2.3 Sensor modeling using CNN

In order to model the system behavior under multiaxial loads, training data with the different load scenarios (F_x, F_y, F_z, $F_x + F_y$+F_z, M_z, $F_{xy} + M_z$) are collected with high density in the whole range. The captured images were reduced to four subsets: two subsets from the direct image segment and two from the mirror one. After selecting the color channel that provided the highest level of contrast, the grayscale values were normalized to between -1 and 1 to be fed into the CNN model [S5]. See Figure 50.

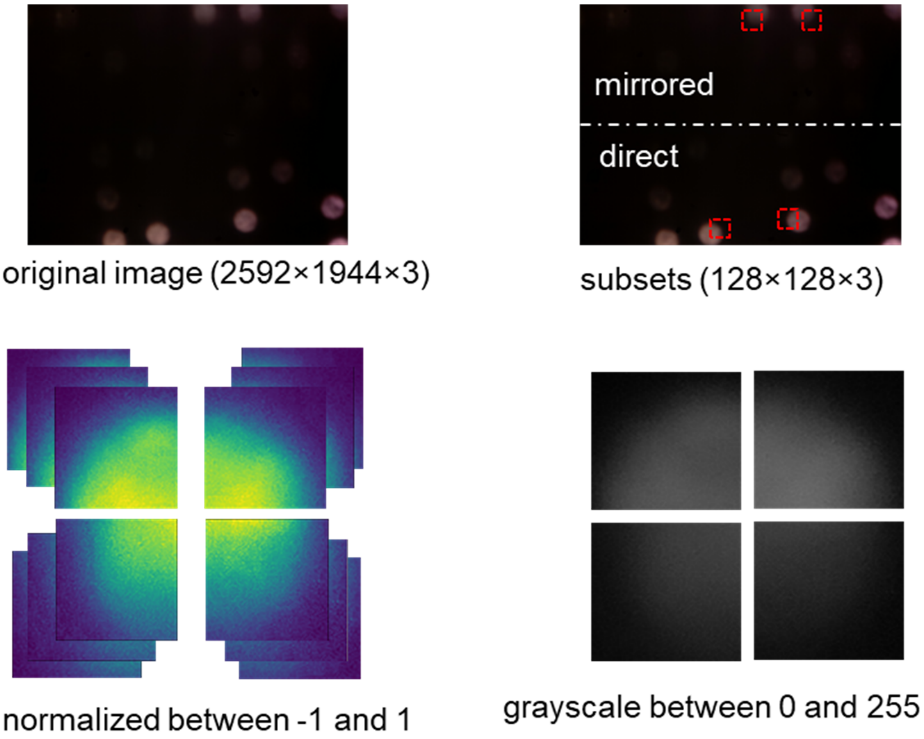

original image (2592×1944×3)

subsets (128×128×3)

normalized between -1 and 1

grayscale between 0 and 255

Figure 50: Image pre-processing for the CNN model [S5].

As can be seen in Figure 50, the four subsets comprise quarter circles, two from each image segment. As discussed by Zhang on the pre-trained CNN model, MobileNetV2 seems to be very suitable for the underlying classification problem, combined with a HydraNet approach for data augmentation [S5].

5.2.4 Sensor modeling using decision tree regression

An alternative method to implementing machine learning algorithms with a better understanding of the system behavior is using decision tree regression (DTR) coupled with a displacement determination algorithm, such as DIC or CNN, as described in Chapter 4.5. The displacements from each of four subsets, shown in Figure 50, are used as the input for a decision tree regressor, which can then predict loads based on a pre-training phase. See Figure 51.

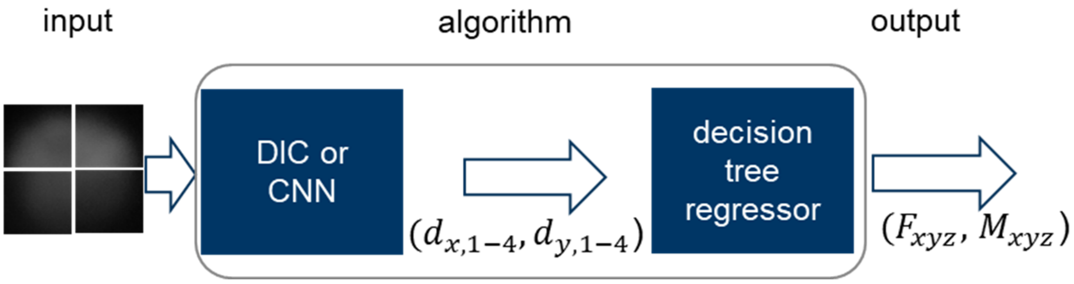

Figure 51: Load determination using a decision tree regressor.

Figure 51 presents the process of determining applied loads from captured images. Firstly, the captured images are cropped into four subsets of interest. Subsequently, the displacements are calculated and used as input into the pre-trained decision tree regressor.

5.2.5 Results

The results of both approaches demonstrate the ability of machine learning algorithms to recognize sensor behavior and to accurately detect load characteristics from the captured images. Figure 52 shows the results achieved for predicting the applied load (F_x, F_y, F_z, M_x, M_y). Due to the high torsional stiffness of the prototype and the low torque measuring range of the reference sensor, as can be seen in Figure 49c, the influence of torque was not investigated.

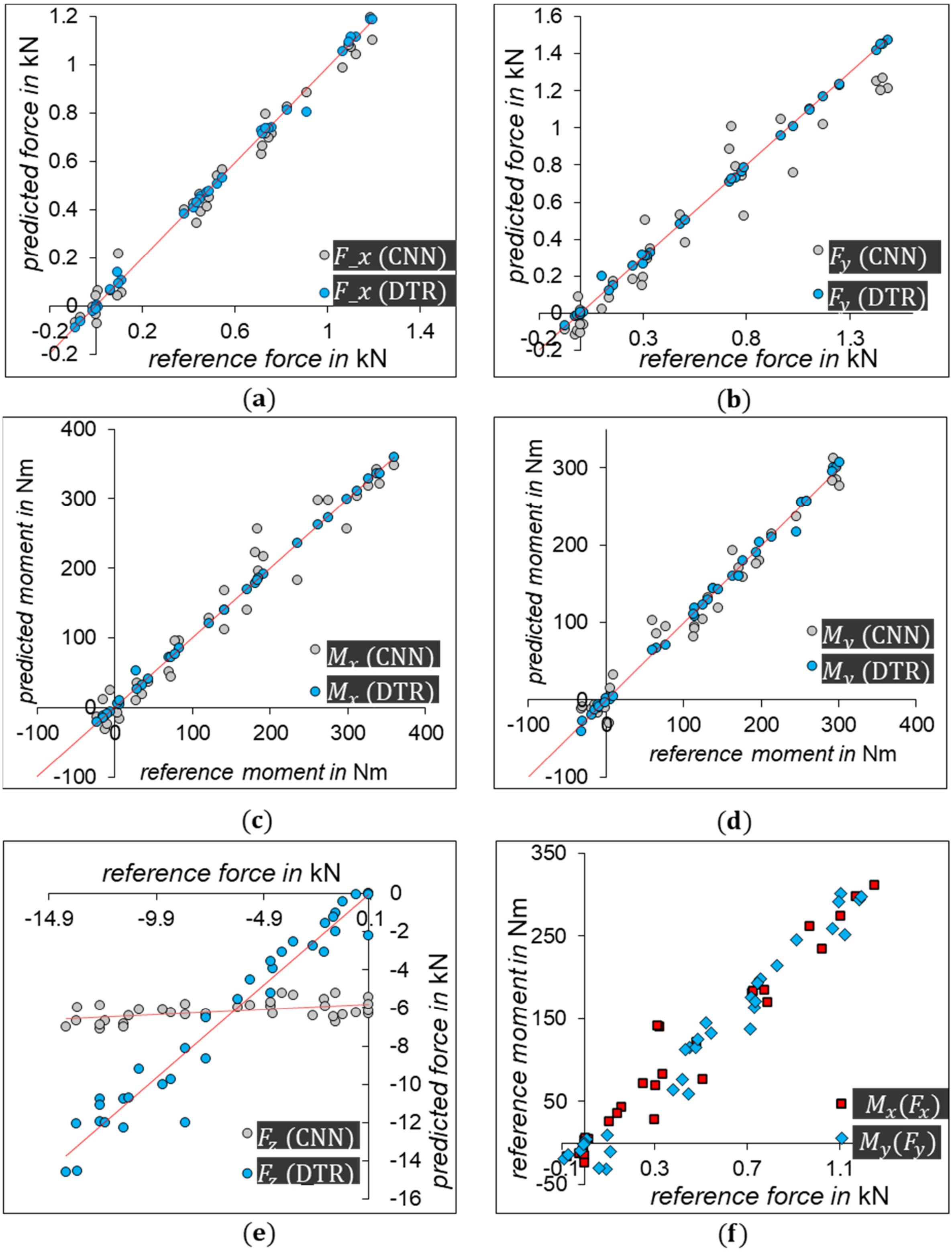

(a) (b) (c) (d) (e) (f)

Figure 52: Results of machine learning-based load prediction according to [S5]: (a) and (b) for the bending forces, (c) and (d) for the bending moments, (e) for the axial force, and (f) showing the non-linear relationship between the applied bending force and bending moments.

The results of load prediction for both the CNN and DTR approach in Figure 52a–e show the DTR provided a significantly better prediction compared to the CNN algorithm. The prediction of bending moments and bending forces is also remarkably accurate despite the nonlinear relationships between the two, as shown in Figure 52f. In addition to improved prediction accuracy, the DTR model takes advantage of using the calculated 2D subset displacements as inputs, as opposed to the feature vector of an input subset in CNN. This characteristic reduces the amount of training data required compared to the CNN model.

The table below compares both algorithms' maximum errors in predicting loads as well as the deviations of the loads determined by evaluating the displacements under uniaxial loading shown in Figure 49.

Table 3: Comparing the maximum errors in load prediction for both CNN and DTR algorithms as well as for the DIC-based determination.

Load	CNN	DTR	DIC-based
F_x	119.83 N	105.80 N	104 N
F_y	385.66 N	101.40 N	100 N
M_x	82.91 Nm	27.40 Nm	-
M_y	43.02 Nm	28.40 Nm	-
F_z	4.5 kN	3.5 kN	3.7 kN

As can be seen in Table 3, the errors of the DTR algorithm are very close to those calculated by the DIC algorithm. This shows that the DTR algorithm is highly accurate in recognizing the load components from the displacements and that the prediction accuracy is directly dependent on the pre-computation of the displacements.

6 Examples of Industrial Applications

After evaluating the ability of the developed multiaxial image-based sensor to detect multiaxial loads, this chapter emphasizes its ability for high-resolution detection of deformations in stiff machine elements. For this, the sensor is integrated into two stiff machine elements to measure their deformations under load.

6.1 Sensor Bending Roll

6.1.1 Combined bending-linear flow splitting process

According to Groche et al., linear flow splitting is a multi-station sheet-bulk metal forming process allowing the continuous production of bifurcated profile shapes without the need for joining, or external heating [GRO18]. In the final process step, the profile is bent to the desired curvature by bending rolls, as shown in Figure 53. In this process, measuring the bending forces that occur during bending is essential for process monitoring and early fault detection. Although small variations in force can have a noticeable effect on final profile geometry, they cause very little significant elastic deformation of the bending roll. Furthermore, depending on the height of the bending radius, the direction of the bending force varies during the bending process. This places high demands on the measurement resolution of the bending force in both magnitude and direction.

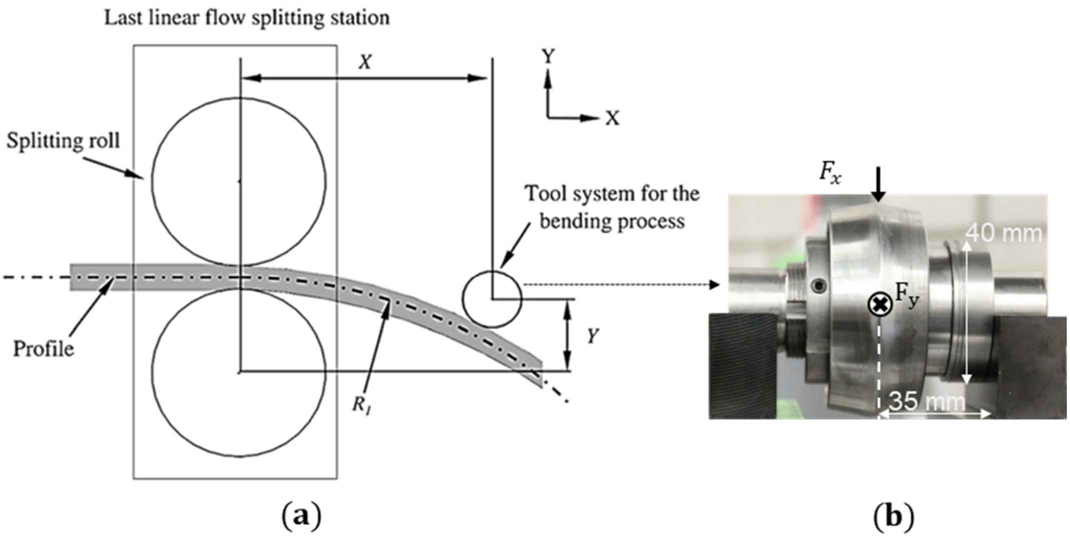

Figure 53: (a) Illustration of a bending-linear flow splitting process [GRO18] and (b) the bending roll used in this study with its dimensions

6.1.2 Sensor design and assembly

The specified profile bending process requires a bending force measurement resolution of 100 N within a measurement range of 20 kN. Since the measurement focuses only on bending forces, the sensor design has been simplified and involves only a direct light beam. This simplification allows the lens system to achieve an optical magnification of $m = -15$. An Omnivision Ov5647 image sensor with an imaging area of 2592 x 1944 pixels and a pixel size of 1.4 x 1.4 µm is used. A hole with a diameter of 20 mm is drilled in order to install the sensor inside the pin, and the two sensor parts were adhesively bonded to the pin. Figure 54 illustrates the sensor integration into the bending roll carrying pin.

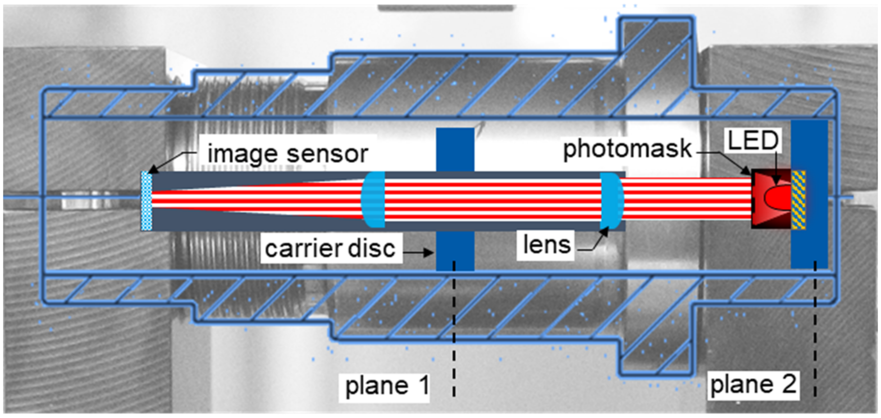

Figure 54: Sensor installation inside the pin of the bending roll [O5].

Once the bending forces F_x and F_y are applied, the pin is deflected marginally, and plane 1 is displaced downwards. The relative movements between plane 1 and plane 2 in the $x-y$ plane are recorded by the image sensor, and the resulting displacements are then determined. Prior to its use, the sensor is calibrated.
As can be seen in Figure 54, when the bending forces F_x and F_y are applied, the pin is slightly deflected, and plane 1 is displaced in the force direction. The relative movements between plane 1 and plane 2 in the $x-y$ plane are recorded by the image sensor, and the resulting displacement is then determined.

6.1.3 Calibration process and the impact of clamping conditions

One difficulty with double-sided clamped pins is that the deformation behavior depends on the clamping condition. The pin deflection decreases as the clamping force increases. Lower clamp forces, conversely, result in tilting of the clamped pin side (plane 2 in Figure 54). Figure 55 shows the effect the clamping condition has on the plane displacement of the integrated image-based sensor.

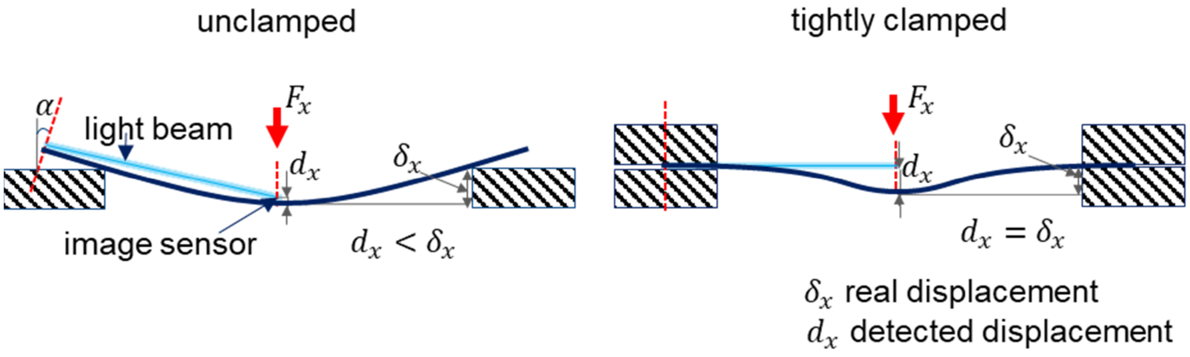

Figure 55: Visualization of the displacement of the measuring plane according to the clamping situation [O5].

As shown in Figure 55, in the case of an unclamped pin, a plane tilting at the tilt angle α occurs, resulting in compensation of the true displacement caused by the translational disc shifting under load. In this case, the displacement detected by the image sensor d_x is less than the actual pin deflection δ_x. In the case of a tight clamping, no tilting will occur, and the plane displacement can be fully detected by the integrated sensor $d_x = \delta_x$.

To investigate the influence of clamping conditions on the measurement results of the assembled sensor pin, the pin is loaded in four different clamping scenarios by applying specific tightening torques to the bolts in the clamping shells (0 Nm, 5 Nm, 15 Nm, and 25 Nm), see Figure 56b. Afterwards, a ZwickRoell Z100 tensile and compression testing machine incrementally applies a bending force ranging from 0 N to 16 kN to the center of the pin. The deflection of the pin under load is measured by the integrated sensor and two laser distance sensors (Keyence LK-H020) mounted externally. The central laser distance sensor evaluates the displacement of the pin's middle plane, while the outer one measures the displacement of the entire test setup under load. The gathered information is combined to determine the exact deflection of the pin's middle plane. The signal from the external laser distance sensor is combined with the reading from the central sensor. The test setup and resulting displacements from both the integrated and external sensors under different pin-clamping conditions are depicted in Figure 56.

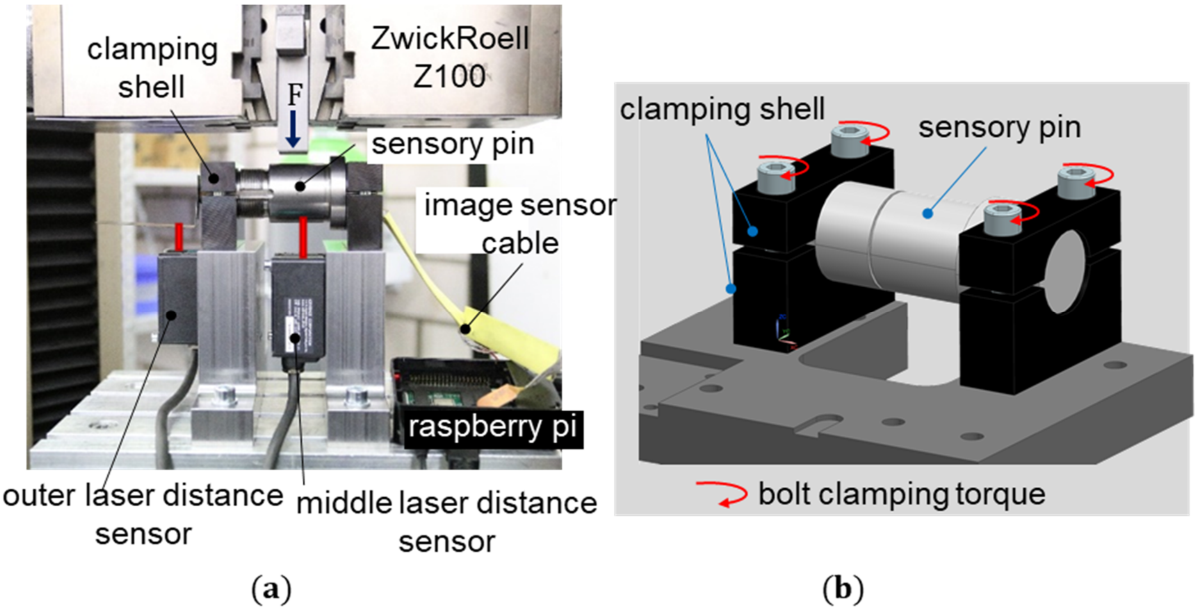

Figure 56: Determination of the influence of the clamping situation on the measurement resolution (a) experimental setup [O5] and (b) visualization of the variation of the clamping force by the bolt clamping torque.

Figure 57 presents the results of the experiment, which illustrate the compression force curve, the deflection measured by the laser distance sensors, and the plane displacements detected by the integrated sensor under the four clamping conditions.

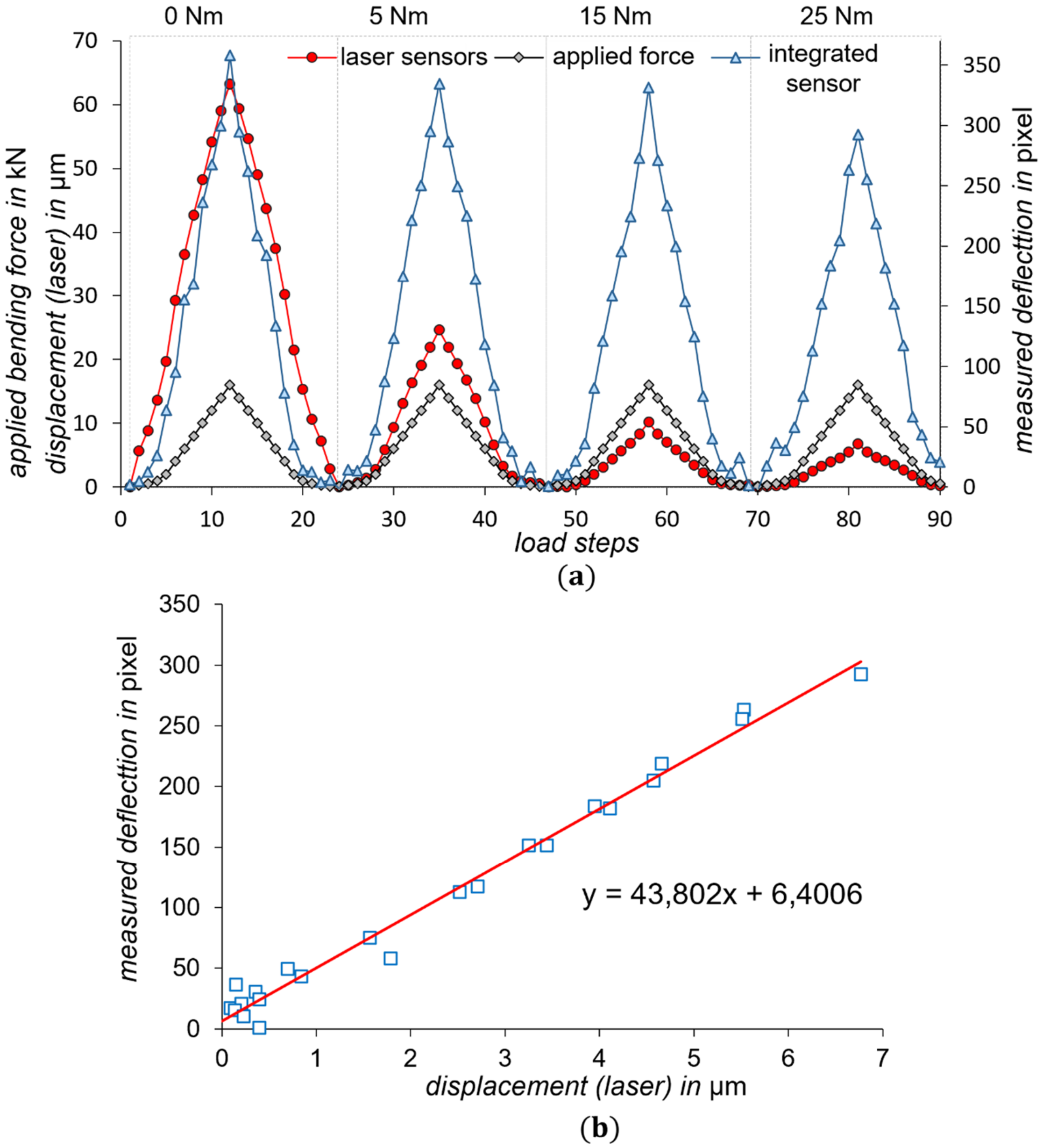

Figure 57: Results of the experimental investigation into the influence of the clamping situation on the pin deformation behavior. Curves of the integrated and external laser sensor according to [O5] (a) and correlation between both sensors at a clamping torque of 25 Nm (b).

Figure 57a shows how the amplitude of the pin deflection measured by the external laser sensors decreases as the clamping torque increases. In contrast, the deflection measured by the integrated image-based sensor does not exhibit this distinct change as the clamping torque increases. This is attributed to the significant influence the plane tilt has on the image-based sensor, as shown in Figure 55. At the maximum clamping torque of 25 Nm, it can be assumed that no plane tilt occurs, and both the integrated image-based sensor and the external distance laser sensors measure the same pin deflection. In this case, the integrated image-based sensor can be calibrated by correlating it to the external sensor (see Figure 57b). At a slope of 43.8 pixels/µm, the measuring resolution of one pixel displacement is approximately 22.8 nm.

6.1.4 In-situ calibration of the bending roll and experimental trials

To ensure accurate measurement of bending forces during the bending process, it is essential to calibrate the bending roll, including the bearing and roll element, after it is mounted in the bending device. The calibration process involves applying uniaxial loads along the x-axis and y-axis directions. These loads are systematically applied in multiple steps within the expected maximum loading range, specified as F_x up to 2 kN and F_y up to 17 kN. Figure 58 provides an illustration of the calibration setup.

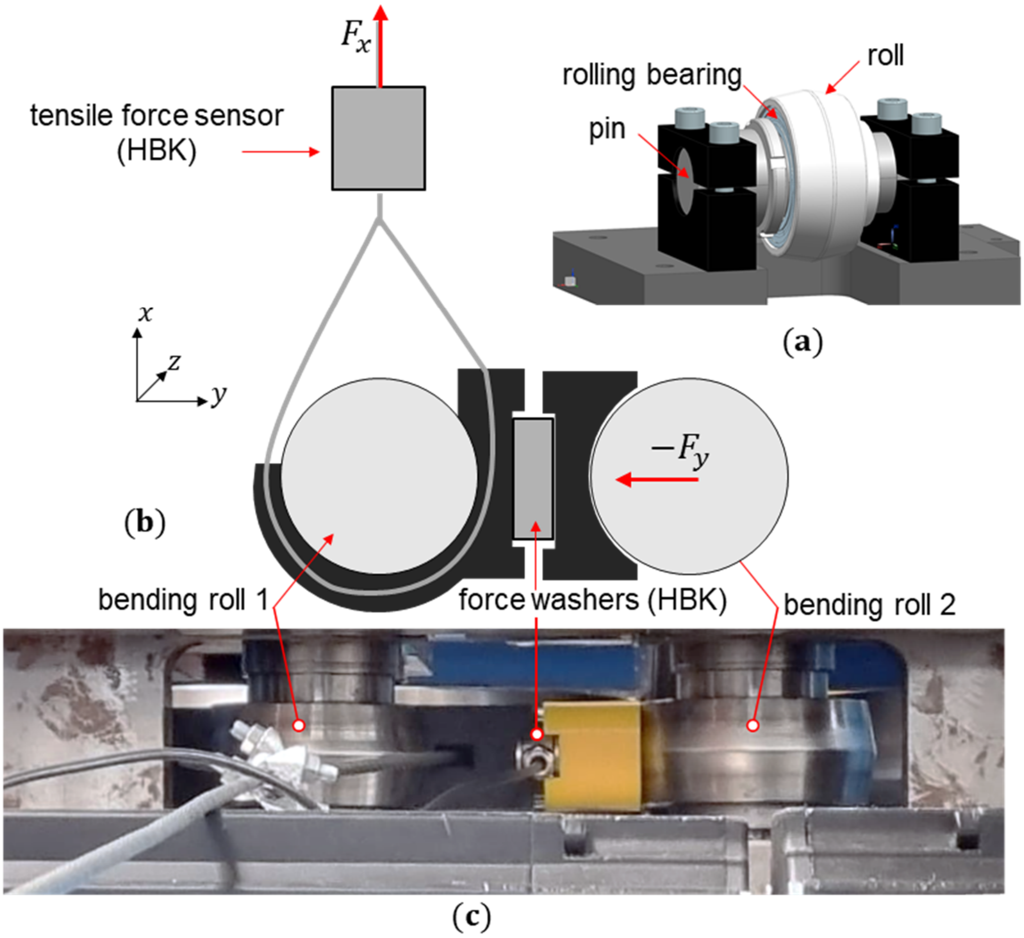

Figure 58: Experimental setup for in-situ sensor roll calibration (a), bending roll assembly and schematic illustration (b), and in (c), a picture of the calibration setup

Figure 58 shows how the tensile force F_x is applied by pulling a wire around the roll using a 3D-printed adapter, thereby pulling the roll in the x direction. The force is applied stepwise by incrementally tightening a threaded rod device pulling the wire. A HKB tensile force sensor is built within the wire to measure and monitor F_x. Conversely, the load in the y direction is realized by moving the second bending roll toward the first by machine control. The force F_y in the y direction is measured with a HKB force washer sensor that was integrated using a 3D adapter. This setup allows for uniaxial and controlled stepwise force application in both directions.

The results of the sensor bending roll calibration are shown in Figure 59. The force displacement curves exhibit a slightly quadratic behavior, which could be attributed to the damping effect of the built-in bearing.

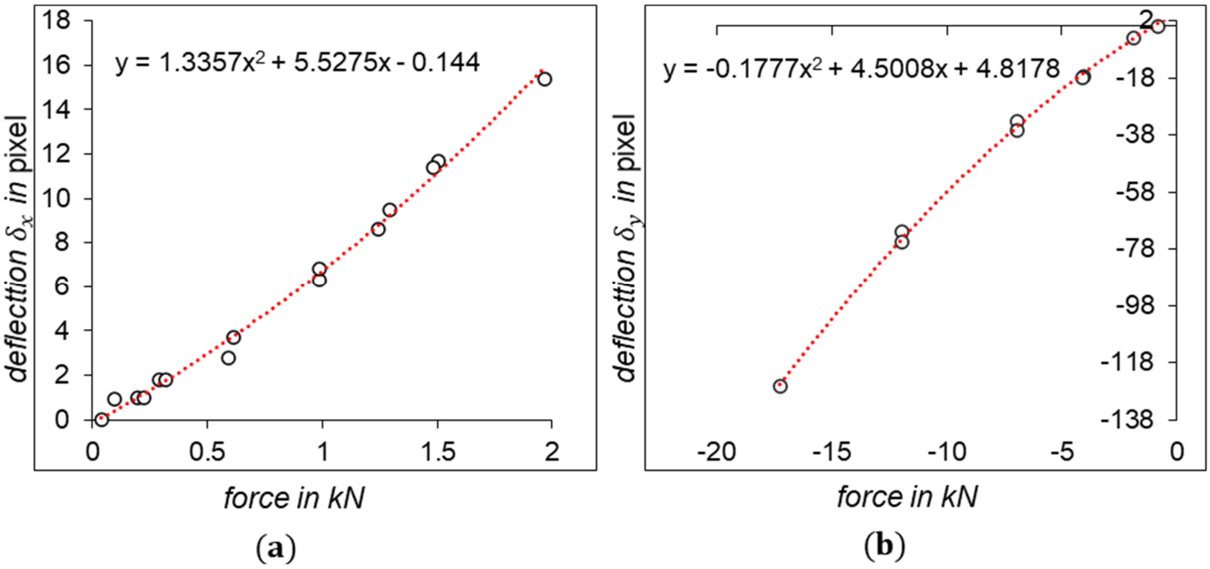

Figure 59: Results of the in-situ bending roll calibration for F_x (a) and for F_y (b).

After in-situ calibration of the roll, profile bending trials are carried out with different roll infeed positions. The bending roll deflection during the bending process are measured by the integrated image-based sensor in $x-$ and $y-$direction and the corresponding bending forces are then calculated based on the calibration curves in Figure 59. Figure 60 illustrates a schematic of the bending process and the measured bending forces for two different roll infeed positions.

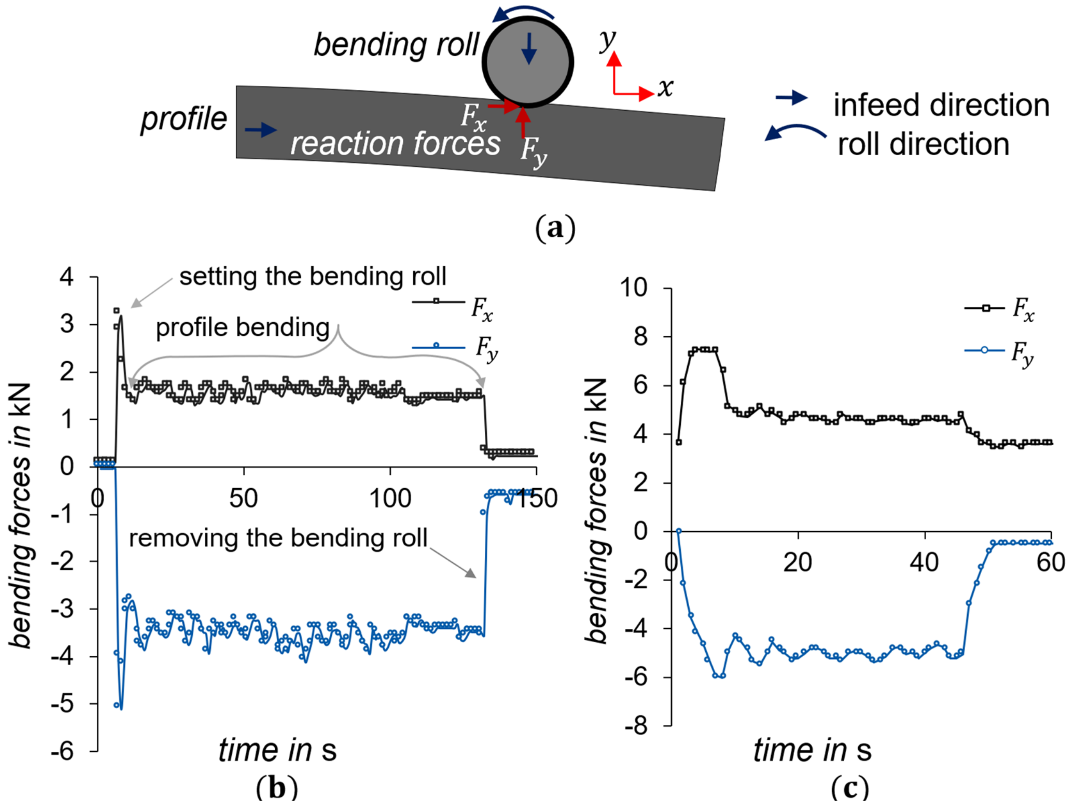

Figure 60: Measurement of bending forces during profile bending at different roll infeed positions: (a) schematic of the bending process; (b) bending forces for an infeed position of 20 mm according to [O5]; and (c) for an infeed position of 50 mm.

As shown in Figure 60a, as the bending roll is fed into the profile, the force rapidly increases before stabilizing at an almost constant force level. Here, the roll's position is kept constant and its rotation during profile feed causes a wave-shaped force curve. At the end of the bend, the force drops, as shown in Figure 60b and Figure 60c. The bending process begins by feeding the bending roll into the forward feeding profile. The force curves increase with the bending roll's infeed position. The forces in the direction of profile feed, abbreviated F_x, are notably smaller than those in the forward feed direction of the bending roll, abbreviated F_y. As the bending roll's infeed increases, the force in the x-direction increases. As Taplick showed in his investigations, the resulting radius of the bent profile depends directly on the bending force applied by the bending roll [TAP16].

6.2 Sensor Guidance Column

6.2.1 Blanking tool and tool misalignment problem

Blanking is one of the most widely used cutting techniques in sheet metal forming, especially for standardized production in the automotive and electronics industries [CAN17]. In this process, a vertically moving punch, mounted on a punch holding plate, descends to perform material blanking against a stationary lower die, mounted on a die shoe [VEN21]. Accurate alignment between punch and die is ensured by guiding the upper and lower plates with guide columns [VEN21]. Figure 61 shows a blanking tool installed in a Bruderer stamping press.

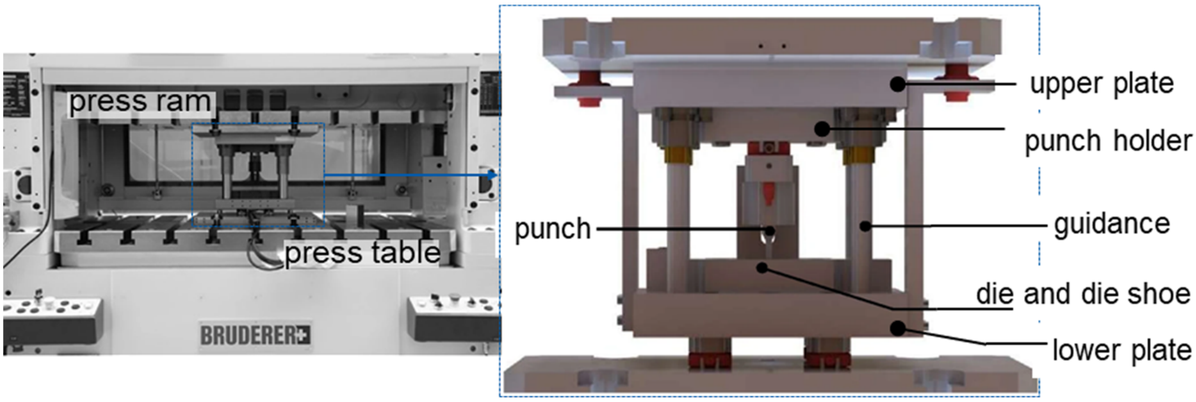

Figure 61: Blanking tool setup in a BSTA 810 stamping press according to [MOL22].

As described by Hirsch, any misalignment between the punch and the die can affect the final product geometry or result in tool wear [HIR12]. Since these mass production forming processes are usually carried out on high-speed press machines, Hirsch stated that horizontal tool vibrations may lead to an indeterminate position between punches and the die. Conversely, the vertical movement can escalate wear due to heightened friction forces between the blanked surface and the lateral area of the punches [HIR12]. In his investigation, Kraus emphasized a correlation between tool vibration, increased relative tool movement, and resulting tool wear [KRA18].

Assuming that any relative lateral movement between the upper and lower die plates caused by an unbalanced workpiece in the forging process will result in a certain deflection of the guide column, Kim et al. demonstrated how this deflection can be detected by measuring the resulting stress condition at the column clamp via sensor bolts [KIM18].

In the context of validating the image-based deflection sensor, the sensor is similarly integrated into a guide column in order to measure the deflection that occurs when the upper plate tilts.

6.2.2 Sensor assembly experiment setup

Since the guidance column can only be subjected to bending loads, a sensor design to measure only in-plane displacement is installed. For this reason, one of the guidance columns (length 280 mm and diameter 38 mm) is drilled to have an inner hole with a diameter of 22 mm. The lens system is designed to achieve an optical magnification of $m = -13$. In contrast to earlier sensor configurations, the current setup involves mounting a lens on the LED side rather than the image sensor side. This adjustment facilitates improved light focus on the sensor over longer distances. See Figure 62.

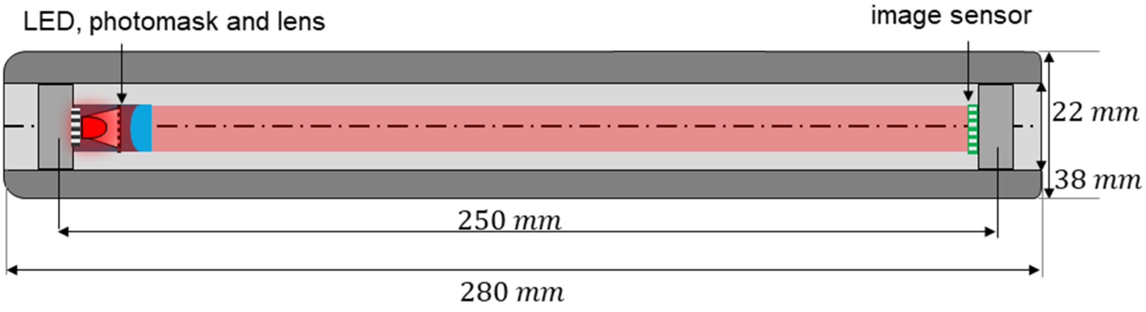

Figure 62: Sensor installation inside the guidance column

The sensor guidance column is mounted on the left of the front side of the blanking tool shown in Figure 62. After the column was pressed into the lower plate, calibration is performed by applying loads to the top of the column in the x and y directions. This resulted in a displacement of 1 px, corresponding to 1.8 µm. To evaluate the ability to measure possible tool deflections due to possible lateral motion between both tool plates or upper plate tilting, the upper plate is artificially tilted by inserting thin sheet strips with different thickness to the left and right side of the upper plate. The tool's top plate is then clamped tightly to the press ram. The ram is then moved up and down without blanking a specimen, so that only the effect of column deflection under upper plate tilting is measured. Figure 63 shows the assembly of the sensor guidance column in the blanking tool and visualizes the resulting tilting moment M_y when a sheet is inserted on the right side of the column.

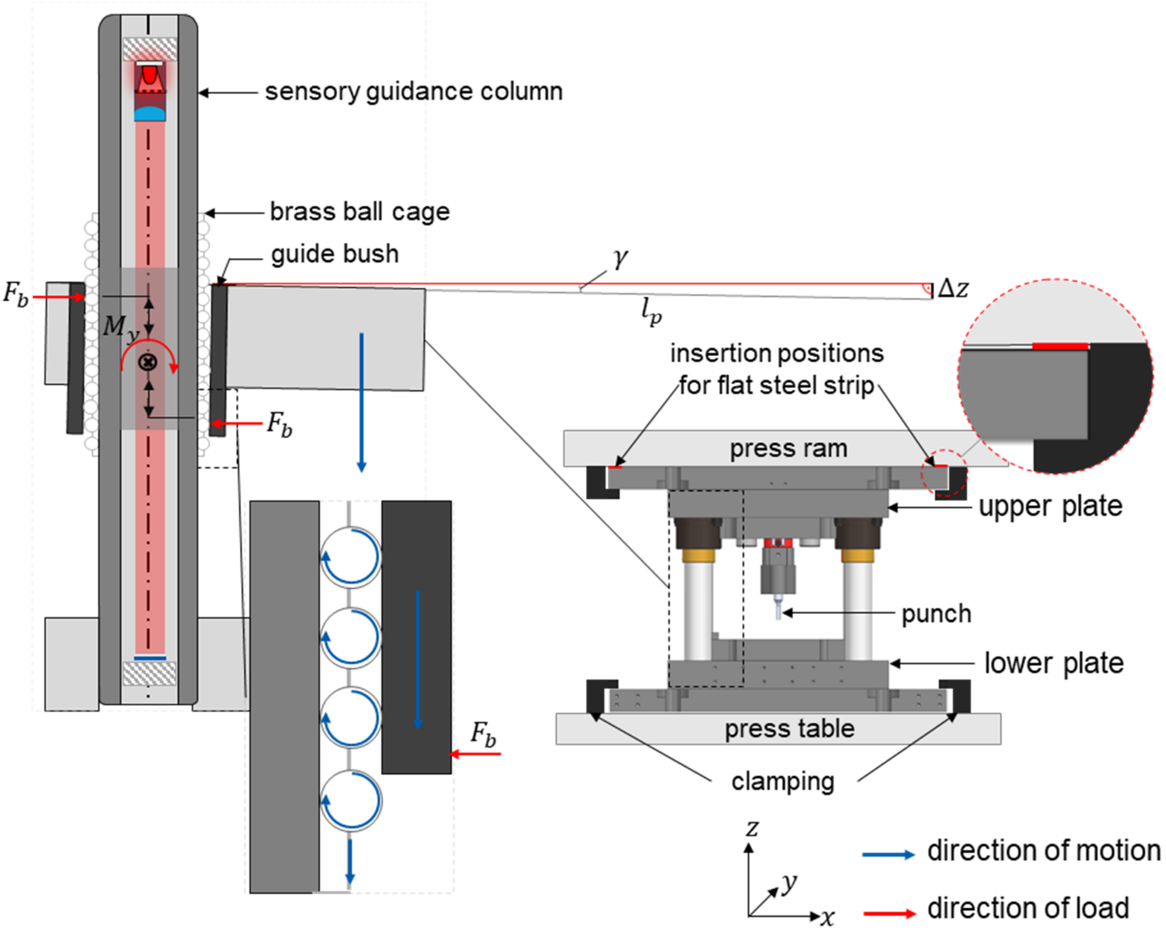

Figure 63: Assembly of the sensor guidance column within the blanking tool. Column bending moment M_y induced by the tilt on the right side of the upper plate during the vertical plate motion along the column

As shown in Figure 63, inserting the red metal strip between the upper plate and the press ram causes the plate to tilt by an angle γ, which can be calculated from the sheet thickness and the distance between the column and the strip insertion position l_p as follows:

$$\gamma = \arcsin\left(\frac{\Delta z}{l_p}\right) \tag{28}$$

In the blanking process, the upper plate moves up and down the column through brass ball cages, so the tilting of the upper plate creates compressive forces F_b that are transmitted to the column through the balls, resulting in a bending moment M_y, as shown in Figure 63. Inserting the flat steel strips on the right side of the column results in a positive moment M_y and a positive deflection in the x-axis. Conversely, inserting on the left results in a negative M_y and a negative deflection in the x-axis. The distance l_p from the insertion position to the guidance column is 130 mm on the left side and 355 mm on the right. This difference in distance results in different tilt angles for the same strip thickness. Table 4 shows the sheet thicknesses used for validation and the corresponding column tilt angles for both insertion positions.

Table 4: Sheet thicknesses and the corresponding column tilt angles

Sheet thickness	Tilt angle left	Tilt angel right
0.01	0.004407°	0.001614°
0.1	0.04407°	0.01614°
0.25	0.1102°	0.04035°
0.5	0.2204°	0.0807°
1	0.4407°	0.1614°

During the validation process, three strokes were performed at each tilt angle, with each stroke taking 60 seconds. The column deflections were measured and evaluated.

6.2.3 Results

The results in Figure 64 demonstrate how very small tool tilts can be detected with distinct and good reproducible deflections; see Figure 64b and Figure 64c. The high measuring resolution of the integrated image-based sensor allows the detection of a column tilt angle as small as $\gamma = 0.001614°$, as shown in Figure 64b. Additionally, a small column deflection is detected without any upper plate tilting, indicating a tilted column assembly into the lower plate (curve for 0mm in Figure 64a). The observed step-shaped column deflection is due to the fact that when the guide bush moves up and down over the rolling balls, the contact points with the column move outwards with each new ball contact, resulting in a longer lever arm and, thus, higher bending moments. See the illustration in Figure 63. Although the tilting on the left side is greater than on the right side, the deflections on the left side have slightly smaller amplitudes. This is due to the deeper-reaching clamping tool on the left side, which can result in non-linear plate deformation, thereby reducing the resulting column tilt.

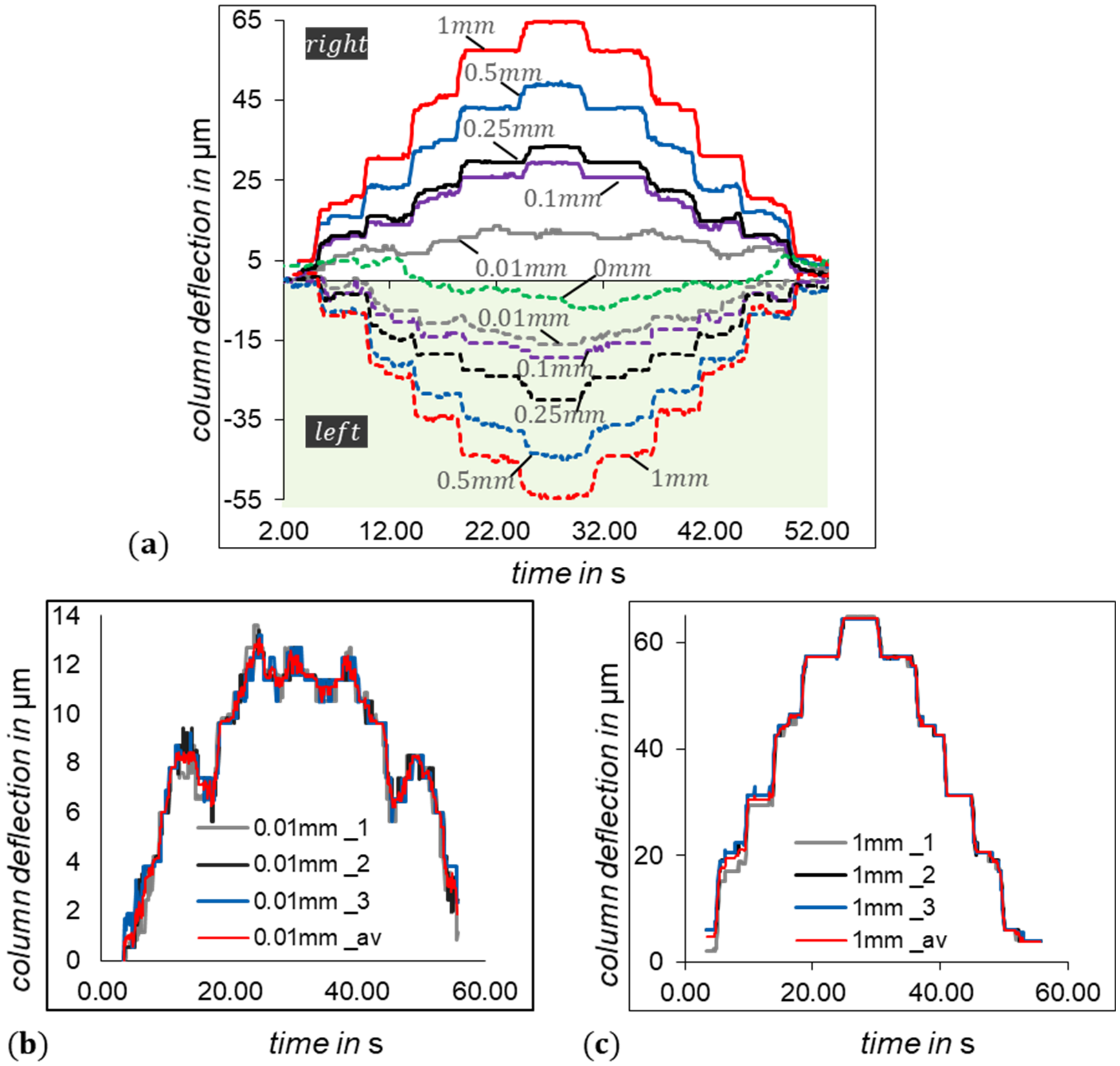

Figure 64: Curves of column deflection under all tilt variations. (a) Averaged curves of all variations for right (top) and left (bottom). Curves of the three repetitions, including the average curve for a tilt to the right of $\gamma = 0.001614°$, (b), and $\gamma = 0.1614°$, (c)

7 Sensor Integration by Rotary Swaging

To ensure the reliability of our image-based sensor's measurements, the required positional accuracy of the two sensor parts to each other is important, as well as a reliable connection to the host structure under all expected loading conditions. During sensory functionality validation on various prototypes, the sensor-carrying discs are mounted into the host structure by screwing (section 5.1), press-fitting (5.2), and, finally, adhesive bonding (5.3).

Investigations into sensor integration into host structures through forming have highlighted several beneficial aspects, such as the capability to force and form-fit sensors joining into metallic structures, as discussed in [O1]. In particular, previous studies at the PtU on sensor integration by rotary swaging have shown a high degree of flexibility in controlling the sensor properties during the forming process.

However, all previous studies on sensor integration by means of forming technologies so far have been limited to the integration of electromechanical transducers, where a target stress condition of the integrated sensor within the host structure is the most important aspect for a successful sensor integration process. Conversely, the optical non-contact sensor concept presented here requires a high degree of positional accuracy when integrating the sensor into the structure in order to ensure its functionality.

In the process of sensor integration by rotary swaging, a diameter reduction of the tubular structure is performed, while the sensor bearing discs are positioned within the structure and fixed by mandrels. This results in joining the discs within the structure, as illustrated in Figure 65.

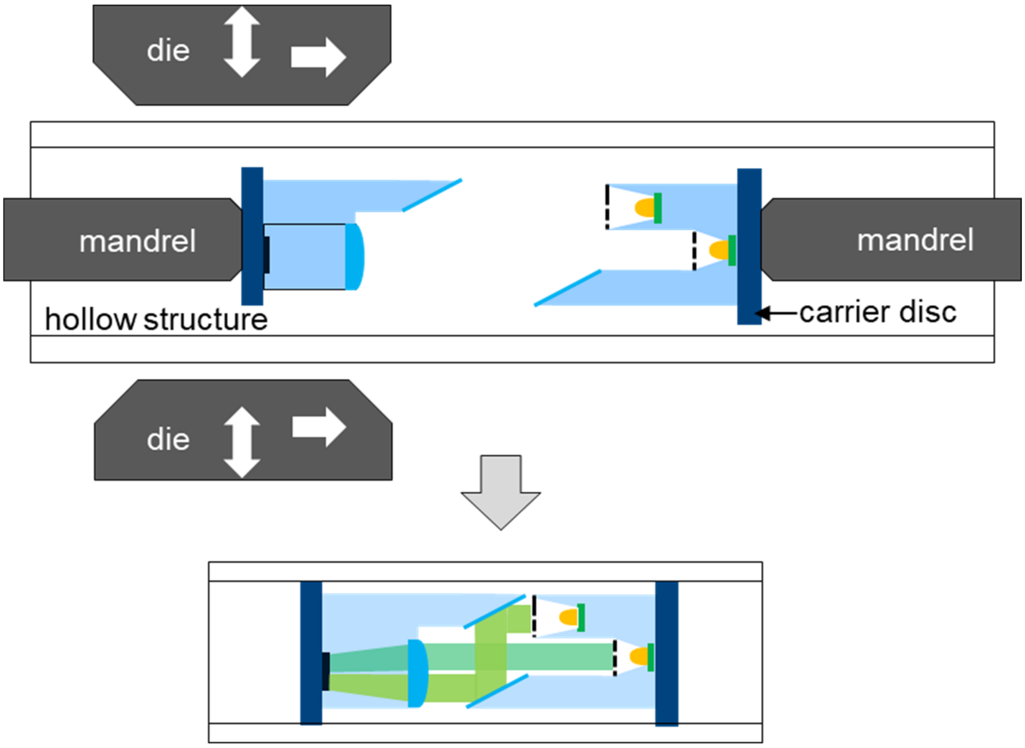

Figure 65: Visualization of a possible process design for sensor integration by rotary swaging.

As visualized in Figure 65, the two discs will be fixed by two mandrels at certain positions. However, it is possible to integrate the two sensor-carrying discs in sequence. To ensure successful sensor integration, the following objectives are set for the joining process:

1. Ensure high positional accuracy between the two sensor parts with respect to each other.
2. Achieve a reliable and backlash-free joint under all expected load conditions of the sensor structure in the use phase.
3. Ensure damage-free joining of the sensitive optical element.

Joining a disc within a hollow structure by reducing the inner diameter of the hollow structure poses a buckling problem. The radially-acting compressive forces on the disc during tube diameter reduction could cause sudden buckling of the disc. This, in turn, gives rise to axial-acting forces that significantly affect the positioning accuracy of the disc inside the structure. In addition, the carrier disc is only fixed in the structure by a force-fit connection. Furthermore, the high radial forces acting on the workpiece can damage the sensitive optical elements. To meet the derived objectives, a special joining partner and joining process design must be developed for the rotary swaging process. This chapter presents the developed process design, as well as the results of numerical and experimental investigations.

7.1 Process and Joining Partners Design

An approach for meeting established objectives is to accomplish a reliable form- and force-fit disc joining within the structure with a low joining force. The carrier disc is designed to have two primary regions: a relatively rigid core, which acts as a mounting base for optical elements and ensures no deformation during joining, surrounded by a thin, easily deformable rim. Internal teeth inside the tube aid the initial penetration of the thin rim into the tube with minimal joining force required, locking the disc in position within the teeth. As the diameter decreases, the disc continues to penetrate the toothed structure. The increase in contact area between the disc edge and the tooth structure results in increased compressive stress and, thus, elastic deformation of the thin rim. This generates a force-fit connection in addition to the form-fit. Figure 66 demonstrates this approach.

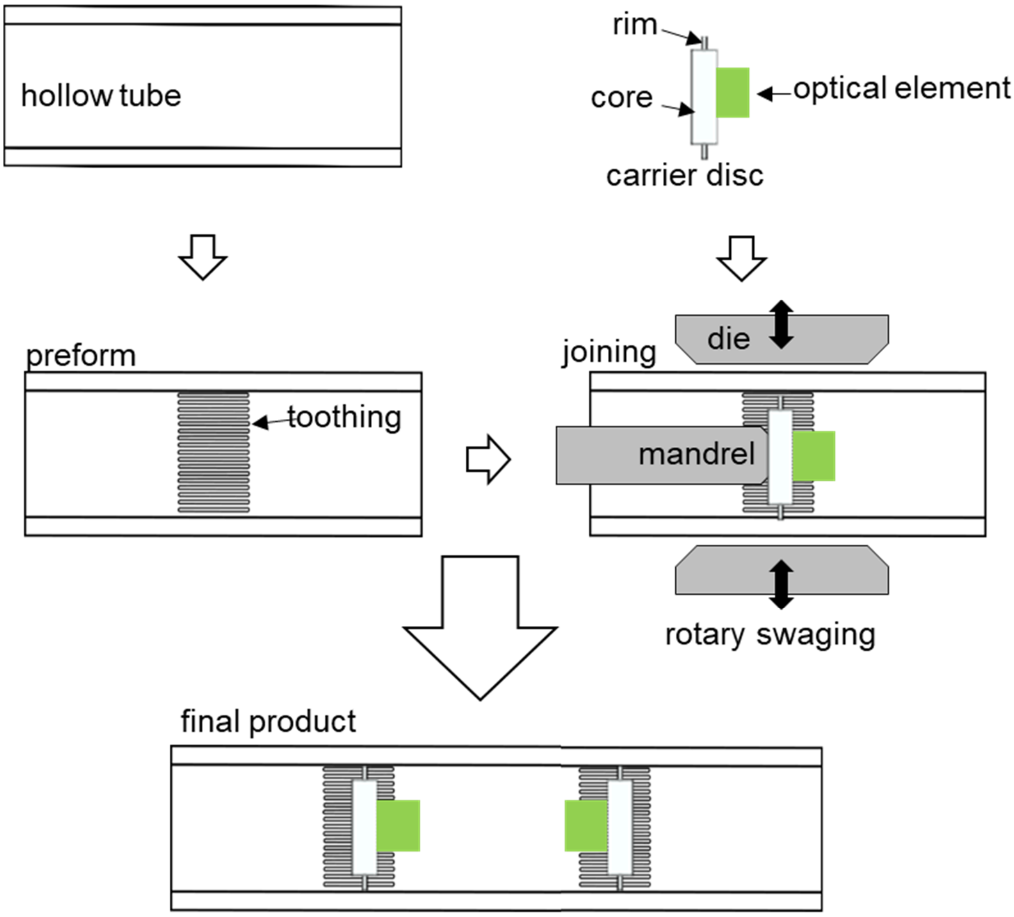

Figure 66: Joining partner and joining process design approach [O1].

As shown in Figure 66, the sensor elements are mounted at the center of a disc consisting of a rigid core and a relatively thin rim. The tube, conversely, is preformed to have teeth at a predefined position. A mandrel is used to position the disc inside the tube and hold it in place during the rotary swaging process. During the joining process, the stiffness ratio between the disc and the toothed tube determines the ratio between the form- and force-fit joining. Increasing the number of teeth promises to increase the disc stability inside the tube during the joining process and prevent any tilting. However, it will increase the force required to penetrate the teeth and reduce the degree of the form-fit joining. A similar behavior can be observed when increasing the disc's rim thickness. Both the material and the geometry define the stiffness ratio between the two joining partners, and thus the joining formation.

7.2 Numerical Process Simulation

The influence of the rim geometry and the number of teeth on the ratio of form-fit and force-fit joints is obtained by numerical simulation. Table 5 shows the chosen material for both joining partners and the parameter variation for the numerical simulation, as well as the tooth geometry.

Table 5: Material and parameter variation for both joining partners.

S355J2G3 steel	1.2379 steel
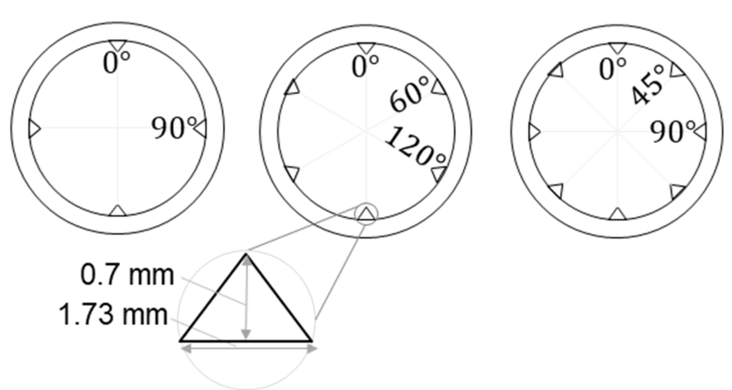	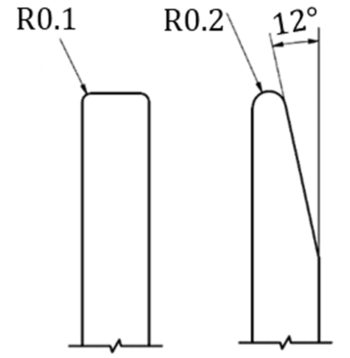

To avoid early plastic deformation of the rim during penetration into the tooth, the pin is made of 1.2379 steel with a high yield strength (σ_y= 420 MPa), while the tube is made of S355J2G3 with a lower yield strength (σ_y= 355 MPa). In the numerical simulation, two variants for the rim edge – chamfered and non-chamfered – were considered. The number of teeth is also varied between 4, 6, and 8; see Table 5.

7.2.1 Preliminary simulation and basics of model parameters

Due to the high deformation of the teeth during disc penetration, optimizing the mesh shape and mass scaling is needed to improve simulation accuracy. In a typical Abaqus mesh algorithm, the inner elements become small and triangular in the shape of a tooth. At larger deformations, the elements become entirely flat, which results in simulation abortion. In order to avoid this problem, the internal nodes must have a specific distribution to avoid the creation of very small elements, as has been investigated by Heck [S6]. Furthermore, the Arbitrary Lagrangian-Eulerian algorithm for remeshing (ALE) is used to create a more uniform aspect ratio within the mesh. Figure 67a and Figure 67b show the simulation parameters and the resulting deformation behavior during the joining process.

	Tube	Disc
Material Properties	**Mild Steel**	**1.2379**
E-Modulus [MPa]	210000	210000
Poisson's Ratio [-]	0.33	0.33
Rp0.2 [MPa]	300	699.5
Rm [MPa]	385	990
Element type	C3D8R	
target time increment	10^{-6}s	

(a)

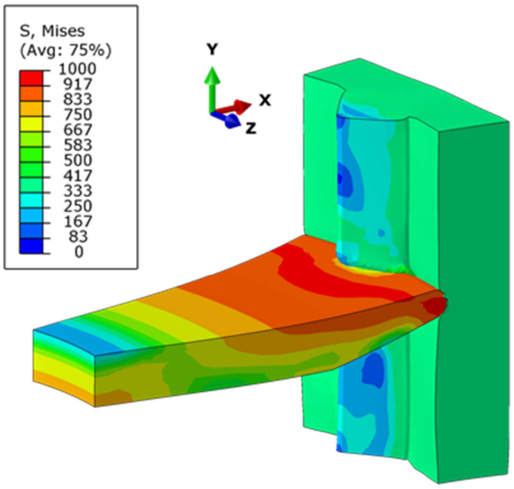

(b)

Figure 67: Preliminary simulation and basic model parameters: (a) simulation parameter settings and (b) achieved disc penetration behavior [O6].

The difference in materials allows the tooth to undergo plastic deformation earlier, making it easier for the rim to penetrate. As the rim approaches the bottom of the tooth, compressive stress increases, causing the rim to deflect; see Figure 67b.

This finding lead to the design of a 3D segment of the tube, 5 mm thick and 5 mm high, which allowed the simulation of the joint formation region with minimal computational time. The modeled tube section includes a variable number of teeth, the carrier disc, and the four tools. The simulation model is also set up for torsion-free rotary swaging of the tube, so that rotation of the workpiece only occurs when the forming tools are open. Since the quality of the joining process and the resulting positioning accuracy of the integrated disc depend on the rim's penetration behavior into the teeth, a full model is used instead of a quarter or half model to avoid potential compromises in accuracy. Figure 68 illustrates the model setup and the motion kinematics of the tools.

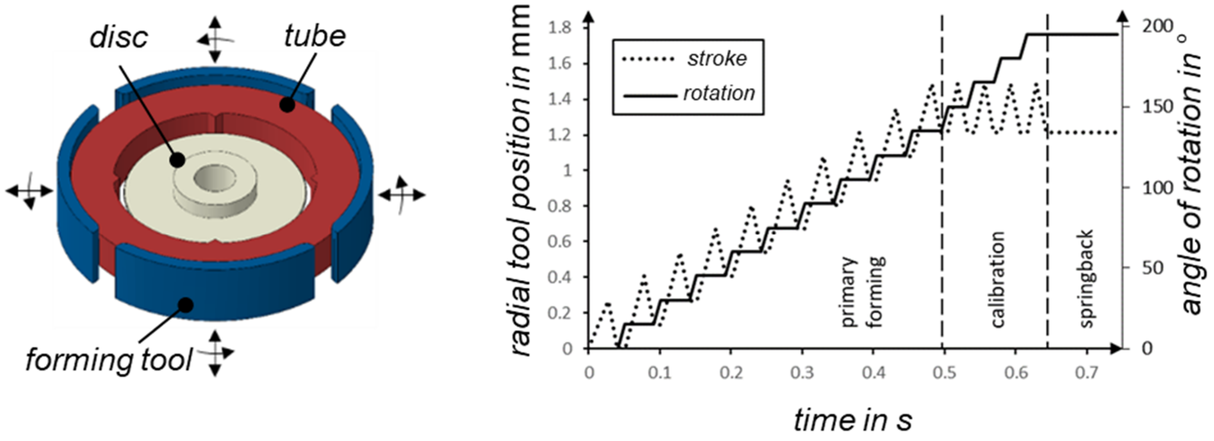

(a) **(b)**

Figure 68: Model setup for simulating (a) design parameters and (b) tool kinematics [O6].

As shown in Figure 68a, the tools strike the tube with the disc located inside and rotate after the strikes are released. The radial tool’s position and angle of rotation can be observed in Figure 68b. The process has only three stages. In the first forming stage, the tube’s diameter is decreased by 3 mm over the course of 10 forming strokes. To ensure uniform stress distribution between the disc and the tube, a sequence of four calibration strokes is performed without further diameter reduction. The initial boundary condition that held the disc in place is released during the springback step at the end of the forming process.

7.2.2 Investigating the effect of rim geometry

As demonstrated in Table 1, the influence of rim edge geometry is investigated by comparing two main variants: a chamfered and a non-chamfered rim edge. The non-chamfered variant has a contact area that is twice as large as that of the chamfered variant. Therefore, it is expected that a higher radial joining force will be required, and a lower penetration depth will be achieved in this case.

However, the evaluation of the penetration depth shows that the chamfered edge achieves only about 10% higher penetration depth (Figure 69a) and about 3% lower maximum radial stress (Figure 69b) compared to the non-chamfered edge. Nevertheless, a significant difference can be observed in the axial deflection behavior of the two rim geometries shown in Figure 69c.

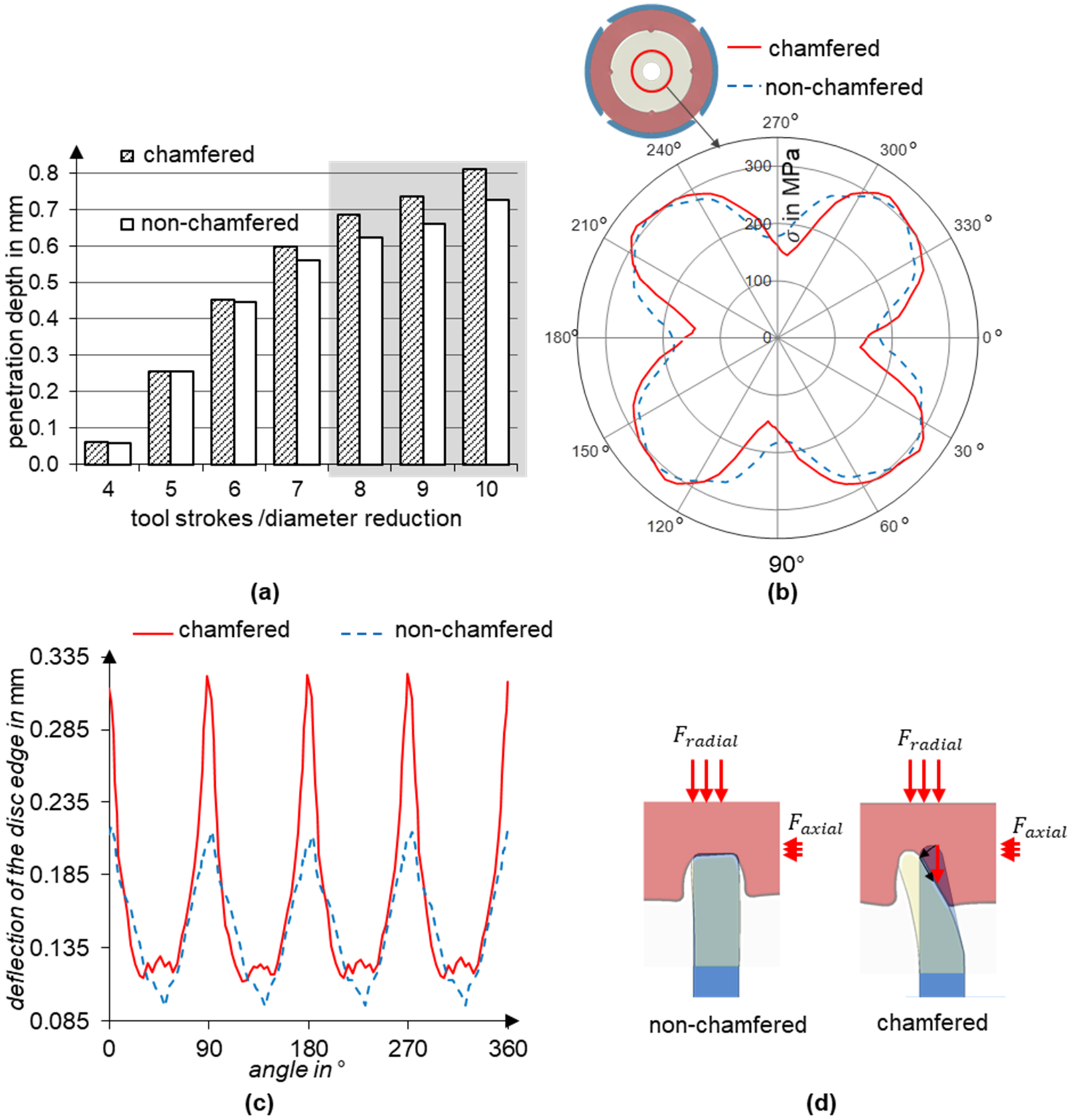

Figure 69: Effect of the rim edge geometry on the joining process (a) on penetration depth; (b) on the radial joining force. Evaluation of the axial edge deflection: (c) axial edge deflection over the whole disc circumference, and (d) visualization of the influence of the chamfer on the force distribution at the rim [O6].

As depicted in Figure 69c, both disc variations exhibit a wave-like axial deflection characterized by peaks at the teeth, a consequence of disc penetration. Notably, the chamfered variant displays considerably higher peaks. The elevated alternate rim deflection between toothed and non-toothed areas indicates a more substantial axial grip within the teeth for the chamfered disc. Both disc variations experience nearly identical radial and axial forces, where the radial force arises from radial forming tools, and the axial force results from material flow in the axial direction. However, the chamfered rim variant displays increased axial deflection due to its chamfered geometry, as illustrated in Figure 69d. Given the greater penetration depth and the consequent rise in alternate axial rim deflection, the subsequent investigations focus on the chamfered disc variant.

7.2.3 Investigating the effect of the number of teeth

Increasing the number of teeth obviously increases the contact area between the teeth and the disc, thereby increasing the required joining force and decreasing the achievable penetration depth. To investigate the effect of the number of teeth on joint formation, the number of teeth is varied between 4, 6, and 8 in the following tests. The chamfered edge disc is used in this variation. The simulation results show no significant differences in the depth of penetration of the disc, Figure 70a, or in the level of radial stress, Figure 70b.

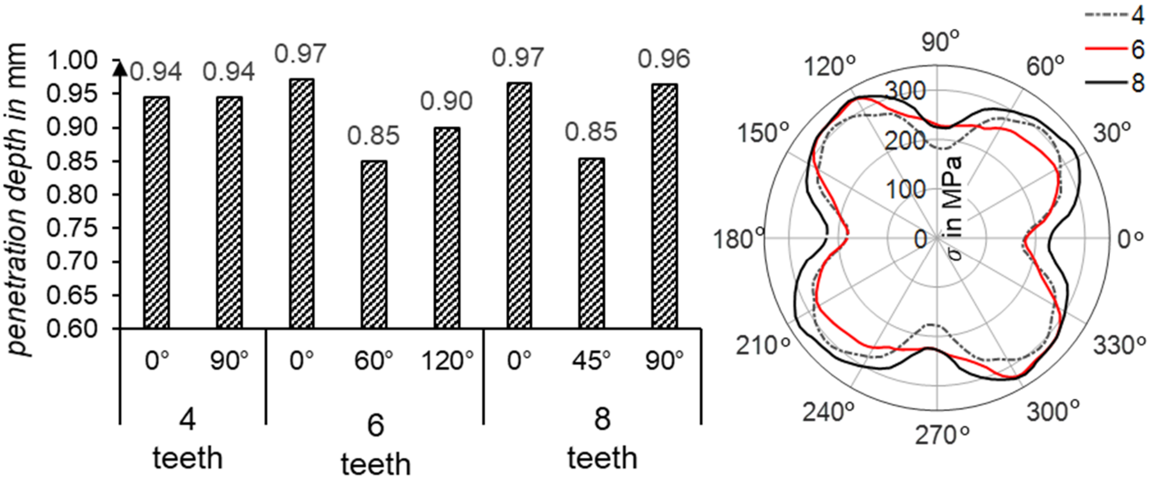

(a) (b)

Figure 70: Effect of the number of teeth on the joining process (a) on the penetration depth at the teeth, and (b) on the radial stress distribution at the disc [O6].

However, the results indicate that increasing the number of teeth appears to result in an unsymmetrical penetration of the disc into the teeth as well as an inhomogeneous distribution of radial stress on the disc. The radial stress distribution appears to have four distinct amplitudes regardless of the number of teeth. To clarify this behavior, both the disc penetration and the radial stress evolution during the rotary swaging process were analyzed.

The average penetration of all teeth (blue curve) and the deviation in tooth penetration (error bars) are shown in Figure 71a for the three cases. It can be observed that in the case of four teeth, there is a linear evolution of the disc penetration at almost the same level in all teeth. However, in the case of 6 and 8 teeth, the penetration becomes less linear and shows a significant deviation between the teeth. This deviation is even more pronounced in the case of 6 teeth, and the progression of the penetration appears to be more non-linear.

The reason for this behavior has been identified as radial force propagation from the tools into the tube during the rotary swaging process. Since only four oscillating tools are hitting the tube at a time, some of the teeth are outside the path of the acting radial force. At this point, the tube material begins to flow into the unstressed gap between the tools, releasing the previously applied radial stress. Figure 71b illustrates the material flow at three teeth for the case of 8 teeth during one forming increment.

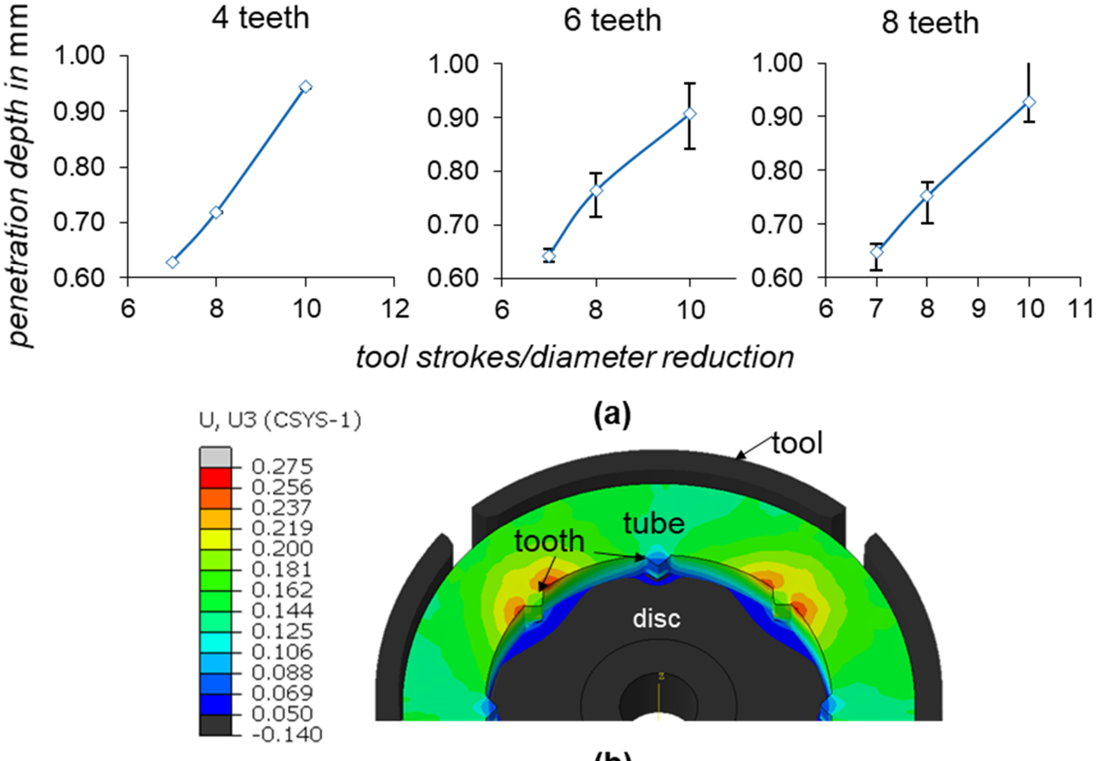

(a)

(b)

Figure 71: Formation of the joint during tube rotary swaging: (a) disc penetration in the last three increments for each variation; and (b) axial material flow at the teeth during the swaging process [O6].

As can be seen in Figure 71b, the axial material flow, represented by the U3 component in the simulation, is noticeably higher on the teeth between the gaps than on the other two teeth in the loading area of the tools. This alternating reduction of the previously established radial stress by incremental tool impact and workpiece rotation explains why the resulting stress distribution follows the same pattern regardless of the tooth variant.

Although this typically has less effect on the roundness and surface finish of rotary swaging parts, it does introduce a bias in the radial stress generated between the disc and die. To mitigate this problem, the teeth should ideally be arranged to remain within the effective tool area despite the tool rotation.

7.2.4 Experimental investigations

Preliminary trials

To pre-teeth the tube, a mandrel with toothed cavities is inserted into the tube during rotary swaging. As rotary swaging proceeds, the material flows into these cavities, forming the internal teeth. For experimental validation, the tube is pre-toothed with 8 teeth to enhance radial stress with a more uniform stress disturbance, as opposed to using 6 teeth, as shown Figure 71a. Figure 72 displays a cross-section of the resultant tooth geometry.

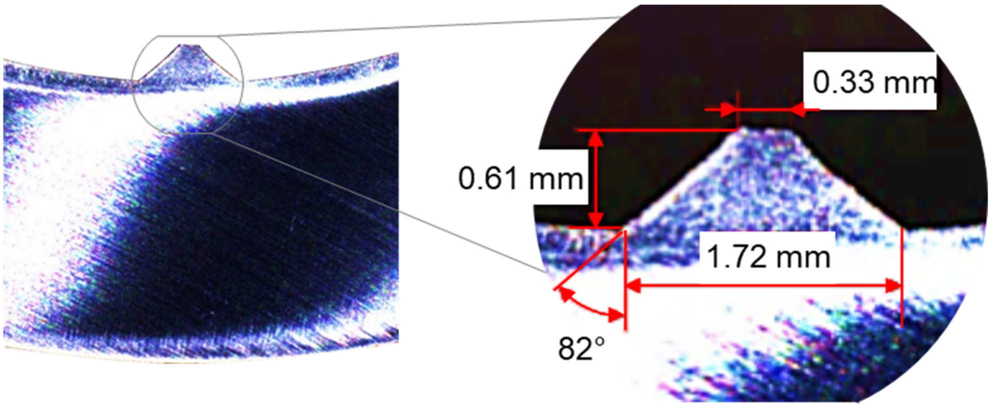

Figure 72: Cross section of pre-formed tooth geometry [O6].

After toothing the tube, discs are mounted on a mandrel and positioned within the pre-toothed section. The tube diameter is then reduced by infeed rotary swaging, causing the disc to join inside the tube. To enable movement after the initial disc penetration and prevent excessive rim deflection, the mandrel used to hold the disc is allowed to move axially. To achieve this, the mandrel is guided axially by the clamping fixture and preloaded by a spring to prevent any movement prior to penetration, as shown in Figure 74a. Finally, the quality of the joint is visually evaluated using metallographic cross sections. Both the penetration depth and the deflection of the disc are evaluated as characteristics of the form- and force-fit joint. To prevent springback during cutting, specimens are fully embedded in resin. Figure 73a shows an example of two successfully joined discs at a distance of 80 mm. As can be seen in the cross-section image in Figure 73b, the disc undergoes a deflection of 1.1 mm and a penetration depth of 0.35 mm.

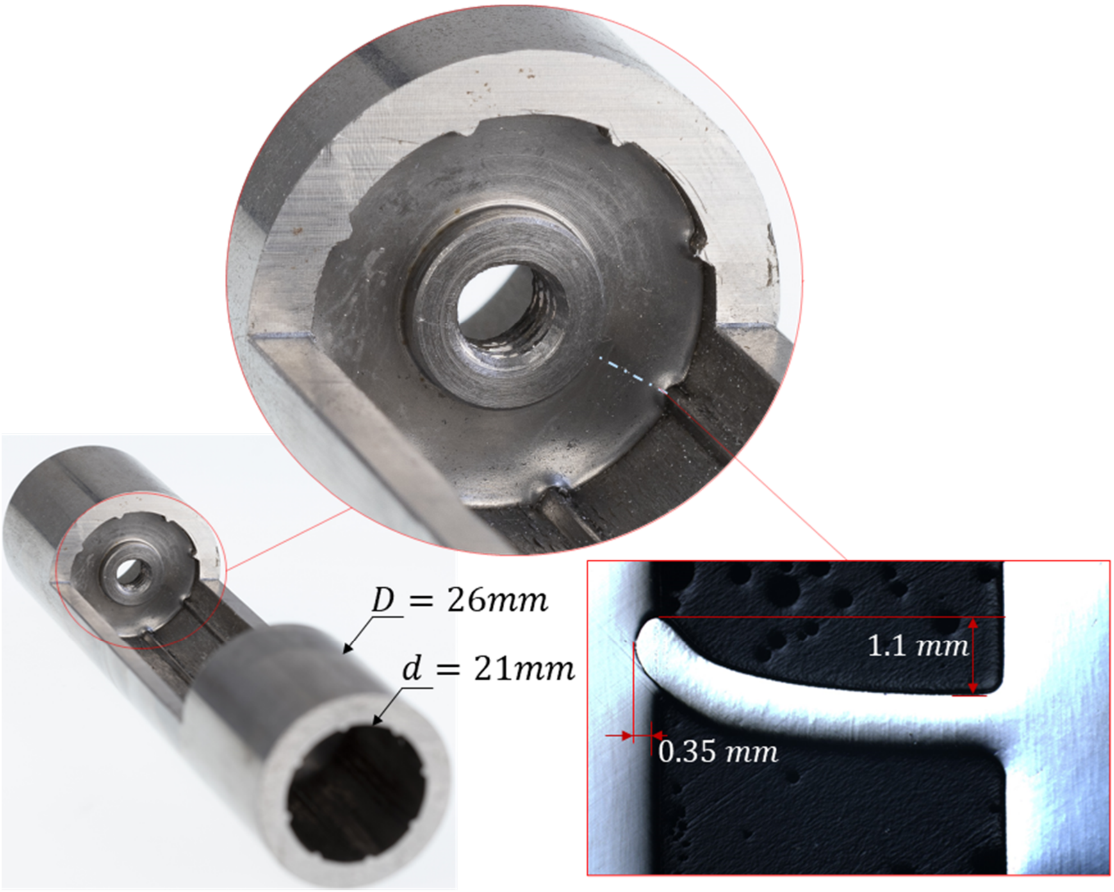

(a) (b)

Figure 73: Successful disc integration. (a) Integrated disc inside the tube and (b) deformation behavior compared to the simulation [O6].

Evaluation of the positioning accuracy of the two discs, integrated with a specified distance of 80 mm to each other, resulted in a distance of 79.6 mm. Additionally, a total disc tilt of 0.8° with respect to each other is observed after joining [S6].

Sensor integration

After successfully integrating the discs into the tube, as shown in Figure 73, the sensor components were adhesively bonded onto the discs. The sensor is designed to measure only in-plane displacement caused by torsional and bending loads. To enhance robustness against disc deformation, the diameter of the disc core is increased from 10 mm to 15 mm in comparison to the previous investigation. After pre-toothing the tube, the discs with the mounted sensor components were screwed to a mandrel and positioned inside the tube. During subsequent diameter reduction by recess rotary swaging, the two discs with the sensor components were sequentially integrated. Figure 74a and 74b demonstrate the integration process. Figure 74a shows how excessive disc deflection caused by axial material flow is prevented by allowing the disc to move axially. Figure 74c illustrates a successfully integrated sensor inside the tube. The lens tube shown here refers to the system design where the lens is mounted directly behind the photomask to focus the pattern image onto the image sensor. All components, LED, photomask, and lens are then assembled into a tube called the lens tube.

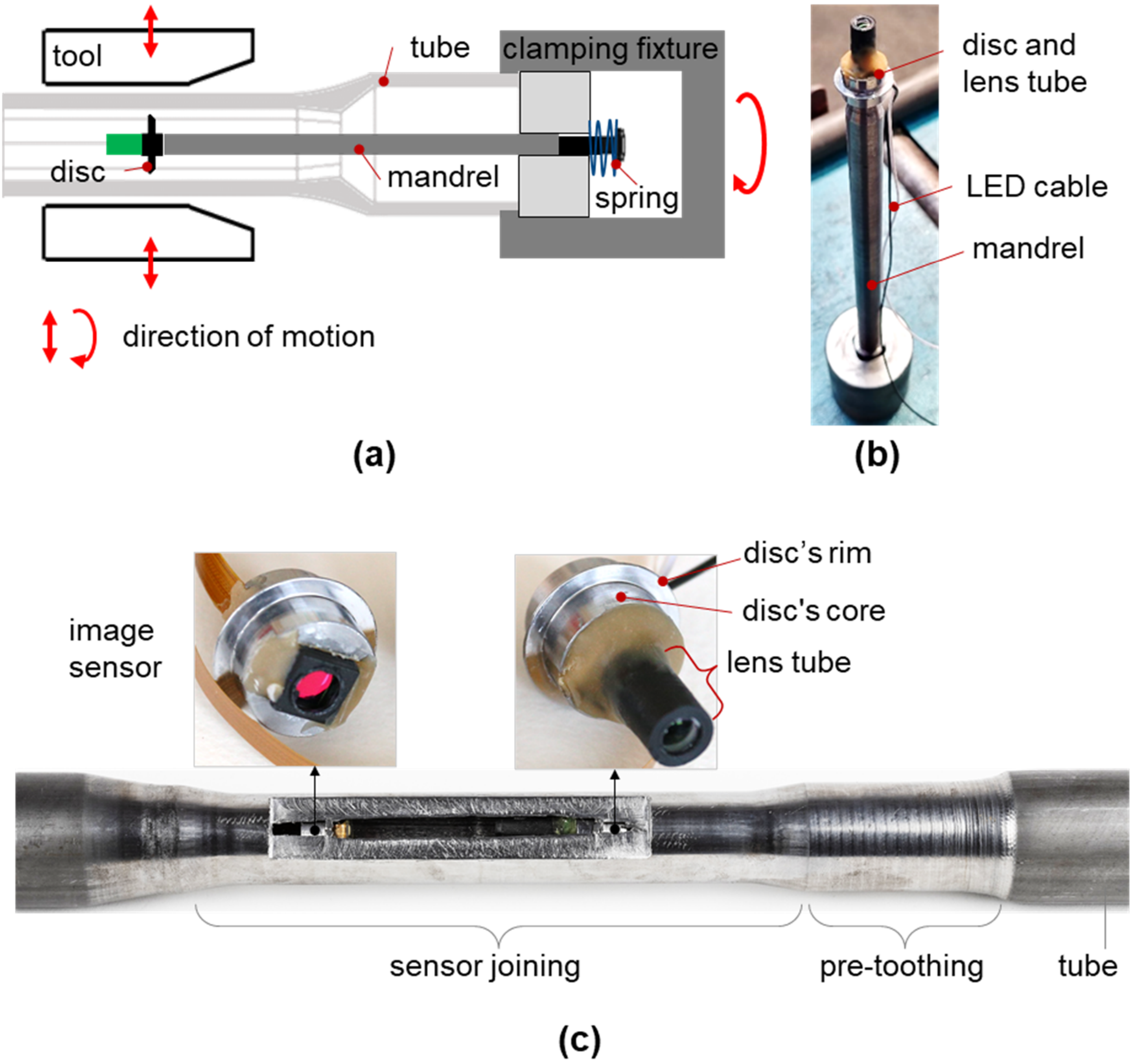

Figure 74: Sensor integration into the tube through recess rotary swaging. (a) Visualizing the joining process; (b) photo of the sensor-carrying disc screwed to the mandrel [O6]; (c) both sensor components integrated into the tube.

Non-destructive evaluation of the joint quality

The sensor tube is undergoing a non-destructive evaluation of the quality of the joint. The tube is subjected to static bending and torsional loading on testing machines, where the loads are both detected by the integrated sensor and by the testing machine sensors. Inadequate joint quality would result in hysteretic behavior or in a zero-point shift in the sensor signal. The tube is stepwise loaded, with a bending force of 1500 N, and a torsional load of 300 Nm is detected by the integrated sensor. During the bending test, the load is applied at the midpoint between the two integrated discs. Figure 75 shows the achieved results.

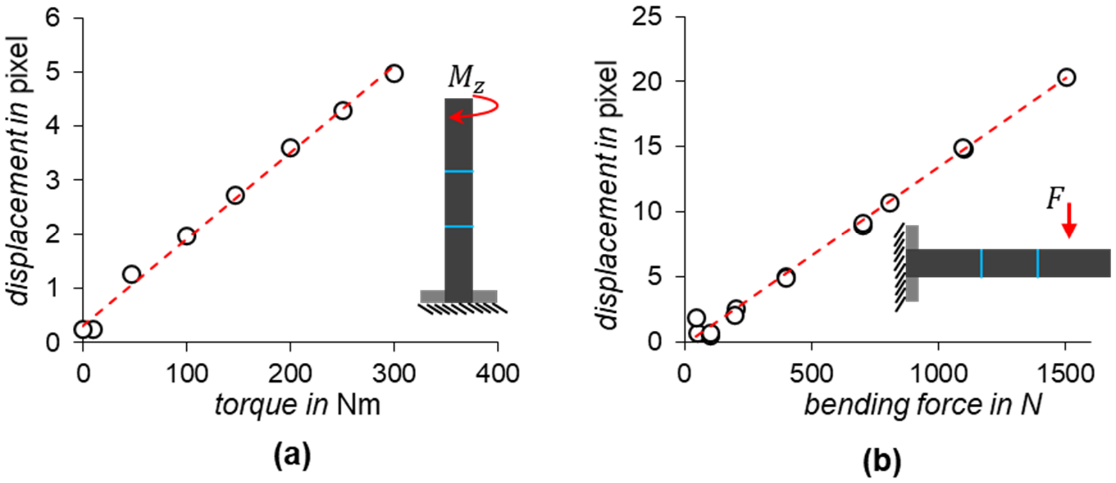

Figure 75: Sensor behavior under (a) torsional load and (b) bending load [O6].

As can be seen in Figure 75, both sensor signals show hysteresis-free and zero-point stable behavior, confirming a successful integration.

8 Conclusion and Future Work

8.1 Conclusion

In the context of Industry 4.0, automated processes require a greater focus on data collection to control forces and moments in various manufacturing processes. Measuring process forces and moments facilitates not only the implementation of control strategies but also increases the accuracy of detecting specific product characteristics. Moreover, sensors are increasingly utilized in the implementation of digital approaches, such as structural health monitoring or predictive maintenance. Limited accessibility, error-prone measurement locations, or harsh environments typically prevent the use of external sensors for the accurate measurement of load conditions in manufacturing machines or mechanical structures.

Integrating sensors into mechanical components and machines enables direct load measurement on the host structures while preserving their mechanical functionality. In recent research, various processes have been investigated to integrate electromechanical transducers, such as strain gauge-based or piezoelectric transducers, into passive metallic structures. In particular, joining by forming technologies have shown significant capability for damage-free and controlled sensor integration. However, the design requirements for electromechanical sensors in the joining process have restricted the sensor structures created by forming technology to the measurement of uniaxial or biaxial force or torque. Additionally, the high cost of sensor components results in expensive sensor structures and machine elements. As a result, despite their major potential, the widespread implementation of these sensor components has not been accomplished.

This thesis presents the principles for the creation of multiaxial sensor load-bearing structures and machine elements based on a simple, optical, non-contact, image-based measurement concept. The introduced measurement concept for high-resolution multiaxial measurement of resulting structural deflection under load demonstrates the potential to overcome existing limitations in the creation of sensor structures and machine components.

Furthermore, the design parameters for determining the target measurement resolution and a comprehensive sensor configuration strategy were presented. Although the analytical approach demonstrated feasibility in determining load components, its high sensitivity to sensor assembly deviations and the need for precise determination of the center of rotation represents a significant drawback. To overcome this shortcoming, a DTR algorithm with pre-calculated displacements has shown considerable potential for recognizing sensor behavior and accurately identifying load components. In addition to the adjustable measurement length and optical magnification, it was also shown that the image quality significantly improves the measurement resolution.

Through experimental evaluation using diverse prototypes, the concept demonstrates its ability to accurately detect multi-axis loads from a single image capture. The DTR algorithm allowed for an increase in measurement axes from four to six in cases where a nonlinear relationship between bending forces and bending moments occurred.

The sensor evaluation under industrial-related conditions using the sensor bending roll shows exceptional measurement resolution for the applied bending forces in both directions and magnitude, reaching the nanometer range. These findings were confirmed by the sensor validation using the guidance column. Here, the results show that the high-resolution measurement of the guidance column deflection in a blanking tool offers new possibilities for the detection of small tool misalignments. This allows for new approaches to detecting anomalies, especially in scenarios involving repeated tool installations with non-exact clamping conditions, as Kraus et al. showed the direct effect of different tool clamping conditions on tool vibration [KRA17].

The investigations on sensor integration by rotary swaging have demonstrated the possibility of integrating highly sensitive optical sensors with the high positioning accuracy required using rotary swaging. The investigations have demonstrated the possibilities offered by appropriate design of the joining parameters and the joining process. In addition, it has been shown that the number of tools and the contact area during rotary swaging have a direct effect on the distribution of radial stresses in the integrated disc. When a tooth is located in the gap between the tools during a forming increment, the axial material flow at that point results in a partial reduction of the previously generated radial stress. As the tube rotates and the gap between the teeth changes, non-linear radial stress is imposed that increases with the depth of penetration. Successful disc integration was achieved by allowing axial displacement of the disc after the initial penetration and applying recess rotary swaging. Given the appropriate process design, a successfully integrated sensor for measuring bending force and torque shows full functionality with no hysteretic sensory behavior. Integrating the original sensor design, including built-in mirrors to measure changes in measuring length under axial load, was not feasible due to perceived process variations. As discussed in [O6] and [O7], the high accuracy required for sensor integration through forming can be achieved using flexible forming machines, such as the 3DSP [GRO17b]. However, this may result in a complex process design, conflicting with the goal of cost-effective production of sensor-bearing structures and machine elements.

8.2 Future Work

A potential solution is to enhance sensor robustness by modifying the sensor design in a way that eliminates mirroring of the critical beam path, for example, by tilting the beam path and adding another image sensor for axial load detection. Figure 76b shows this approach compared to the initial sensor design, shown in Figure 76a.

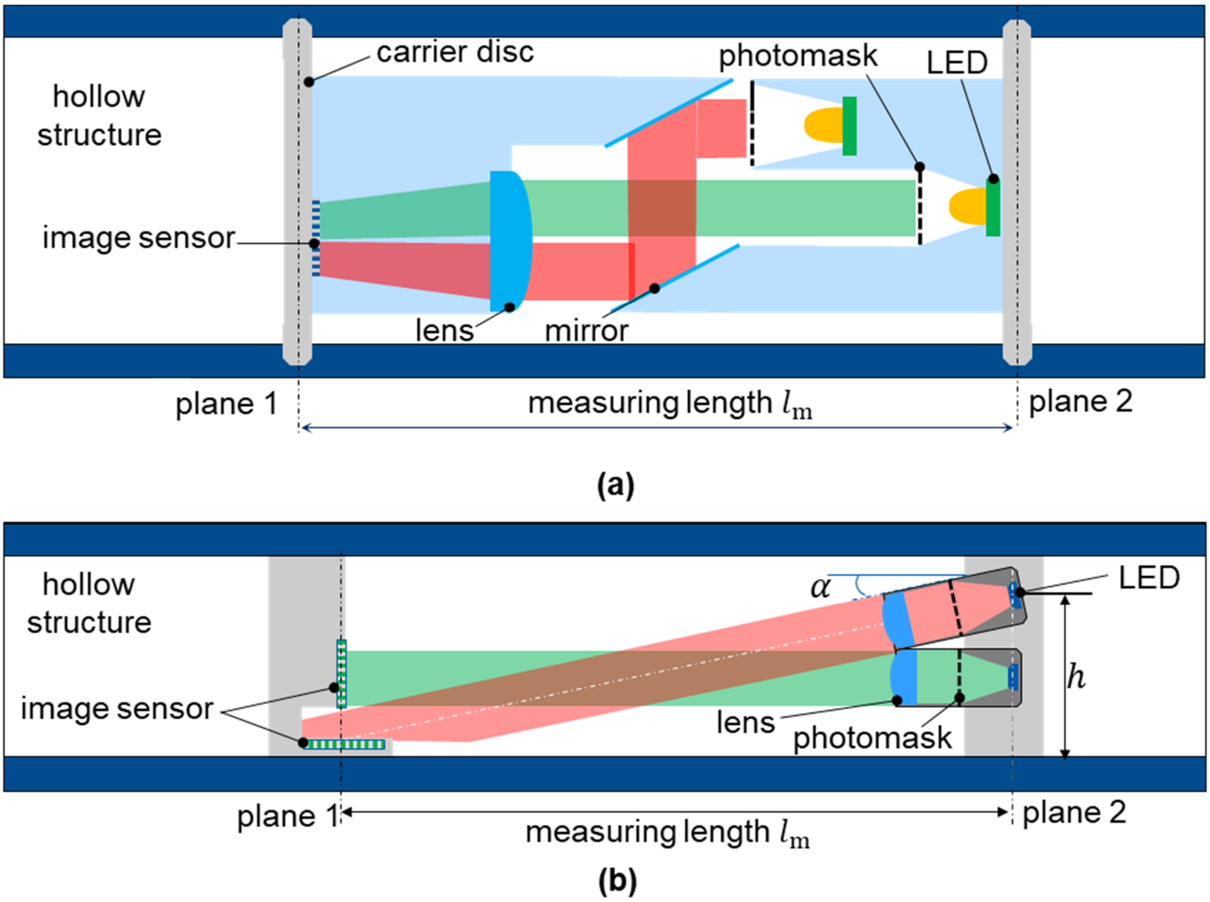

(a)

(b)

Figure 76: Sensor design to increase sensor robustness during assembly

As can be seen in Figure 76b, the red beam is tilted at angle α and reaches the horizontally mounted image sensor. The tilt angle is given in relation to the measurement length l_m and the sensor height h, which is proportional to the inner diameter of the structure, as follows:

$$\alpha = \arctan\left(\frac{h}{l_m}\right) \tag{29}$$

Higher angle results in better image quality, would require however, larger system height or inner diameter. In this case a focusing lens on the side of the photomask is recommended, to sharply adjust the image quality at the image sensor. Furthermore, the flexible photomask design facilitates a reduction in image distortion, e.g. targeted application of image correction algorithms, such as the use of vertical edge detection for tilt correction, as shown in [ALG08]. The different colors of the light paths ensure that each image sensor captures only the light path assigned to it.

In addition to the achievable measurement resolution, which was a particular focus of this work, a key aspect of any sensor is its measurement accuracy. Similar to strain gauge-based sensors, the accuracy depends on several factors such as the calibration process and the performance of the electronics used. However, for image-based sensors, the image processing algorithms play a significant role in achieving high measurement accuracy. This is linked to achieving illumination stability over the sensor's operating time to ensure constant image quality and, in turn, accurate image processing.

The highly sensitive detection of slight guidance deflection in blanking tools offers the potential for real-time identification and correction of any tool misalignment during installation. Assuming that the ram guidance system overtakes the tool guidance right after tool clamping within the machine raises questions about the role of tool guidance both during the installation and operation phases and about the potential for size optimization of the currently oversized tool guidance systems.

List of Figures

Figure 1: Illustration of the Rotary Swaging Unit [ISH19] 7
Figure 2: Influence of the rotation per stroke αH on the resulting angle of twist according to [RAT07] 8
Figure 3: Basic types of elastic elements in strain gauge force/torque sensors based on the load-induced stress according to [GEV06]. 9
Figure 4: Design of a strain gauge-based six-axis force/torque sensor [AHM21]. 10
Figure 5: Optical intensity based multiaxial force sensors. (a) The deformation of the internally reflecting rubber hemisphere results in a different intensity pattern in the photodiodes [TAR11]; (b) as the distance between the mirrors and the optical fibers changes, the intensity of the reflected light changes proportionally [XIE12]; and (c) changing the distance between the fiber tip and the respective mirror results in changes in the intensity of the light detected by the photodiodes [ALM17] 12
Figure 6: Multiaxial load conditions borne by fasteners in a wind turbine tower [LI23]. 13
Figure 7: Multiaxial sensor bolts that function (a) by external attachment of strain gauge films on an M72 Bolt [SCH21]; (b) by screwing a strain gauge sensor inside an M20 bolt [HER22]; and c) by the integration of a laser source and a prism rod into the bolt [WOL23]. 14
Figure 8: Visualization of the camera assembly according to [PRO23]. 15
Figure 9: Definition of the focal length in a spherically curved interface according to [DEM09]. 16
Figure 10: Determining the focal length in thin and thick lenses, according to [DEM09]. 16
Figure 11: Three-lens zoom lens system [MOU97]. 17
Figure 12: Adjusting the optical magnification in a three-lens zoom system, according to [S1]. 18

Figure 13: Effects of aberrations on the incoming rays from an object on the image plane. Spherical and comatic aberration [LIN17], astigmatism [WRI17],

curvature of field [LIN17], distortion [PAR09] and longitudinal and lateral chromatic aberration [GOH21]. 20
Figure 14: Simulation of optical systems: (a) ray tracing of two field points and (b) the associated spot diagram [GRO05]. 22
Figure 15: Use of the photomask for background schlieren techniques (a), system design according to [SUN14], and (b) a photomask consisting of predefined circles on a black background. 23
Figure 16: Cross-sectional view of an image sensor [NAK05]. 24
Figure 17: Capturing colored images using a color filter, according to [PAR22]. 24
Figure 18: Structure and signal transmission in image sensors: CCD sensor (left) and CMOS sensor (right) [OHT20]. 25
Figure 19: Visualization of the working principles of DIC: (a) set-up for strain analysis [ZHA19b], (b) correlation process for a subset of one pixel, and (c) the resulting correlation matrix [LEM08]. 28
Figure 20: CNN network structure for image classification [ALZ21]. 30
Figure 21: Structure of a decision tree algorithm [HAF21]. 31
Figure 22: Create virtual training images by recombining real training images [DUB19]. 32
Figure 23: Visualization of the influence of the inner hole diameter on the structure stiffness 34
Figure 24: Schematic of optical image-based multiaxial load detection within a hollow structure (left) and visualized plane displacements in ($\Delta z, \Delta y$, and θx). 38
Figure 25: Comparison of the feature contrast achieved by the methods of spin coating, airbrush, and back-illuminated photomask patterning [S3]. 40
Figure 26: Schematic illustration of the optical image-based multiaxial structure-integrated load measurement [O3]. 41
Figure 27: Visualization of the photomasks' pattern projection onto the image sensor where the pattern has only two points. 42
Figure 28: Visualization of the crosstalk behavior of in-plane displacements φ and δxy on the out-of-plane displacements $\Delta P3{,}4$ [O3] 44
Figure 29: Influence of an inclined border line between the two beams on the determination of the crosstalk behavior [O3]. 45

Figure 30: A one-sided clamped hollow tube for detection of local strains and relative plane displacements under different load components....................... 48

Figure 31: Visualization of the measuring resolution in image-based displacement measuring. 51

Figure 32: Deterioration of pattern imaging sharpness caused by increasing the optical magnification 53

Figure 33: Displacement measuring range as a function of sensor area, optical gain, and maximum structure elongation and deflection under load. 54

Figure 34: Iterative setting of the optical magnification and measuring length in the sensor design. 56

Figure 35: Resulting feature sharpness in the color channels......................... 58

Figure 36: Key parameters for DIC and required processing time. (a) Visualization of the parameters and processing time for the two DIC algorithms NCC and NSSD; (b) as a function of the subset size; and (c) as a function of the search field size; (d) a logarithmic curve of the processing time as a function of the subpixel size according to [S2]. 59

Figure 37: CNN network structure for determining displacements by number positions in the decimal number system according to [MA21] and [S4]. 61

Figure 38: Displacement determination process according to [MA21]. 62

Figure 39: Prediction accuracy and time cost as functions of the number of fully connected layers according to [S4]. 63

Figure 40: Evaluating the multiaxial load detection: (a) test bench design and (b) sensor prototype [O3]. 65

Figure 41: Photomask design [O3] 66

Figure 42: Results of uniaxial loading test [O3] 67

Figure 43: Characterization of the crosstalk behavior: a) determined angle ∅ of the border line; b) determined crosstalk between δx and $P3{,}4\_x$ for uniaxial (Fx) and biaxial (Fxy) loading; c) determined crosstalk between δy and $P3{,}4\_y$ for uniaxial (Fy) and biaxial (Fxy) loading; d) crosstalk of the twist angle φ on the mirrored image segment [O3]. 69

Figure 44: Determination of the centers of rotation for the direct and mirrored image segments by mere torsional load (a) for the direct image segment and (b) for the mirrored image segment [O3]. 70

Figure 45: Calculated displacement components (δx, δy, φ) when the structure is under multiaxial loading with ($Fx + Fy + Mz$) [O3]. 71
Figure 46: Determined displacement components (δx, δy, φ, Δlm) when the structure is multiaxially loaded with ($Fx + Fy + Fz + Mz$) [O3]. 73
Figure 47**:** Correlation of bending moments to bending forces in both load cases (a) for $Fx + Fy + Mz$ and (b) for $Fx + Fy + Fz + Mz$. 75
Figure 48: (a) modified sensor design and (b) test bench for multiaxial loading of the sensor [O4]. 78
Figure 49: Results of uniaxial loads [O4]. 79
Figure 50: Image pre-processing for the CNN model [S5]. 80
Figure 51: Load determination using a decision tree regressor. 81
Figure 52: Results of machine learning-based load prediction according to [S5]: (a) and (b) for the bending forces, (c) and (d) for the bending moments, (e) for the axial force, and (f) showing the non-linear relationship between the applied bending force and bending moments. 82
Figure 53: (a) Illustration of bending-linear flow splitting process [GRO18] and (b) the bending roll with its dimensions 85
Figure 54: Sensor installation inside the pin of the bending roll [O5]. 85
Figure 55: Visualization of the displacement of the measuring plane according to the clamping situation [O5]. 86
Figure 56: Determination of the influence of the clamping situation on the measurement resolution (a) experimental setup [O5] and (b) visualization of the variation of the clamping force by the bolt clamping torque. 87
Figure 57: Results of the experimental investigation into the influence of the clamping situation on the pin deformation behavior. Curves of the integrated and external laser sensor according to [O5] (a) and correlation between both sensors at a clamping torque of 25 Nm (b). 88
Figure 58: Experimental setup for in-situ sensor roll calibration. (a) Bending roll assembly; (b) schematic illustration, and (c) picture of the calibration setup 90
Figure 59: Results of the in-situ bending roll calibration for Fx (a) and for Fy (b). 91
Figure 60: Measurement of bending forces during profile bending at different roll infeed positions: (a) schematic of the bending process; (b) bending forces for an infeed position of 20 mm according to [O5]; and (c) for 50 mm 92

Figure 61: Blanking tool setup in a BRUDERER stamping press according to [MOL22]. 93
Figure 62: Sensor installation inside the guidance column 94
Figure 63: Assembly of the sensor guidance column within the blanking tool. Column bending moment My induced by the tilt on the right side of the upper plate during the vertical plate motion along the column 95
Figure 64: Curves of column deflection under all tilt variations. (a) averaged curves of all variations for right (top) and left (bottom). Curves of the three repetitions, including the average curve for a tilt to the right of $\gamma = 0.001614°$ in (b) and of $\gamma = 0.1614°$ in (c) 97
Figure 65: Visualization of a possible process design for sensor integration by rotary swaging. 99
Figure 66: Joining partner and joining process design approach [O1]. 101
Figure 67: Preliminary simulation and basic model parameters: (a) simulation parameter settings and (b) achieved disc penetration behavior [O6]. 103
Figure 68: Model setup for simulating (a) design parameters and (b) tool kinematics [O6]. 104
Figure 69: Effect of the rim edge geometry on the joining process (a) on penetration depth; (b) on the radial joining force. Evaluation of the axial edge deflection: (c) axial edge deflection over the whole disc circumference, and (d) visualization of the influence of the chamfer on the force distribution at the rim [O6]. 105
Figure 70: Effect of the number of teeth on the joining process (a) on the penetration depth at the teeth, and (b) on the radial stress distribution at the disc [O6]. 106
Figure 71: Formation of the joint during tube rotary swaging: (a) disc penetration in the last three increments for each variation; and (b) axial material flow at the teeth during the swaging process [O6]. 107
Figure 72: Cross section of pre-formed tooth geometry [O6]. 108
Figure 73: Successful disc integration. (a) Integrated disc inside the tube and (b) deformation behavior compared to the simulation [O6]. 109
Figure 74: Sensor integration into the tube through recess rotary swaging. (a) Visualizing the joining process; (b) photo of the sensor-carrying disc screwed to the mandrel [O6]; (c) both sensor components integrated into the tube. 111

Figure 75: Sensor behavior under (a) torsional load and (b) 3-point bending load [O6]. 112
Figure 76: Sensor design to increase sensor robustness during assembly .. 116

References

Own publications

[O1] Al-Baradoni, N. ; Groche, P.: Sensor-integrated structures in mechanical engineering: challenges and opportunities for mechanical joining processes. In: *Production Engineering* Bd. 16 (2022), Nr. 2–3, S. 423–434 — ISBN 0123456789

[O2] Al-Baradoni, N. ; Krech, M. ; Groche, P.: In-process calibration of smart structures produced by incremental forming. In: *Production Engineering* (2020)

[O3] Al-Baradoni, N. ; Groche, P.: Sensor integrated load-bearing structures: Measuring axis extension with dic-based transducers. In: *Sensors* Bd. 21, Multidisciplinary Digital Publishing Institute (2021)

[O4] Al-Baradoni, N. ; Groche, P.: Identification of the sensory properties of image-based multi-axis force/torque sensors. In: *Sensors and Measuring Systems*; 21th ITG/GMA-Symposium, 2022

[O5] Al-Baradoni, N. ; Thoma, C. ; Depta, B. ; Groche, P.: Image-based, structure-integrated sensor for measuring multiaxial deflection in stiff machine elements. In: *https://doi.org/10.1117/12.2657659*. Bd. 12486 : SPIE, 2023 — ISBN 9781510660793

[O6] Al-Baradoni, N. ; Heck, P. ; Groche, · P.: High-Precision Integration of Optical Sensors into Metallic Tubes Using Rotary Swaging: Process Phenomena in the Joint Formation. Preprints 2024, 2024021329. https://doi.org/10.20944/preprints202402.1329.v1

[O7] Al-Baradoni, N. ; Groche, P.: Integration of optical sensors into load-bearing structures: Opportunities and challenges. In: *ForTech Bulk 2022 : Forming Technology Network Bulk 2022, 18. - 19. Mai 2022*. Stuttgart : Universität Stuttgart, Institut für Umformtechnik, 2022 — ISBN 978-3-946818-19-9

Student works supervised by the author

[S1] MALICEVIC, K.: Development of a camera-based multi-axis force/torque sensor with specifically configured sensory chracteristics German Tiltel: Entwicklung eines kamerabasierten, mehrachsigen Kraft-/ Drehmomentensensors mit gezielt konfigurierten sensorischen Eigenschaften. Master Thesis, Technical University of Darmstadt, 2022.

[S2] WINTER, S.: Development and validation of a test environment for image acquisition and processing in optical deformation measurement. German Titel: Entwicklung und Validierung einer Testumgebung zur Bilderfassung und -verarbeitung bei optischer Verformungsmessung, Master Thesis, Technical University of Darmstadt, 2019.

[S3] SIEGEL, M.: Optimization of the sensory properties of optically based sensory structures for force and torque measurement. German Titel: Optimierung der sensorischen Eigenschaften optisch basierter sensorischer Strukturen zur Kraft und Drehmomentmessung. Master Thesis, Technical University of Darmstadt, 2020.

[S4] ZHANG, B. ; BIALEK, F. ; ROMEIS, J. ; COBO, J. ; WILLE, A.: Investigation of the Use of Neural Networks for image analysis and classification for camera-based force/torque /torque sensors, German Titel: Untersuchung des Einsatzes von neuronalen Netzen zur Bildauswertung und Lastenklassifikation bei kamerabasierter Kraft-/Drehmomentsensoren. Advanced Design Project, Technical University of Darmstadt, 2021.

[S5] ZHANG, Y.: Development of an AI-based algorithm for image processing in camera-based force/torque sensor. German Titel: Entwicklung eines KI-basierten Algorithmus zur Bildauswertung bei kamerabasierten Kraft-/Drehmomentsensoren. Master Thesis, Technical University of Darmstadt, 2022.

[S6] HECK, P.: Process design for position-controlled integration of optical sensors in tubular structures. German Titel: Prozessauslegung zur lagegeregelten Integration optischer Sensoren in rohrförmige Strukturen. Master Thesis, Technical University of Darmstadt, 2023.

Further references

[ABS21] ABSPOEL, M. ; ESCUDERO, D. ; VOLGUSHEV, N.: Secure training of decision trees with continuous attributes. In: *Proceedings on Privacy Enhancing Technologies* Bd. 2021

[AHM21] AHMAD, A. ; WYNN, T. ; LIN, C.: A comprehensive design of six-axis force/moment sensor. In: *Sensors* Bd. 21, Multidisciplinary Digital Publishing Institute (2021)

[AKB18] AKBARI, H. ; KAZEROONI, A.: Improving the coupling errors of a Maltese cross-beams type six-axis force/moment sensor using numerical shape-optimization technique. In: *Measurement* Bd. 126, Elsevier (2018)

[ALG08] AL-GHAILI, A. ; MASHOHOR, S. ; ISMAIL, A. ; RAMLI, A.: A new vertical edge detection algorithm and its application. In: *2008 International Conference on Computer Engineering and Systems, ICCES 2008*, 2008 — ISBN 9781424421152

[ALM17] AL-MAI, O. ; AHMADI, M. ; ALBERT, J.: A Compliant 3-Axis Fiber-Optic Force Sensor for Biomechanical Measurement. In: *IEEE Sensors Journal* (2017)

[ALM18] AL-MAI, O. ; AHMADI, M. ; ALBERT, J.: Design, Development and Calibration of a Lightweight, Compliant Six-Axis Optical Force/Torque Sensor. In: *IEEE Sensors Journal* (2018)

[ALZ21] ALZUBAIDI, L. ; ZHANG, J. ; HUMAIDI, A. ; AL-DUJAILI, A. ; DUAN, Y. ; AL-SHAMMA, O. ; SANTAMARÍA, J. ; FADHEL, M. ; AL-AMIDIE, M. ; FARHAN, L.: Review of deep learning: concepts, CNN architectures, challenges, applications, future directions. In: *Journal of Big Data* Bd. 8, SpringerOpen (2021)

[AND12] ANDERL, R. ; EIGNER, M. ; SENDLER, U. ; STARK, R.: *Smart engineering: interdisziplinäre Produktentstehung* : Springer-Verlag, 2012 — ISBN 3642293719, 9783642293719

[BER12] BERKOVIC, G. ; SHAFIR, E.: Optical methods for distance and displacement measurements. In: *Advances in Optics and Photonics* (2012)

[BIL21] BILLESCHOU, P. ; ALBERTSEN, C. ; LARSEN, J. ; MANOONPONG, P.: A Low-Cost, Compact, Sealed, Three-Axis Force/Torque Sensor for Walking Robots. In: *IEEE Sensors Journal* Bd. 21, Institute of Electrical and Electronics Engineers Inc. (2021)

[BLA21] BLAHNIK, V. ; SCHINDELBECK, O.: Smartphone imaging technology and its applications. In: *Advanced Optical Technologies* Bd. 10, De Gruyter Open Ltd (2021)

[BOR17] BORNERT, M. ; DOUMALIN, P. ; DUPRÉ, J. ; POILANE, C. ; ROBERT, L. ; TOUSSAINT, E. ; WATTRISSE, B.: Shortcut in DIC error assessment induced by image interpolation used for subpixel shifting. In: *Optics and Lasers in Engineering* Bd. 91, Elsevier (2017)

[BRU89] BRUCK, H. ; MCNEILL, S. ; SUTTON, M. ; PETERS, W.: Digital image correlation using Newton-Raphson method of partial differential correction. In: *Experimental Mechanics* Bd. 29, Kluwer Academic Publishers (1989)

[CAL17] CALMANO, S.: *Methodik zur Regelung von Bauteileigenschaften in Umformprozessen*, Dissertation, Technical Univeristy of Darmstadt, 2017, Shaker Verlag— ISBN 3844054448

[CAN17] CANALES, C. ; BUSSETTA, P. ; PONTHOT, J.: On the numerical simulation of sheet metal blanking process. In: *International Journal of Material Forming* Bd. 10, Springer-Verlag France (2017)

[CAV19] CAVILLON, M. ; LANCRY, M. ; POUMELLEC, B. ; WANG, Y. ; CANNING, J. ; COOK, K. ; HAWKINS, T. ; DRAGIC, P. ; BALLATO, J.: Overview of high temperature fibre Bragg gratings and potential improvement using highly doped aluminosilicate glass optical fibres. In: *JPhys Photonics* Bd. 1 (2019)

[CHE02] CHENG, P. ; SUTTON, M. ; SCHREIER, H. ; MCNEILL, S.: Full-field speckle pattern image correlation with B-Spline deformation function. In: *Experimental Mechanics* Bd. 42, Springer (2002)

[CHE21] CHENG, H. ; CAO, Y. ; LI, H.: Preliminary design of a three-element zoom system based on a variable-focal-power lens. In: *Optical Review* Bd. 28, Springer Japan (2021)

[CON23] *ConSenses GmbH*. URL www.consenses.de, accessed on 18.12.2023

[COR21] CORRIGAN, A. ; SUTTON, D. ; ZIMMERMANN, J. ; DILLON, L. ; BERA, K. ; MEIER, A. ; CECCHI, F. ; MADABHUSHI, A. ; SCHMIDT, G. ; HIPP, J.: Image analysis in drug discovery. In: *The Era of Artificial Intelligence, Machine Learning, and Data Science in the Pharmaceutical Industry* : Academic Press, 2021 — ISBN 9780128200452

[DAK18] DAKIN, J. ; BROWN, R.: *Handbook of optoelectronics. Volume 3, Applications of optoelectronics*, 2018 — ISBN 9781138102262

[DEM09] DEMTRÖDER, W.: *Experimentalphysik 2*, *Springer-Lehrbuch*. Berlin, Heidelberg : Springer Berlin Heidelberg, 2009 — ISBN 978-3-66-255789-1, 978-3-66-255790-7

[DÍE18] DÍEZ, J. ; CATALÁN, J. ; BLANCO, A. ; GARCÍA-PEREZ, J. ; BADESA, F. ; GACÍA-ARACIL, N.: Customizable optical force sensor for fast prototyping and cost-effective applications. In: *Sensors (Switzerland)* (2018)

[DIN03] *DIN 8583-3: Manufacturing processes forming under compressive conditions - Part 3: Free forming; Classification, subdivision, terms and definitions*, 2003

[DIN22] DIN 8580:2022-12 Manufacturing processes - Terms and definitions, division (2022)

[DON17] DONG, Y. L. ; PAN, B.: A Review of Speckle Pattern Fabrication and Assessment for Digital Image Correlation. In: *Experimental Mechanics 2017 57:8* Bd. 57, Springer (2017)

[DRO18] DROSSEL, W. ; HENSEL, S. ; NESTLER, M. ; MÜLLER, R.: Method for Large-Scale Production of Piezoceramic-Metal-Compounds. In: *Advanced Engineering Materials* Bd. 20, John Wiley & Sons, Ltd (2018)

[DUB19] DUBOST, F. ; BORTSOVA, G. ; ADAMS, H. ; IKRAM, M. ; NIESSEN, W. ; VERNOOIJ, M. ; DE BRUIJNE, M.: Hydranet: Data augmentation for regression neural networks. In: *Medical Image Computing and Computer Assisted Intervention–MICCAI 2019:* 22nd International Conference, Shenzhen, China, October 13–17, 2019, Proceedings, Part IV 22. Springer International Publishing, 2019

[ELG05] EL GAMAL, A. ; ELTOUKHY, H.: CMOS image sensors. In: *IEEE Circuits and Devices Magazine* Bd. 21 (2005)

[GEI04] GEISSLER, M. ; XIA, Y.: Patterning: Principles and some new developments. In: *Advanced Materials* Bd. 16 (2004), Nr. 15 SPEC. ISS.

[GEV06] Gevatter, H. ; Grünhaupt, U. (Eds.). (2006). Handbuch der Mess- und Automatisierungstechnik im Automobil: Fahrzeugelektronik, Fahrzeugmechatronik. Berlin, Heidelberg: Springer Berlin Heidelberg.

[GIA00] GIACHETTI, A.: Matching techniques to compute image motion. In: *Image and Vision Computing* Bd. 18, Elsevier (2000)

[GOH21] GOH, K. ; YEAP, K. ; TEH, P.: Lateral chromatic aberration correction method and lens design feedback for dynamic optical tilt. In: *Results in Optics* Bd. 4, Elsevier (2021)

[GRA16] GRANDAL, T. ; FRAGA, S. ; VAZQUEZ, J.; ZORNOZA, A.: Technique for embedding fiber optics in metallic structures for smart material applications. In: *8th European Workshop on Structural Health Monitoring, EWSHM 2016*, 2016 — ISBN 9781510827936

[GRA18] GRANDAL, T. ; ZORNOZA, A. ; FRAGA, S. ; CASTRO, G. ; SUN, T. ; GRATTAN, K.: Laser Cladding-Based Metallic Embedding Technique for Fiber Optic Sensors. In: *Journal of Lightwave Technology* Bd. 36, Institute of Electrical and Electronics Engineers Inc. (2018)

[GRE10] GREBENYUK, A. ; RYABUKHO, V.: Digital image correlation with fast Fourier transform for large displacement measurement. In: *Saratov Fall Meeting 2010: Optical Technologies in Biophysics and Medicine XII*. Bd. 7999 : SPIE, 2010

[GRO05] GROSS, H.: *Handbook of Optical Systems*. Bd. 1 : Wiley-VCH, 2005 — ISBN 9783527699223

[GRO07] GROCHE, P. ; FRITSCHE, D. ; TEKKAYA, E. ; ALLWOOD, J. ; HIRT, G. ; NEUGEBAUER, R.: Incremental Bulk Metal Forming. In: *CIRP Annals - Manufacturing Technology* (2007)

[GRO11] GROCHE, P. ; TÜRK, M.: Smart structures assembly through incremental forming. In: *CIRP Annals - Manufacturing Technology* (2011)

[GRO14] GROCHE, P. ; BRENNEIS, M.: Manufacturing and use of novel sensoric fasteners for monitoring forming processes. In: *Measurement: Journal of the International Measurement Confederation* (2014)

[GRO17a] GROCHE, P. ; KRECH, M.: Efficient production of sensory machine elements by a two-stage rotary swaging process—Relevant phenomena and numerical modelling. In: *Journal of Materials Processing Technology* Bd. Groche, P. (2017)— ISBN 9780819485724

[GRO17b] GROCHE, P. ; HOPPE, F. ; SINZ, J.: Stiffness of multipoint servo presses: Mechanics vs. control. In: *CIRP Annals - Manufacturing Technology* (2017)

[GRO18] GROCHE, P. ; TAPLICK, C. ; ÖZEL, M. ; MAHAJAN, P. ; STAHL, S.: Benefits of stress superposition in combined bending-linear flow splitting process. In: *International Journal of Material Forming* Bd. 11, Springer-Verlag France (2018)

[GRO19] GROCHE, P. ; HOHMANN, J. ; ÜBELACKER, D.: Overview and comparison of different sensor positions and measuring methods for the process force measurement in stamping operations. In: *Measurement* Bd. 135, Elsevier (2019)

[GUE15] GUENTHER, B.: Modern Optics, Oxford University Press (2015) — ISBN 9780191801983

[GUN05] GUNTURK, B. ; GLOTZBACH, J. ; ALTUNBASAK, Y. ; SCHAFER, R. ; MERSEREAU, R.: Demosaicking: Color filter array interpolation. In: *IEEE Signal Processing Magazine* Bd. 22, Institute of Electrical and Electronics Engineers Inc. (2005)

[HAF21] HAFEEZ, M. ; RASHID, M. ; TARIQ, H. ; ABIDEEN, Z.; ALOTAIBI, S. ; SINKY, M.: Performance Improvement of Decision Tree: A Robust Classifier Using Tabu Search Algorithm. In: *Applied Sciences* Bd. 11 (2021), Nr. 15

[HEC18] HECHT, E.: *Optik.* Berlin, Boston: De Gruyter, 2018. https://doi.org/10.1515/9783110526653

[HEH18] HEHR, A. ; NORFOLK, M. ; WENNING, J. ; SHERIDAN, J. ; LESER, P. ; LESER, P. ; NEWMAN, J.: ADDITIVE MANUFACTURING OF COMPOSITES AND COMPLEX MATERIALS Integrating Fiber Optic Strain Sensors into Metal Using Ultrasonic Additive Manufacturing. In: *JOM* Bd. 70

[HER22] HERBST, F. ; CHADDA, R. ; HARTMANN, C. ; PETERS, J. ; RIEHL, D. ; GWOSCH, T. ; HOFMANN, K. ; MATTHIESEN, S. ; KUPNIK, M.: Multi-axis Force Sensor for Sensor-integrating Bolts. In: *Proceedings of IEEE Sensors* Bd. 2022-Octob, Institute of Electrical and Electronics Engineers Inc. (2022) — ISBN 9781665484640

[HIR12] HIRSCH, M.: *Einfluss von Leichtbauwerkstoffen in schnelllaufenden Stanzwerkzeugen auf das Verschleißverhalten*, Technische Universität München, 2012

[HON12] HONG, D. ; KIM, Y. ; KWAK, J.; JEONG, C. ; AN, J.: Miniature force-torque sensor using semiconductor strain gage sensor frame design and analysis for development. In: *2012 9th International Conference on Ubiquitous Robots and Ambient Intelligence, URAI 2012*, 2012 — ISBN 9781467331104

[HU18] HU, S. ; WANG, H. ; WANG, Y. ; LIU, Z.: Design of a Novel Six-Axis Wrist Force Sensor. In: *Sensors (Basel, Switzerland)* Bd. 18, Multidisciplinary Digital Publishing Institute (MDPI) (2018)

[HUN03] HUNG, P. ; VOLOSHIN, A.: In-plane strain measurement by digital image correlation. In: *Journal of the Brazilian Society of Mechanical Sciences and Engineering* Bd. 25, Associação Brasileira de Engenharia e Ciências Mecânicas - ABCM (2003)

[IBR05] IBRAHIM, R. ; PETTIT, C. : Uncertainties and dynamic problems of bolted joints and other fasteners. In: *Journal of Sound and Vibration* Bd. 279, Academic Press (2005)

[ISH19] ISHKINA, S. ; CHARNI, D. ; HERRMANN, M. ; LIU, Y. ; EPP, J. ; SCHENCK, C. ; KUHFUSS, B. ; ZOCH, H.: Influence of process fluctuations on residual stress evolution in rotary swaging of steel tubes. In: *Materials* Bd. 12, Multidisciplinary Digital Publishing Institute (2019)

[JIA21] JIANG, X. ; MA, J. ; XIAO, G. ; SHAO, Z. ; GUO, X.: A review of multimodal image matching: Methods and applications. In: *Information Fusion* Bd. 73, Elsevier (2021)

[KAN14] KANG, M. ; LEE, S. ; KIM, J.: Shape optimization of a mechanically decoupled six-axis force/torque sensor. In: *Sensors and Actuators A: Physical* Bd. 209, Elsevier (2014)

[KEI17] KEIL, S.: *Dehnungsmessstreifen* : Springer Fachmedien Wiesbaden, 2017. https://doi.org/10.1007/978-3-658-13612-3

[KIM18] KIM, S. ; EBINA, A. ; SANO, A. ; KUBOTA, S.: *Monitoring of process and tool status in forging process by using bolt type piezo-sensor*. . — Procedia Manufacturing

[KIM20] KIM, U. ; JEONG, H. ; DO, H. ; PARK, J. ; PARK, C.: Six-Axis force/torque fingertip sensor for an anthropomorphic robot hand. In: *IEEE Robotics and Automation Letters* Bd. 5, Institute of Electrical and Electronics Engineers Inc. (2020)

[KOK15] KOKORIAN, J. ; BUJA, F. ; VAN SPENGEN, W.: In-plane displacement detection with picometer accuracy on a conventional microscope. In: *Journal of Microelectromechanical Systems* (2015)

[KRA15] KRÄUSEL, V. ; GRAF, A. ; HEINRICH, M. ; DECKER, R. ; CASPAR, M. ; KROLL, L. ; HARDT, W. ; GÖSCHEL, A.: Development of hybrid assembled composites with sensory function. In: *CIRP Annals - Manufacturing Technology* Bd. 64, Elsevier (2015)

[KRA17] KRAUS, D. ; LIEBERENZ, M. ; GROCHE, P.: Reduction of tool wear by systematic design of the tool clamping situation. In: *Journal of Manufacturing Processes* Bd. 28, Elsevier (2017)

[KRA18] Kraus, D.: *Einfluss der Werkzeugspannsituation auf den Scherschneidprozess*. Aachen, Shaker Verlag, 2018

[KRA20] KRAUS, B. ; NEU, M. ; KIRCHNER, E.: Sensing machine elements as enablers of comprehensive digitization - A review. In: *2020 10th International Electric Drives Production Conference, EDPC 2020 - Proceedings*, Institute of Electrical and Electronics Engineers Inc. (2020)

[KRE18] KRECH, M. ; TRUNK, A. ; GROCHE, P.: Controlling the sensor properties of smart structures produced by metal forming. In: *Journal of Materials Processing Technology* (2018)

[KRE20] KRECH, M.: *Adaptiver Umformprozess zur Herstellung und simultanen Kalibrierung von metallischen Strukturen mit bauteil*. Düren : Shaker Verlag, 2020 — ISBN 978-3-8440-7514-4

[KRE21] KRECH, M.: Measuring device for arranging in a cylindrical interior section of a hollow body. Patent [DE102020119655B4], 2022.

[LEE16] LEE, D. ; KIM, U. ; JUNG, H. ; CHOI, H.: A capacitive-type novel six-axis force/torque sensor for robotic applications. In: *IEEE Sensors Journal* Bd. 16, Institute of Electrical and Electronics Engineers Inc. (2016)

[LEM08] LEMMEN, H. ; ALDERLIESTEN, R. ; BENEDICTUS, R. ; HOFSTEDE, J. ; RODI, R.: The power of Digital Image Correlation for detailed elastic-plastic strain measurements. In: *WSEAS international conference on engineering mechanics, structures, engineering geology. Crate Island, Greece. 2008.*

[LEV19] LEVINSON, H.: *Principles of Lithography, Fourth Edition* : SPIE, 2019
https://doi.org/10.1117/3.865363
ISBN: 9780819483256

[LI23] LI, S. ; LI, H. ; ZHOU, X. ; WANG, Y. ; LI, X. ; GAN, D. ; ZHU, R.: Damage detection of flange bolts in wind turbine towers using dynamic strain responses. In: *Journal of Civil Structural Health Monitoring* Bd. 13, Springer Science and Business Media Deutschland GmbH (2023)

[LIB75] LIBERTINY, G.: The design of multiaxial force/moment transducers with particular emphasis on the problem of cross-talk - Techniques to improve the accuracy of complex multiaxial transducers, by eliminating cross-talk, have been developed and illustrated through the desc. In: *Experimental Mechanics* Bd. 15, Kluwer Academic Publishers (1975)

[LIN17] LIN, P.: Advanced Geometrical Optics. In: , *Progress in Optical Science and Photonics*. Bd. 4. Singapore, Springer Singapore (2017) — ISBN 978-981-10-2298-2

[LIN20] LIN, C. ; AHMAD, A. ; KEBEDE, G.: Novel Mechanically Fully Decoupled Six-Axis Force-Moment Sensor. In: *Sensors 2020, Vol. 20, Page 395* Bd. 20, Multidisciplinary Digital Publishing Institute (2020)

[LIT05] LITFIN, G. (Hrsg.): *Technische Optik in der Praxis*. 3. Aufl. Berlin Heidelberg : Springer-Verlag, 2005 — ISBN 978-3-54-021884-5, 978-3-54-026709-6

[LU22] LU, M.: Advancement of Chip Stacking Architectures and Interconnect Technologies for Image Sensors. In: *Journal of Electronic Packaging, Transactions of the ASME* Bd. 144, American Society of Mechanical Engineers (ASME) (2022), Nr. 2

[LVS20] LV, C. ; WANG, S. ; SHI, C.: A High-Precision and Miniature Fiber Bragg Grating-Based Force Sensor for Tissue Palpation During Minimally Invasive Surgery. In: *Annals of Biomedical Engineering* Bd. 48, Springer (2020)

[MA21] MA, C. ; REN, Q. ; ZHAO, J.: Optical-numerical method based on a convolutional neural network for full-field subpixel displacement measurements. In: *Optics Express* Bd. 29, Optica Publishing Group (2021)

[MAL14] MALACARA, D. ; MALACARA, Z.: *Handbook of Optical Design, Second Edition* : Marcel Dekker, 2014 — ISBN 9780203912942

[MEL16] MELZ, T. ; WIEDEMANN, M. ; MELZER, T.: *Smarte Strukturen und Systeme Tagungsband des 4SMARTS-Symposiums, 6.-7. April 2016, Darmstadt*. Oldenbourg : De Gruyter Oldenbourg, 2016 — ISBN 3110467135

[MES23] ME-MEßSYSTEME: *kb-festigkeitslehre*. URL https://www.me-systeme.de/docs/grundlagen/kb-festigkeitslehre.pdf. - accessed on 2023-12-18

[MIC09] SCHREIER, H.; ORTEU, J.; SUTTON, M.: Digital Image Correlation (DIC). In: *Image Correlation for Shape, Motion and Deformation Measurements* : Springer, Boston, MA, 2009

[MOE12] MÖHRING, H. ; BERTRAM, O.: Integrated autonomous monitoring of ball screw drives. In: *CIRP Annals - Manufacturing Technology* Bd. 61 (2012)

[MOL22] MOLITOR, D. ; KUBIK, C. ; HETFLEISCH, R. ; GROCHE, P.: Workpiece image-based tool wear classification in blanking processes using deep convolutional neural networks. In: *Production Engineering* Bd. 16, Springer Science and Business Media Deutschland GmbH (2022)

[MOU97] MOUROULIS, P. ; MACDONALD, J.: *Geometrical optics and optical design*. New York : Oxford University Press, 1997 — ISBN 0195089316, 9780195089318

[MUE16] MÜLLER, M. ; MÜLLER, B. ; HENSEL, S. ; NESTLER, M. ; JAHN, S. ; MÜLLER, R. ; SCHUBERT, A. ; DROSSEL, W.: Structural integration of piezoceramic fibers in deep drawn sheet metal for material-integrated health monitoring. In: *Mechatronics* Bd. 34, Pergamon (2016)

[MUE17] MÜLLER, B. ; PIERER, A. ; SCHMIDT, M. ; SCHUBERT, A. ; KORIATH, H. ; PUTZ, M. ; WITTSTOCK, V.: In-Process Monitoring of Joining Operations for Piezoceramic Elements. In: *Key Engineering Materials* (2017)

[NAK05] NAKAMURA, J.: *Image sensors and signal processing for digital still cameras* : Taylor & Francis, 2005 — ISBN 9781420026856

[NOH16] NOH, Y. ; BIMBO, J. ; SAREH, S. ; WURDEMANN, H. ; FRAŚ, J. ; CHATHURANGA, D. ; LIU, H. ; HOUSDEN, J. ; ALTHOEFER, K. ; RHODE, K.: Multi-Axis force/torque sensor based on Simply-Supported beam and optoelectronics. In: *Sensors (Switzerland)* (2016)

[OHT05] OHTA, H. ; SUMIGAWA, T.: Bolt with function of measuring strain. Patent [US7293466B2] 2005.

[OHT20] OHTA, J.: *Smart CMOS Image Sensors and Applications* : CRC Press, 2020 — ISBN 9781315156255

[ONR23] *Optical force-/torque sensor*. URL https://onrobot.com/de/produkte/hex-6-achsiger-kraft-drehmoment-sensor. accessed on 2023-10-03

[PAN06] PAN, B. ; XIE, H.; XU, B. ; DAI, F.: Performance of sub-pixel registration algorithms in digital image correlation. In: *Measurement Science and Technology*, 2006

[PAN09] PAN, B. ; QIAN, K. ; XIE, H. ; ASUNDI, A.: Two-dimensional digital image correlation for in-plane displacement and strain measurement: A review. In: *Measurement Science and Technology* Bd. 20, IOP Publishing (2009)

[PAN12] PAN, B. ; WU, D. ; XIA, Y.: An active imaging digital image correlation method for deformation measurement insensitive to ambient light. In: *Optics and Laser Technology* (2012)

[PAR09] PARK, J. ; BYUN, S. ; LEE, B.: Lens distortion correction using ideal image coordinates. In: *IEEE Transactions on Consumer Electronics* Bd. 55 (2009)

[PAR22] PARK, H. ; CHOI, J. ; CHOI, J. ; JOO, K. ; KIM, N.: Investigation of the Hue–Wavelength Response of a CMOS RGB-Based Image Sensor. In: *Sensors* Bd. 22, Multidisciplinary Digital Publishing Institute (2022)

[PER13] PERVEEN, N. ; KUMAR, D. ; BHARDWAJ, I.: An overview on template matching methodologies and its applications. In: *International Journal of Research in Computer and Communication Technology* Bd. 2 (2013)

[PIL04] PILCH, A. ; MAHAJAN, A. ; CHU, T.: Measurement of whole-field surface displacements and strain using a genetic algorithm based intelligent image correlation method. In: *Journal of Dynamic Systems, Measurement and Control, Transactions of the ASME* Bd. 126, American Society of Mechanical Engineers Digital Collection (2004)

[PRO23] *ProCam® - Camera modules active alignment & testing*. URL https://trioptics.com/products/procam-camera-modules-active-alignment-and-testing/. - accessed on 2023-10-19

[RAT07] RATHMANN, T.: Entwicklung eines Technologieprozessors zur Untersuchung des Kaltrundknetens mit Hilfe der Finite-Elemente-Analyse. Aachen, Shaker Verlag, 2007— ISBN 978-3-8322-5825-2

[REU14] REU, P.: All about speckles: Aliasing. In: *Experimental Techniques* (2014). https://doi.org/10.1111/ext.12111

[RIZ18] RIZVI, S.: *Handbook of photomask manufacturing technology* : CRC Press, 2018

[SAN07] SANDLIN, S. ; KOSONEN, T. ; HOKKANEN, A. ; HEIKINHEIMO, L.: Use of brazing technique for manufacturing of high temperature fibre optical temperature and displacement transducer. In: *Materials Science and Technology* Bd. 23 (2007)

[SAS19] SASIÁN, J.: Introduction to lens design. In: *Introduction to Lens Design*, Cambridge University Press 2019 — ISBN 9781108625388

[SAX22] SAXENA, A.: An Introduction to Convolutional Neural Networks. In: *International Journal for Research in Applied Science and Engineering Technology* Bd. 10, International Journal for Research in Applied Science and Engineering Technology (IJRASET) (2022)

[SCH13] SCHWANKL, M. ; RÜBNER, M. ; SINGER, R.F. ; KÖRNER, C.: Integration of PZT-Ceramic Modules using Hybrid Structures in High Pressure Die Casting. In: *Procedia Materials Science* Bd. 2, Elsevier (2013)

[SCH14a] SCHUBERT, A.S ; WITTSTOCK, V. ; JAHN, S. ; MÜLLER, B. ; MÜLLER, M.: Joining by forming of piezoceramic macro-fiber arrays within micro-structured surfaces of aluminum sheets. In: *Production Engineering* (2014)

[SCH14b] SCHUBERT, A. ; WITTSTOCK, V. ; KORIATH, H. J. ; JAHN, S. F. ; PETER, S. ; MÜLLER, B. ; MÜLLER, M.: Smart metal sheets by direct functional integration of piezoceramic fibers in microformed structures. In: *Microsystem Technologies* (2014)

[SCH21] SCHAUMANN, P. ; BÖHM, M.: Development and challenges of support structures for offshore wind turbines. In: *ce/papers* Bd. 4, John Wiley & Sons, Ltd (2021)

[SCU21] SCIUTI, V.; CANTO, R. ; NEGGERS, J. ; HILD, F.: On the benefits of correcting brightness and contrast in global digital image correlation: Monitoring cracks during curing and drying of a refractory castable. In: *Optics and Lasers in Engineering* Bd. 136, Elsevier (2021)

[SHA20] SHARIFZADEH, M. ; BENALI, H. ; RIVAZ, H.: Phase aberration correction: A convolutional neural network approach. In: *IEEE Access* Bd. 8, Institute of Electrical and Electronics Engineers Inc. (2020)

[SMI21] SMITH, M. ; SMITH, L. ; HANSEN, M.: The quiet revolution in machine vision - a state-of-the-art survey paper, including historical review, perspectives, and future directions. In: *Computers in Industry* Bd. 130, Elsevier (2021)

[SPU12] SPUR, G. ; NEUGEBAUER, R. ; HOFFMANN, H.: *Handbuch Umformen* : Carl Hanser Verlag GmbH & Company KG, 2012 — ISBN 9783446430044

[STE12] STEINICH, T. ; BLAHNIK, V.: Optical design of camera optics for mobile phones. In: *Advanced Optical Technologies* Bd. 1, Walter de Gruyter GmbH (2012)

[SUN14] SUN, C.; HSIAO, T.: On the background design for microscale background-oriented schlieren measurements of microfluidic mixing. In: *Microfluidics and Nanofluidics* Bd. 17, Springer Verlag (2014)

[SUT08] SUTTON, M.: Digital Image Correlation for Shape and Deformation Measurements. In: *Springer Handbook of Experimental Solid Mechanics*, 2008

[SWA16] SWAROOP, P. ; SHARMA, N.: An overview of various template matching methodologies in image processing. In: *International Journal of Computer Applications* Bd. 153, Foundation of Computer Science (2016)

[SZC19] SZCZEPANKOWSKI, P. ; NIEZNANSKI, J.: Application of barycentric coordinates in space vector PWM computations. In: *IEEE Access* Bd. 7, Institute of Electrical and Electronics Engineers Inc. (2019)

[TAP16] TAPLICK, C.: Kombiniertes Hochkant-Biegen und Spaltprofilieren, Berichte aus Produktion und Umformtechnik. Bd. 104. Aachen : Shaker Verlag, 2016 — ISBN 9783844047486

[TAR11] TAR, Á. ; CSEREY, G.: Development of a low cost 3D optical compliant tactile force sensor. In: *IEEE/ASME International Conference on Advanced Intelligent Mechatronics, AIM*, 2011 — ISBN 9781457708381

[TEM20] TEMPLEMAN, J. ; SHEIL, B. ; SUN, T.: Multi-axis force sensors: A state-of-the-art review. In: *Sensors and Actuators, A: Physical* Bd. 304, Elsevier (2020)

[TIE17] TIEDEMANN, R. ; PILLE, C. ; DUMSTORFF, G. ; LANG, W.: Sensor integration in castings made of Aluminum - New approaches for direct sensor integration in aluminum high pressure die casting. In: *Key Engineering Materials*, 2017 — ISBN 9783035711981

[TON05] TONG, W.: An evaluation of digital image correlation criteria for strain mapping applications. In: *Strain* Bd. 41, John Wiley & Sons, Ltd (2005)

[VEN21] VENKATARAMAN, K.: *Design of Jigs, Fixtures and Press Tools* : Springer International Publishing, 2021 — ISBN 9783030765330

[WOL23] WOLF, A.: Integrated Optical Deformation Measurement with TIR Prism Rods. In: *Sensors* Bd. 23 (2023)

[WRI17] WRIGHT, A. ; POLAND, S.: Adaptive optics for aberration correction in optical microscopy. In: *Handbook of Photonics for Biomedical Engineering*, Springer Netherlands 2017 — ISBN 9789400750524

[XIE12] XIE, H. ; JIANG, A. ; SENEVIRATNE, L. ; ALTHOEFER, K.: Pixel-based optical fiber tactile force sensor for robot manipulation. In: *Proceedings of IEEE Sensors*, 2012 — ISBN 9781457717659

[XIO18] XIONG, L. ; JIANG, G. ; GUO, Y. ; LIU, H.: A Three-Dimensional Fiber Bragg Grating Force Sensor for Robot. In: *IEEE Sensors Journal* Bd. 18, Institute of Electrical and Electronics Engineers Inc. (2018)

[XU05] XU, M. ; WATANACHATURAPORN, P. ; VARSHNEY, P. ; ARORA, M.: Decision tree regression for soft classification of remote sensing data. In: *Remote Sensing of Environment* Bd. 97, Elsevier (2005)

[YAN06] YANG, F. ; HE, X. ; QUAN, C.: Characterization of dynamic microgyroscopes by use of temporal digital image correlation. In: *Applied Optics* Bd. 45, Appl Opt (2006)

[YAN15] YANG, L. ; LIU, S. ; TSOKA, S. ; PAPAGEORGIOU, L.: Sample re-weighting hyper box classifier for multi-class data classification. In: *Computers and Industrial Engineering* Bd. 85, Pergamon (2015)

[YAO07] YAOFENG, S. ; PANG, J.: Study of optimal subset size in digital image correlation of speckle pattern images. In: *Optics and Lasers in Engineering* (2007)

[ZHA03] ZHANG, J. ; JIN, G. ; MA, S. ; MENG, L.: Application of an improved subpixel registration algorithm on digital speckle correlation measurement. In: *Optics and Laser Technology* Bd. 35, Elsevier (2003)

[ZHA06] ZHANG, Y.: In situ fatigue crack detection using piezoelectric paint sensor. In: *Journal of Intelligent Material Systems and Structures* Bd. 17 (2006)

[ZHA16] ZHAO, Y. ; ZHAO, Y. ; WANG, C. ; LIANG, S. ; CHENG, R. ; QIN, Y. ; WANG, P. ; LI, Y. ; LI, X. ; HU, T.: Design and development of a cutting force sensor based on semi-conductive strain gauge. In: *Sensors and Actuators, A: Physical* Bd. 237, Elsevier (2016)

[ZHA19a] ZHANG, Y.: *Systematic design of microscope objectives*. Jena, 2019. — Dissertation, Friedrich-Schiller-Universität Jena, 2019

[ZHA19b] ZHAO, J. ; SANG, Y. ; DUAN, F.: The state of the art of two-dimensional digital image correlation computational method. In: *Engineering Reports* (2019)

[ZOU14] ZOU, R. ; CAO, R. ; ZAGHLOUL, M. ; YAN, A. ; CHEN, R. ; OHODNICKI, P. ; BURIC, M. ; CRANDALL, D. ; LIANG, X. ;TO, A. ; CHEN, K.: Optical fiber sensor-fused additive manufacturing and its applications in residual stress measurements in titanium parts. In: *Optics InfoBase Conference Papers* : Optical Society of America, 2014 — ISBN 9780960038053

Formula symbols and abbreviations

Formula characters, Latin letters

Character	Unit	meaning
$\Delta x, \Delta y, \Delta z$	mm	Translational Displacement
V_f	mm/s	Infeed Speed Rotary Swaging
f_{rot}	Hz	Frequency of Workpiece Rotation
f_{sw}	Hz	Swaging Frequency
n_i	-	Lens Refractive Index
R	mm	Lens Radius of Curvature
F	-	Lens Focal Point
f	mm	Lens Focal Length
H	-	Lens Principal Plane
A	-	Object Plane
B	-	Image Plane
a	mm	Distance Between the Object Plane A and Lens
b	mm	Distance Between the Lens and the Image Plane B
m	-	Optical Magnification Factor
l_m	mm	Measuring Distance
$\vec{k}^T$	-	Vector of Calibrating Coefficients
P_i	-	Evaluation Point on Object Surface
M_{t}	Nm	Torsional Load
M_x, M_y, M_z	Nm	Moments
F_x, F_y, F_z	N	forces

$\vec{v}$	-	Two Point Connecting Vector
$\vec{c}_{\mathrm{i}}$	-	Initial Position of Evaluation Points P_i
$\vec{c}_{\mathrm{CR\_d}}$	-	Center of Rotation on Mirrored Image Segment
$\vec{c}_{\mathrm{CR\_m}}$	-	Center of Rotation on Direct Image Segment
Δl_m	mm	Distance Change of Measuring Distance l_m
l	mm	Length
l_p	mm	Distance between two Positions
D	mm	Outer Diameter
d	mm	Inner Diameter
E	N/m^2	Young's Modulus
A	mm^2	Cross-Sectional Area
W_b	mm^3	Bending Section Modulus
I_{xy}	mm^4	Product Moment of Area
W_p	mm^3	Torsional Section Modulus
G	N/mm^2	Shear Modulus
arc	mm	Arc Length of the Angle of Twist φ at the Inner Diameter d
s_p	-	Subpixel Registration
s	mm	Measuring Resolution
A_s	mm^2	Image Sensor Area
d_x	pixel	Detected Displacement
U3	mm	Axial Material Flow

Formula character, Greek letters

Character	Unit	meaning
α_H	°	Angle of Rotation per Stroke Rotary Swaging
θ	°	Angle, Rotational Displacement
φ	°	Angle of Twist
$\emptyset$	°	Angle of Rotation of Border Line Between Direct and Mirrored Image Segments
γ	°	Angle of Tilt
$\vec{\delta}_{\mathrm{xy}}$	mm	Plane Deflection In $x - y$ Plane
ε_b	µm/m	Bending Strain
ε_N	µm/m	Normal Strain
ε_τ	µm/m	Torsional Shear Strain
σ	MPa	Stress
σ_b	MPa	Bending Stress
$\varepsilon_{b,d}$	µm/m	Bending Strain at Inner Diameter d
$\varepsilon_{\tau,d}$	µm/m	Shear Torsional Strain at Inner Diameter d
σ_y	MPa	Yield Strength

Abbreviations

Abbreviation	Meaning
DIN	German Institute for Standardisation
LED	Light-Emitting Diode
MRI	Magnetic Resonance Imaging
ICs	Integrated Circuits
OMA	On-Chip Micro-Lens Array
RGB	RGB Color Filter
CFA	CFA Color Filter
CCD	Charge Coupled Device
CMOS	Complementary Metal Oxide Semiconductor
DIC	Digital Image Correlation
FFT	Fast Fourier Transform
MEMS	Microelectromechanical Systems
CNN	Convolutional Neural Networks
ANN	Artificial Neural Network
GAN	Generative Adversarial Network
3D	Three Dimensions
2D	Two Dimensions
NCC	Normalized Cross Correlation
NSSD	Normalized Sum Square Difference
F-CNN	First Level CNN Algorithm
S-CNN	Second Level CNN Algorithm
T-CNN	Third Level CNN Algorithm

DTR	Decision Tree Regression
ALE	Arbitrary Lagrangian-Eulerian